

---

Aus dem Josef Lissner Laboratory for Biomedical Imaging  
des Instituts für Klinische Radiologie  
der Ludwig-Maximilians-Universität München

Direktor: Prof. Dr. med. Dr. h.c. Maximilian F. Reiser, FACR, FRCR

**Ultra-high field magnetic resonance diffusion tensor imaging  
of the hyaline articular cartilage**

Dissertation zum Erwerb des Doktorgrades der Humanbiologie  
an der Medizinischen Fakultät der Ludwig-Maximilians-Universität zu München

vorgelegt von  
Lucianna Filidoro  
aus  
Florenz (Italien)

2011

---

**Mit Genehmigung der Medizinischen Fakultät der Universität München**

Berichterstatter:

Prof. Dr. med. Dr. h.c. Maximilian F. Reiser, FACR, FRCR

Mitberichterstatter:

Prof. Dr. Karl-Hans Englmeier

Prof. Dr. Peter E. Müller

Mitbetreuung durch die promovierten Mitarbeiter:

Prof. Dr. med. Dr. h.c. Maximilian F. Reiser, FACR, FRCR

Priv.-Doz. Dr. med. Christian Glaser

Priv.-Doz. Dr. rer. nat. Olaf Dietrich

Dr. rer. biol. hum. José Raya

Dekan:

Prof. Dr. med. Dr. h.c. Maximilian F. Reiser, FACR, FRCR

Tag der mündlichen Prüfung:

21.11.2011

---

# Content

1 Introduction .....	1
2 Articular cartilage .....	5
2.1 Functional characteristics and composition .....	5
2.2.1 Morphology .....	7
2.2.2 Chondrocytes .....	9
2.2.3 Collagen.....	9
2.2.4 Glycans .....	11
2.2.5 Interstitial water .....	13
2.2.6 Metabolic activities.....	13
2.3 Ultrastructure .....	14
2.3.1 Tangential zone.....	15
2.3.2 Transitional zone .....	15
2.3.3 Radial zone .....	15
2.4 Osteoarthritis.....	16
2.4.1 Epidemiology .....	16
2.4.2 Etiology .....	16
2.4.3 Pathogenesis .....	17
2.4.4 Symptoms .....	19
2.4.5 Diagnosis .....	19
2.4.6 Early diagnosis .....	19
2.4.7 Therapy.....	20
3 Magnetic resonance imaging (MRI) of molecular diffusion .....	21
3.1 Introduction.....	21
3.2 Diffusion-weighted imaging (DWI) .....	23
3.2.1 Theory of diffusion.....	23
3.2.2 Measurement principles.....	23
3.2.2 Apparent diffusion coefficient (ADC).....	26
3.3 Diffusion tensor imaging (DTI) .....	27
3.3.1 Determination of the diffusion tensor.....	27
3.3.2 Quantitative parameters obtained by DTI .....	28
4 DTI of cartilage at 9.4 Tesla.....	31
4.1 Introduction.....	31

---

4.2	Materials & Methods .....	32
4.2.1	Sample preparation .....	32
4.2.2	MRI.....	34
4.3	Results.....	37
4.4	Discussion and conclusions .....	43
5	DTI of cartilage at 17.6 Tesla: feasibility and limitations.....	47
5.1	Introduction.....	47
5.2	Instrument .....	47
5.2.1	Main magnet.....	48
5.2.2	Gradient system .....	49
5.2.3	RF coil .....	50
5.3	Optimization of the DTI protocol .....	51
5.3.1	DTI in an isotropic phantom.....	52
5.3.2	Analysis of temperature influences .....	54
5.3.3	Analysis of b-matrix .....	56
5.3.4	Eddy-current effects .....	57
5.3.5	Chemical-shift artifacts.....	57
5.4	Coordinate systems .....	61
5.5	FA versus SNR .....	63
5.6	Discussion and conclusions .....	64
6	DTI of cartilage at 17.6 T: correlation with histology and scanning electron microscopy .....	67
6.1	Introduction.....	67
6.2	Materials & Methods .....	68
6.2.1	Sample preparation .....	68
6.2.2	MRI.....	68
6.2.3	Biomechanical testing.....	72
6.2.3	Scanning electron microscopy (SEM).....	74
6.2.4	Histology .....	77
6.3	Results.....	78
6.3.1	MRI.....	78
6.3.2	Biomechanical testing.....	80
6.3.3	SEM.....	81
6.3.4	Histology .....	83
6.4	Discussion and conclusions .....	85
6.4.1	Comparison with previous DTI in articular cartilage.....	85
6.4.2	DTI under mechanical loading .....	87
6.4.3	DTI versus SEM .....	87
6.4.4	DTI versus Histology .....	88
6.4.5	Influence of cartilage components on the measured parameters.....	88
6.4.6	Conclusions .....	90
7	Conclusions and summary.....	91

---

Zusammenfassung .....	95
Bibliography .....	99
Danksagung .....	117



---

# 1 Introduction

Articular cartilage is a highly structured tissue and plays an important role in the pathogenesis of osteoarthritis (OA), which is a global socioeconomic burden (Yelin 1995, MacLean 1998, Buckwalter 1997). The degradation of articular cartilage is considered to be an entry point in the process of irreversible joint degeneration. Loss of integrity within the collagenous fiber network is considered to be a hallmark of transition from potentially reversible to irreversible degeneration of articular cartilage long before macroscopically visible loss of cartilage substance occurs (Buckwalter 1997).

Consequently, there is a strong need to diagnose cartilage damage early, and increasing efforts are made to develop and to validate effective disease-modifying therapies. This creates a demand for tools that can not only depict damage of the articular cartilage both noninvasively and as early in the course of disease as possible, but can also quantitatively monitor the status of articular cartilage.

Magnetic resonance imaging (MRI) is a noninvasive imaging technique used primarily in medical settings to produce high quality images of the inside of the human body. MRI is based on the principles of nuclear magnetic resonance (NMR), i. e., the coherent resonant excitation of the atomic nuclei in a static magnetic field with electromagnetic radio frequency pulses. NMR spectroscopy can be used to obtain microscopic chemical and physical information about molecules. Diffusion tensor imaging (DTI) is an MRI technique based on the orientation-dependent measurement of the molecular diffusion properties of water, which can be employed to analyze the internal anisotropy of tissues and the main directions of local diffusion in a tissue. DTI allows one to calculate pixelwise a matrix (the diffusion tensor) whose elements contain directional information of local (voxel) water diffusivity, thus going beyond

---

conventional diffusion-weighted imaging (DWI), which offers information about the mean diffusivity (apparent diffusion coefficient (ADC)) of water in tissue only.

Based on the assumption that the magnitude and the direction of local tissue diffusivity are influenced by the macromolecular environment of the diffusing bulk water, DTI is thought to provide information on tissue ultrastructure. As such, DTI appears to be an ideally suited tool for analyzing tissues with a highly anisotropic ultrastructure. Thus, DTI may come very helpful for analyzing articular cartilage because it may be capable to reflect early changes in the alignment of the collagenous fibers.

The value of water diffusion as a marker for OA is largely known. First invasive measurements of the diffusion in cartilage were performed by Maroudas et al. (Maroudas 1968, Maroudas 1977), who obtained diffusion coefficients in healthy cartilage of  $1.37 \times 10^{-3} \text{ mm}^2/\text{s}$  and  $1.45 \times 10^{-3} \text{ mm}^2/\text{s}$  in OA cartilage at  $37^\circ \text{ C}$ . Since MRI can measure diffusivity non-invasively at scales of microns, diffusion can be an interesting biomarker for the early diagnosis of OA. Early works on spectroscopy and DWI of the cartilage demonstrated the increment of diffusion with enzymatic cartilage degradation (Burstein 1993).

Furthermore, DTI has been demonstrated to be effective in analyzing the microstructure of various tissues. In addition to myocardial fiber orientation (Hsu 1998), the lamellar arrangement of the annulus fibrosus of the intervertebral disc (Hsu 1999), and the spinal cord (Gulani 1997), the measurement of orientation and course of nerve fiber bundles in the white matter of the brain (Pierpaoli 1996) have also attracted high clinical interest as applications of DTI (Le Bihan 2001, Melhem 2002).

On this background, the purposes of the first part of this work (presented in detail in chapter 4) were to 1) assess the feasibility of DTI for analyzing human hyaline articular cartilage, and 2) evaluate whether DTI can demonstrate zonal architectural properties of articular cartilage (Filidoro 2005).

---

Since the signal-to-noise ratio (SNR) in MRI increases with the magnetic field strength, there is a continuous trend towards applying higher fields to improve spatial resolution (Behr VC 2004). Therefore, further MRI experiments described in chapters 5 and 6 of this work were performed at a field strength of 17.6 Tesla. The main objectives to be assessed in these experiments were to systematically examine the relationship between the DTI parameters and the constituents of the extracellular matrix (proteoglycan and collagen), and especially the dependency of the first eigenvector on the collagen structure and the mechanical properties of cartilage.



---

## 2 Articular cartilage

### 2.1 Functional characteristics and composition

Hyaline articular cartilage represents one of the three broad classes of cartilaginous tissues present in the body. The most common hyaline cartilage, and most studied, is articular cartilage. Hyaline articular cartilage is, on a macroscopic scale, glassy smooth, glistening and bluish white in appearance (although older tissues tend to lose this appearance). This tissue covers the articular surface (Figure 2.1) of long bones and sesamoid bones within synovial joints, e.g., the surfaces of the tibia, the femur, and the patella of the knee joint. Other tissues with hyaline cartilage include the larynx, the support structures of the tracheal tube, rib and costal cartilage (Mow 1997).

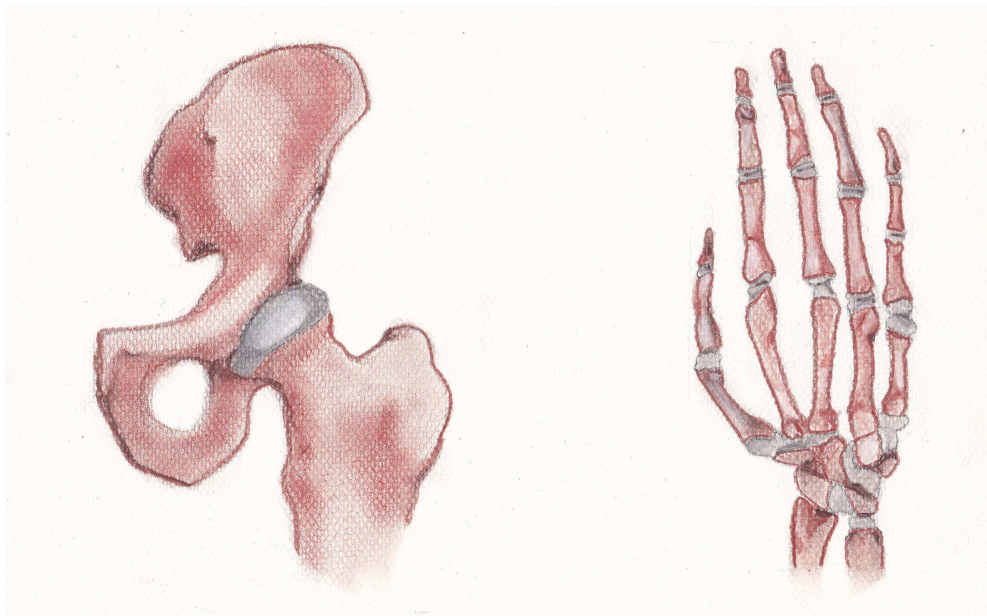


Figure 2.1: Hyaline articular cartilage is present in several joints of human body: e.g. hip and hand.

---

Hyaline articular cartilage builds temporarily the skeleton in embryo and forms most of the bones in a preliminary model of cartilage that later will be replaced by bone tissue (Geneser 1990). During the phase of growth in childhood and adolescence, the growth in length of the bones depends on the presence of hyaline cartilage in the bone jointing. Finally, hyaline articular cartilage resides only at the surface of the joints (Geneser 1990; Mow 1997). In this location, the articular cartilage plays a very important role for the joint movement.

Articular cartilage in freely moveable joints, such as hip and knee, can withstand very large loads and is, at the same time, a smooth, lubricating material with minimal wear (Mow 1997). Articular cartilage is subjected to a wide spectrum of mechanical loading forces in vivo, which produce time varying and spatially nonuniform compressive, tensile, and shear deformations within the tissue. The ability of cartilage to withstand such deformations and to perform a physiological function depends critically on the structure, composition, and integrity of its extracellular matrix (Maroudas 1991).

Cartilage is one of the few tissues of the human body without blood vessels (Figure 2.2). Its nutrition is based on diffusion mechanisms of nutrient from capillary vessels of the surrounding connective tissue or from the synovial fluid in the articulation. In the cartilage, the transport of nutrient and of intermediate catabolic products (metabolites) occurs by means of the interstitial water of the matrix. Cartilage has neither lymphatic vessels nor nerves (Niethard 2005).

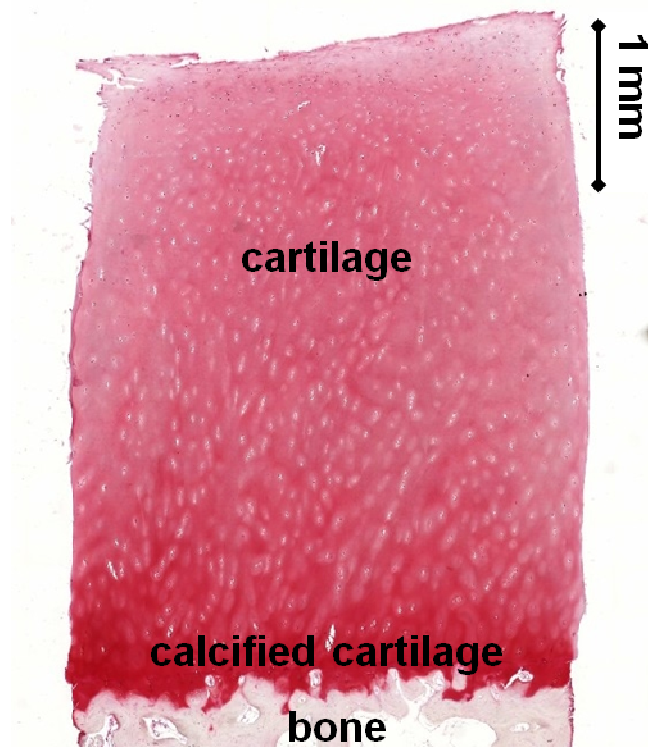


Figure 2.2: Histology of hyaline articular cartilage: cartilage has no blood vessels, nerves, or lymphatic vessels.

### 2.2.1 Morphology

Morphologically, cartilage is characterized by the cartilage cells, the chondrocytes, and by the typical extracellular substance (Figure 2.3a). The chondrocytes represent less than 5% of the cartilage volume (Pullig 2001). The extracellular substance is composed of water with dissolved ions and of collagen, proteoglycans and minerals. Water represents circa 70% of the cartilage weight and collagen represents 50% of its dry weight, i.e. circa 15% of the whole cartilage (Figure 2.3b) (Niethard 2005).

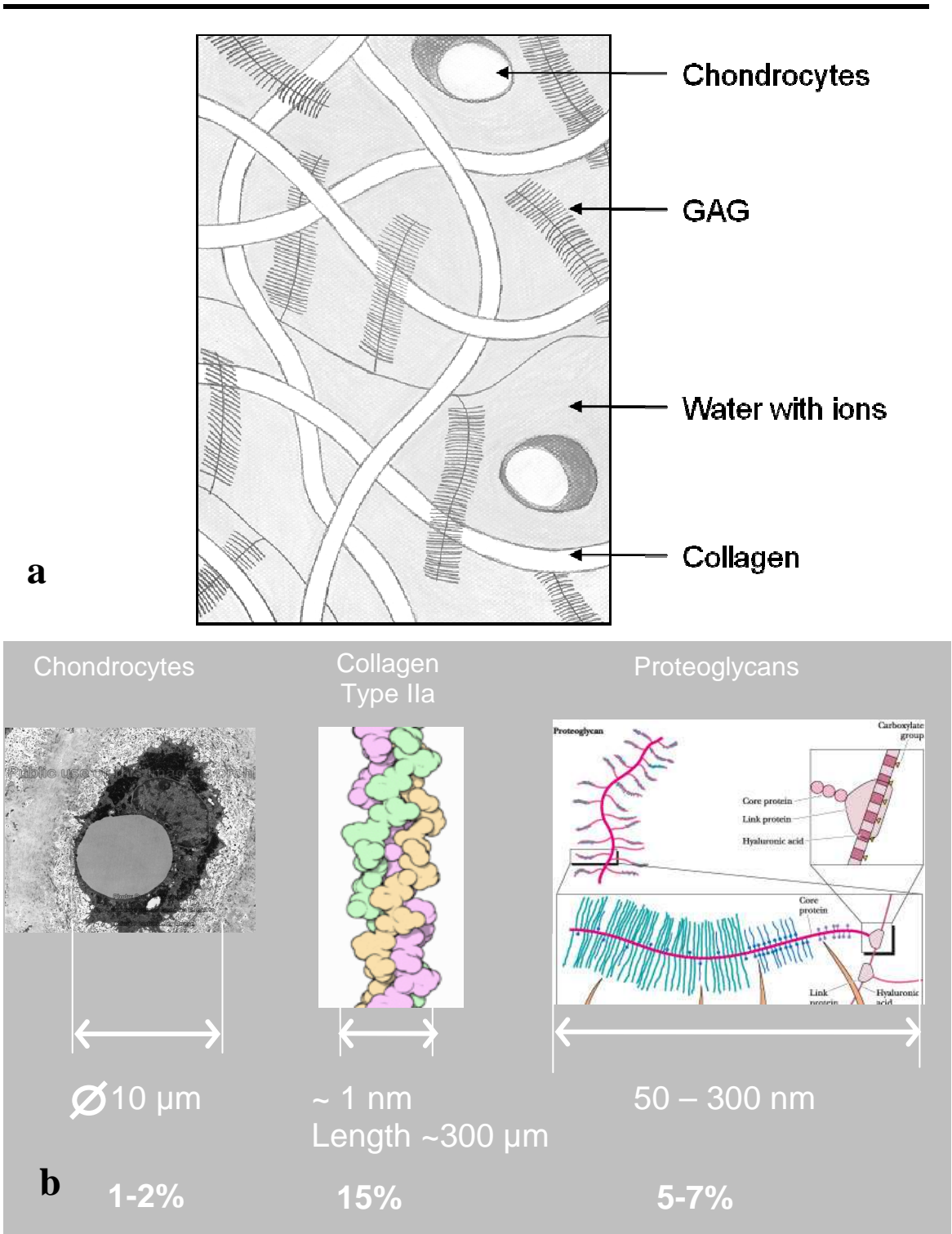


Figure 2.3: Schema of components of the articular cartilage: a) chondrocytes reside in the extracellular matrix: a compound of collagen fibrils and proteoglycan-hyaluronic acid aggregates immersed in interstitial water. b) The sizes of the

---

different components of the articular cartilage and their relative volume contents are shown (Raya 2009). The remaining volume is occupied by water.

### **2.2.2 Chondrocytes**

Chondrocytes are rounded cartilage cells that lie in the cartilage burrows. They can build cell groups that are generated through mitosis from one chondrocyte. In the chondrocytes reside abundant organelles, as RER and Golgi apparatus, important in the synthesis of proteoglycans and collagen. They synthesize the extracellular substance and are surrounded by this substance. The transport of nutritive substance and metabolite occurs through diffusion in the water of the extracellular substance. To favor the diffusion transport, chondrocytes exhibit extensions of the surface (Niethard 2005).

### **2.2.3 Collagen**

Collagen is the main protein of connective tissue in animals (Di Lullo 2002). There are at least 30 different collagen genes dispersed through the human genome.

Articular cartilage contains primarily collagen type II (Figure 2.4), with smaller amounts of types V, VI, IX and XI. They all have a basic structure of three chains forming a triple helix, but with a wide range of variation, presumably to provide for extensive differences in function (Mow 1997).

This basic structure forms the subunit tropocollagen or “collagen molecule”. In articular cartilage, type II tropocollagen molecules have about 300 nm length and are polymerized extracellularly to form collagen fibrils (Hulmes 2002; Mow 1997). Collagen II fibrils have a diameter of 100 nm in width and are embedded in the extracellular matrix.

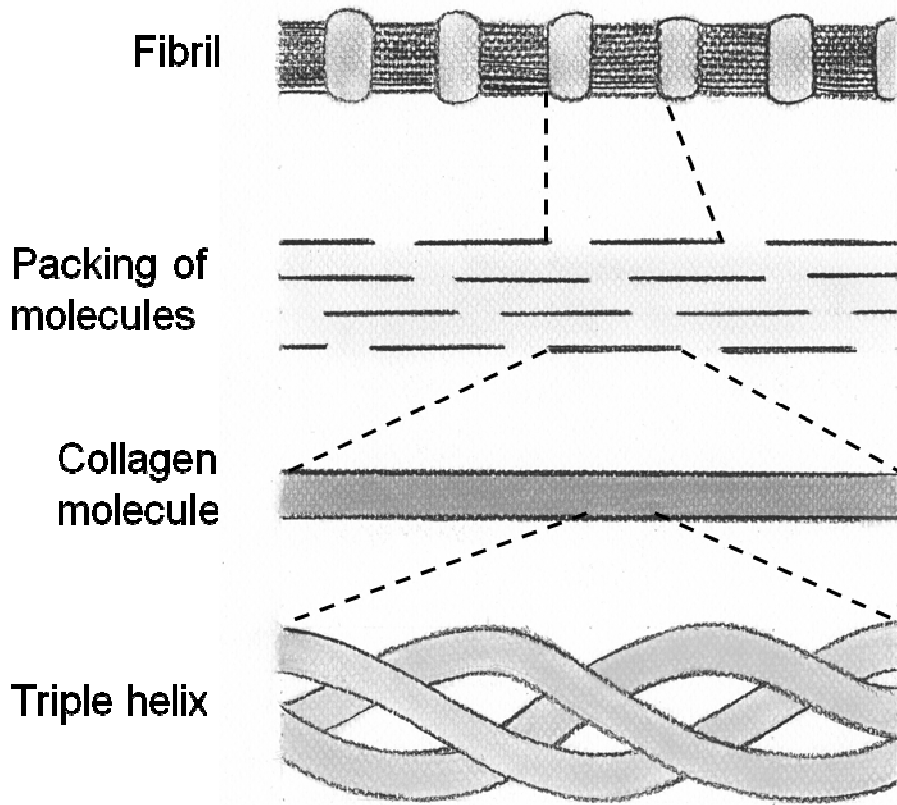


Figure 2.4: Collagen architecture: from bottom up: schematic drawing of the assembly of the triple helix into the collagen molecules, the molecules are assembled to form packing and molecule packing composes the fibrils.

In articular cartilage the primary function of the collagen appears to be providing to the tensile properties of the tissues. During the development of the embryonal connective tissue, many loads act on the extracellular substance. They cause the strain of the tissue and induce the orientation of the fibrils in the distention directions (Kummer 2005; Mow 1997).

The scanning electron microscopy (SEM) allows representing the collagen fibrils with a resolution by  $1\ \mu\text{m}$  (Figure 2.5).

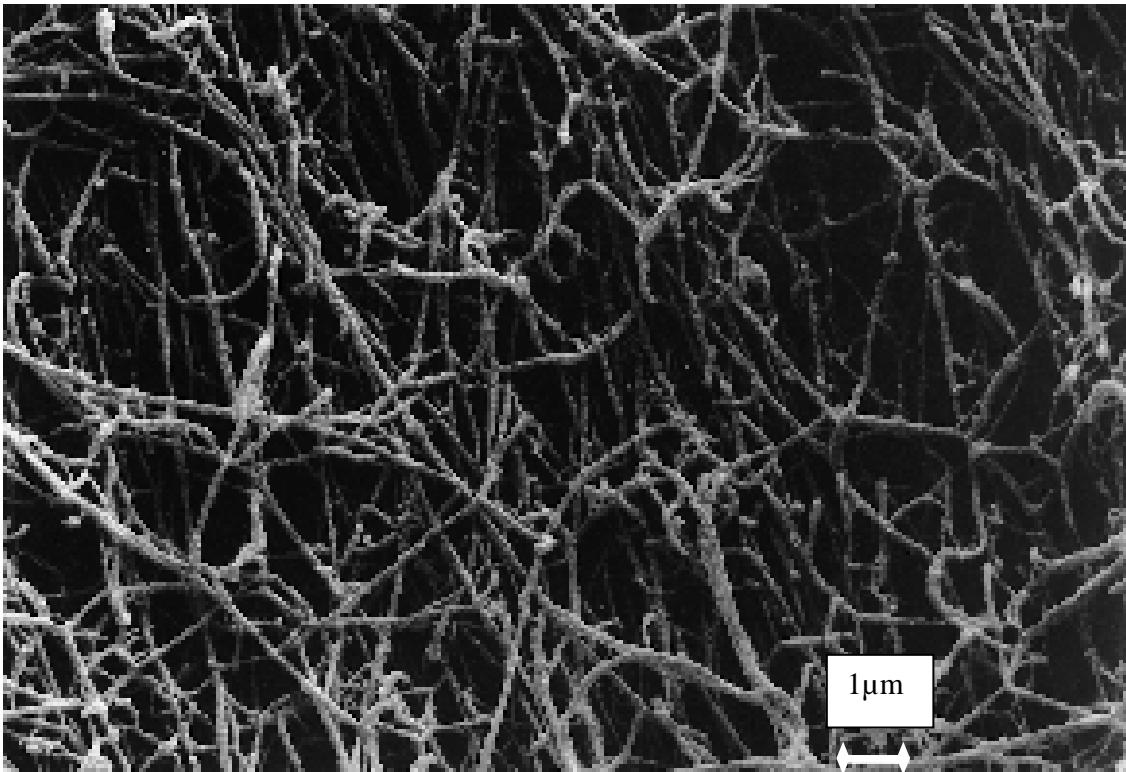


Figure 2.5: SEM image of the collagen fibrils of articular cartilage with a resolution of 1  $\mu\text{m}$  (Glaser 1998).

#### 2.2.4 Glycans

In the extracellular matrix of articular hyaline cartilage, glycans occur as “filler” substance between cells. They are polysaccharides (i.e. polymeric carbohydrate structures) and are in the form of proteoglycans and hyaluronic acid.

Proteoglycans have a structure similar to a bottle brush: a core protein with one or more covalently attached glycosaminoglycan (GAG) chain(s) (Figure 2.6a). The GAG chains are long, linear carbohydrate polymers that are negatively charged under physiological conditions. The major proteoglycan in articular cartilage is aggrecan, which has an important role in skeletal growth, joint function, and the development of OA (Mow 1997). Proteoglycans regulate the movement of molecules through the matrix (Brooks 2002; Alberts 1994).

---

Hyaluronic acids are glycan in form of a monofilament chain (Figure 2.6b). The function of hyaluronic acid is to form macromolecular aggregates with proteoglycan by means of a link protein. These structures are immobilized within the collagen network. A further function is to link the extracellular matrix with the chondrocytes (Mow 1997; Holmes 1998).

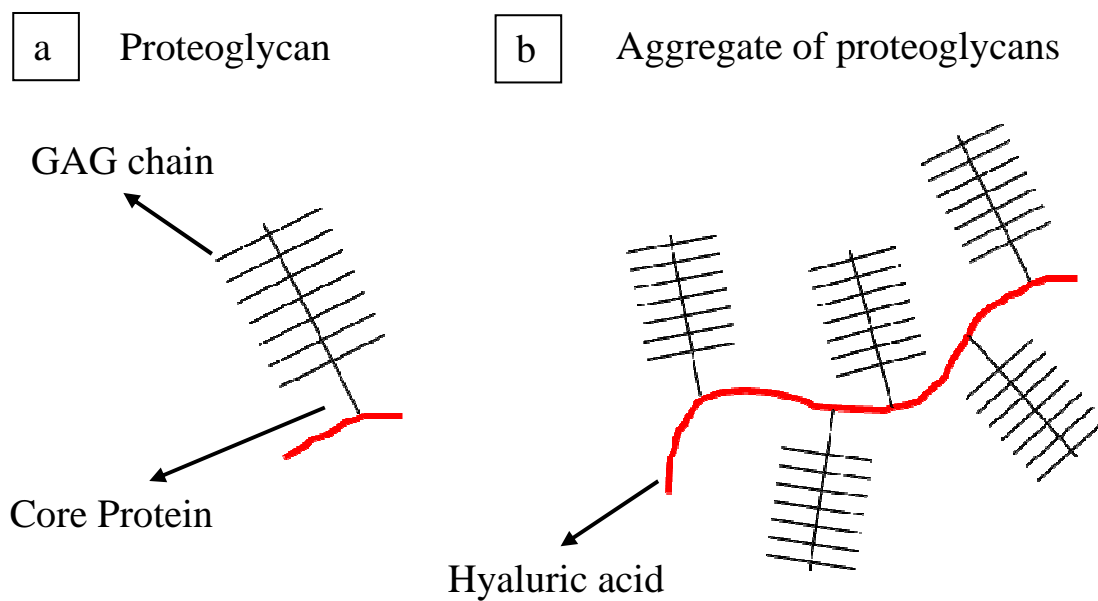


Figure 2.6: In the schema: a) single proteoglycan; b) the hyaluronic acid binds the single proteoglycans through a link protein to form a macromolecular aggregate of proteoglycans.

The electric charges of the proteoglycans provide the swelling properties of the tissue. First, the fixed negative charges are placed close together in the dense solid matrix, and so create charge-charge repulsion forces. At the same time, to maintain electroneutrality, counter-ions, i.e.  $\text{Na}^+$ , will be present and these will cause a Donnan osmotic pressure (Eisenberg 1985, Maroudas 1979). These two phenomena define the swelling pressure (Lai 1991), which has been measured and calculated to be less than 0.25 MPa (Mow 1997).

---

The swelling pressure contributes to compressive stiffness of cartilage, which usually ranges from 0.5 to 1.0 MPa depending on the type of tissue. The fixed charge density also largely determines the transport of electrolytes and electrokinetic properties of cartilage (Mow 1997).

All the proteoglycan characteristics undoubtedly will promote proteoglycan-proteoglycan networking and proteoglycan-collagen interactions in situ, which are important in stabilizing the collagen-proteoglycan solid matrix, and thus enabling it to function in the highly loaded environment of diarthrodial joints (Mow 1997).

### **2.2.5 Interstitial water**

By far, water is the most abundant component of articular cartilage (Mow 1997). It is believed that in normal cartilage, a portion of this water (approximately 30%) resides within the fibrillar space of collagen. It is known, phenomenologically, that changes in the total water content have strong influences in the mechanical, swelling and fluid transport properties exhibited by the tissue (Mow 1997). The amount of water depends largely on several factors: 1) the concentration of the proteoglycans and the resultant swelling pressure; 2) the organisation of the collagen network; and 3) the strength and stiffness of this network (Mow 1997).

The predominant ions within the interstitial fluid are sodium, chloride, potassium and calcium (Mow 1997).

### **2.2.6 Metabolic activities**

Articular cartilage, like all soft connective tissues, is metabolically active and is synthesized and maintained alive by its own cell population, the chondrocytes. The metabolic activities involve both anabolic and catabolic events, which include:

- the synthesis of matrix components;

- 
- the incorporation and organization of these components into the matrix
  - their degradation and loss from the matrix.

In summary, the cartilage extracellular matrix can be viewed as a tissue in which there is a continuous set of metabolic events occurring. Any disturbance of this carefully coordinated process may lead to deterioration of the extracellular matrix (Mow 1997).

## 2.3 Ultrastructure

The content and structure of collagen and proteoglycans within the tissue vary with the depth from the articular surface. Electron microscopic studies have shown that the tissue can be regarded as having three separate structural zones from cartilage surface to bone: tangential zone, transitional zone and radial zone (Figure 2.7) (Glaser 1998; Mow 1997).

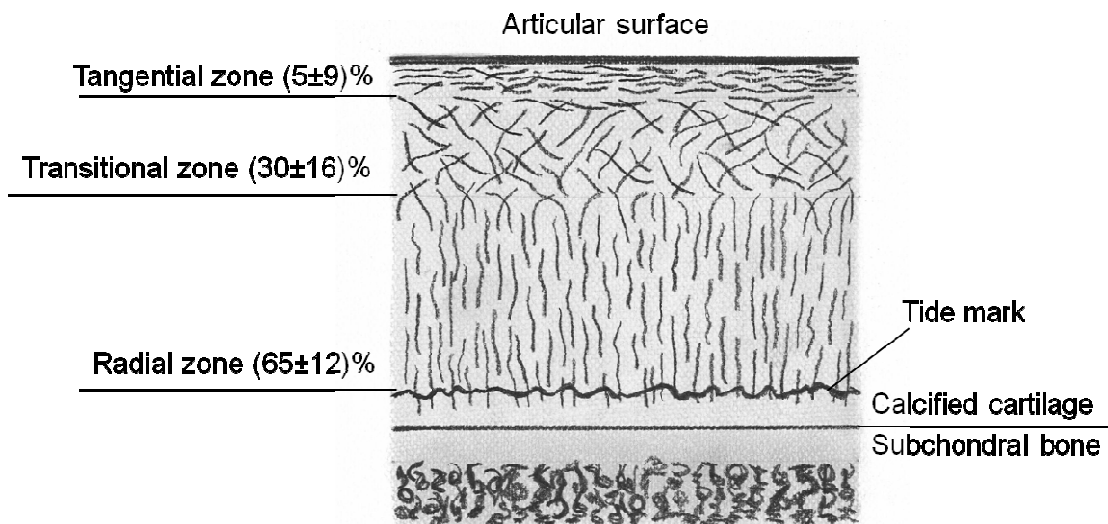


Figure 2.7: Schema of the collagen structure in articular cartilage: tangential zone at the surface, followed by the transitional zone in the middle, the radial zone and after the tidemark, the calcified cartilage. The relative thickness of the

---

respective displayed zones corresponds to those measured for the patellar cartilage with SEM (Filidoro 2008).

### **2.3.1 Tangential zone**

The tangential zone resides at the surface of the hyaline articular cartilage and obtained its name because of the parallel orientation of the collagen fibrils to the cartilage surface. This zone represents the slice with the highest concentration of collagen fibrils and the lowest content of proteoglycans. The collagen fibrils in the tangential zone are the finest in the tissue (Buckwalter 1997, Mow 1997, Clarke 1971).

The dense parallel orientation of collagen fibrils near the cartilage surface seems to have the function to distribute all possible forces on a bigger surface. The tangential zone has as well a function of mechanical protection, against external shear force and abrasion (O'Connor JJ 1993). This theory is supported by the experience that in most degenerative diseases the first pathological changes begin at the tangential slice and thereby the mechanical characteristics of the articulation are reduced (Buckwalter 1997).

### **2.3.2 Transitional zone**

Underneath the tangential zone follows the transitional zone. Here the collagen fibrils are isotropically distributed. The collagen density of approximately 68% is lower than in the tangential zone, but the content of proteoglycan is higher. The transitional zone connects the functional properties of tangential and radial zone (Buckwalter 1997, Glaser 1998).

### **2.3.3 Radial zone**

The transitional zone ends directly in the radial zone. The radial zone is characterized by an orientation of the cartilage fibrils perpendicular to surface. In the radial zone, the

---

fibrils have the largest diameter and there is the highest proteoglycan content of all cartilage (Buckwalter 1997). Due to the proteoglycan content, a high resistance to pressure is guaranteed. This indicates that the radial zone appears to have a damping function (O'Connor 1993). Furthermore, the radial zone builds the anchorage on calcified cartilage (Glaser 1998). The calcified part of cartilage resides on the subchondral bone and it is separated from the radial zone through the tide mark, where the perpendicular collagen fibrils end.

## **2.4 Osteoarthritis**

OA is a group of diseases involving degradation of joints, including articular cartilage and the subchondral bone next to it.

### **2.4.1 Epidemiology**

Degenerative articular diseases have an ample social and medical relevance. Due to their high frequency of occurrence, OA and its treatment take a central position in the health system. Starting from the third life decade, the morphologic alterations of the articular tissue in x-ray imaging increase (Niethard 2005). In Germany, one counts 5 million affected people, generally over 60 years. 300,000 patients every year undergo a replacement of the knee or hip joint (Witte 2009).

### **2.4.2 Etiology**

On the basis of the different causes of OA, primary and secondary OA can be distinguished (Brandt 2009, Valdes 2008).

Primary: This type of OA is a chronic degenerative disorder related to but not caused by aging, as there are people well into their nineties who have no clinical or functional signs of the disease. Up to 60% of OA cases are thought to result from genetic factors.

---

Secondary: Although the resulting pathology is the same as for primary OA, this type of OA is caused by other factors:

- \* Congenital disorders of joints
- \* Diabetes.
- \* Inflammatory diseases and all chronic forms of arthritis
- \* Injury to joints
- \* Septic arthritis (i.e., infection of a joint)
- \* Ligamentous deterioration or instability
- \* Obesity

In both cases, wear and tear play a very significant role, but are not the unique cause.

### **2.4.3 Pathogenesis**

The developing of degenerative joint diseases is slowly progressive. The early stage shows the loss of hyaline cartilage (Niethard 2005). This alteration of articular cartilage occurs in three phases (Figure 2.9). In the first one, the water content of the cartilage increases as a result of a deterioration of the macromolecular matrix, which may be caused by a modified metabolism of the chondrocytes. The proteoglycan concentration decreases, whereas the collagen content remains constant (Mankin 1974). In the second phase, the chondrocytes perceive the presence of a lesion and then increase the synthesis, as “repair-effect” (Mankin 1974). Extending over several years, in consequence of increased synthesis, the nutrient supply for the chondrocytes declines. As result of the altered activity, the cartilage molecules can no longer provide to the maintenance of the extracellular matrix: this situation corresponds to the third phase (Mankin 1974).

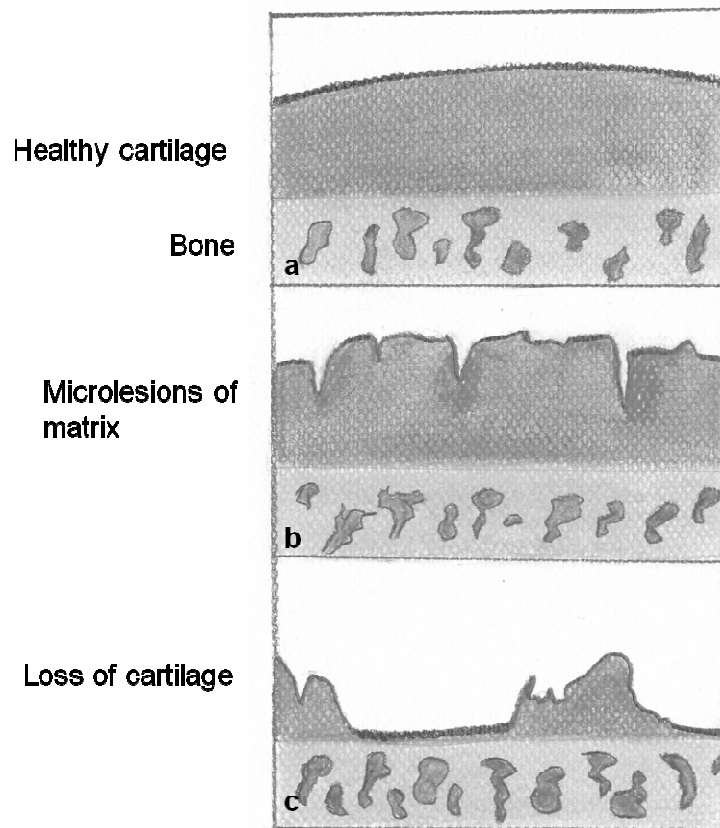


Figure 2.9: Schema of the phases of the pathogenesis of the OA in cartilage: from healthy cartilage (a), the clinical latent arthritis (b) becomes clinical activated arthritis (c) through enzymatic process.

Loss of integrity of the collagenous fibril network is considered to be the hallmark of transition from potentially reversible to irreversible degeneration of articular cartilage long before macroscopically visible loss of cartilage substance occurs (Buckwalter 1997). The articular cartilage loses more and more volume and function.

Following and due to the cartilage degradation, the correspondent bone degenerates, cysts develop and OA will be relevant (Niethard 2005) (Figure 2.10).

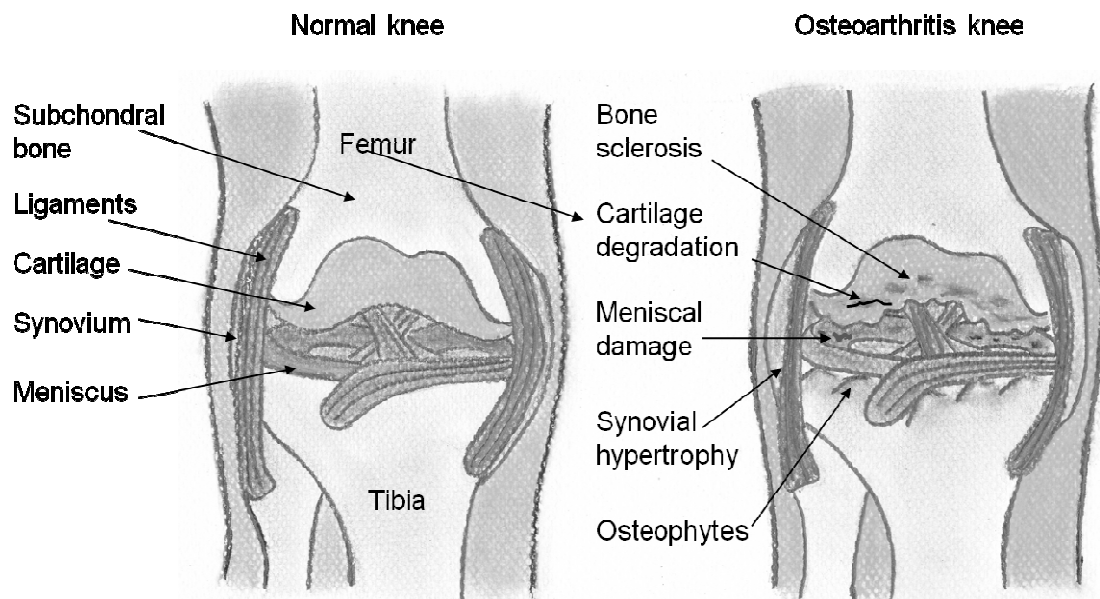


Figure 2.10: Pathogenesis of OA in knee joint: comparison between knee in healthy state and knee with OA. The entire joint is involved.

#### 2.4.4 Symptoms

Clinical manifestations of OA may include joint pain, tenderness, stiffness, creaking, locking of joints, and sometimes local inflammation (Niethard 2005).

#### 2.4.5 Diagnosis

In the early stage of OA diagnosis is obtained by anamnesis and the results of clinical examination, later on by analysis of alterations in x-ray images (Niethard 2005).

#### 2.4.6 Early diagnosis

Loss of integrity within the collagenous fibril network is considered to be the hallmark of transition from potentially reversible to irreversible degeneration of articular cartilage. Since the cartilage tissue is not connected to the nervous system, the pain

---

symptoms appear only when the disease is already advanced and other structures of the joint are affected. On account of this, many efforts are aimed to optimize the early diagnosis of OA in hyaline cartilage. Prerequisite of an investigation method for the early diagnosis is the capacity to analyze the tissue in healthy condition. The surgical invasive arthroscopy allows investigating the surface status and the elasticity of the cartilage, but is not sufficient to describe the (internal) structure of the cartilage matrix. Conventional methods of radiography and x-ray computed tomography (CT) offer an estimation of cartilage thickness or cartilage pathological deformations, but are not adequate to show the cartilage structure. Otherwise, MRI is the most efficient technique for the representation and evaluation of the cartilagenous structure, also in the healthy conditions (Glaser 2006).

#### **2.4.7 Therapy**

In the past forty years, many efforts were made to antagonize the progressive loss of cartilage. In addition to the pharmacologic approach, surgical solutions were attempted, as transplantation of chondrocytes or of cartilage extracellular matrix, to reduce the suffering of the patient. (Buckwalter 1997) Such implants will be rarely rejected from the immune system and they have the ability to stimulate the formation of cartilage tissue (Geneser 1990; Buckwalter 1997). However, no treatment guarantees a long-term rebuilding of the cartilage.

---

## **3 Magnetic resonance imaging (MRI) of molecular diffusion**

### **3.1 Introduction**

Magnetic resonance imaging (MRI) is an imaging technique used primarily in medical settings to produce high quality images of the inside of the human body. MRI is based on the principles of nuclear magnetic resonance (NMR), a spectroscopic technique used to obtain microscopic chemical and physical information about molecules. MRI started out as a two-dimensional tomographic imaging technique, i.e., it produced an image of the NMR signal in a thin slice through the human body. Later on, MRI has advanced beyond a tomographic imaging technique to a three-dimensional volume imaging technique (Hornak 2010).

The concept of nuclear magnetic resonance had its underpinnings with the discovery of the spin nature of the proton. Based on the work of Stern and Gerlach (Gerlach and Stern 1924) as well as of Rabi and coworkers (Rabi 1938), Bloch and Purcell (Bloch 1946; Purcell 1946) performed the first measurements of nuclear magnetic resonance effects of precessing spins in a magnetic field (Haacke 1999).

The physical basic principle for the magnetic resonance is that the intrinsic angular momentum (spin) of the atom nuclei in a magnetic field precesses about the field direction at the ‘Larmor frequency’, which, in turn, depends linearly on the magnitude of the magnetic field itself (Haacke 1999). The idea of Lauterbur and Mansfield (Lauterbur 1973; Mansfield 1973) was that if a spatially varying magnetic field is

---

introduced across the object, the Larmor frequencies are also spatially varying. They proposed and showed that the different frequency components of the signal could be separated to give spatial information about the object. This key point of spatially encoding the data opened the door to MR imaging (Haacke 1999).

Diffusion is essentially a random walk of molecules in a medium. In the presence of a magnetic field gradient, diffusion of water molecules causes a phase dispersion of the transverse magnetization, resulting in the attenuation of the MRI signal (Carr and Purcell 1954; Stejskal and Tanner 1965). The degree of signal loss depends on tissue type, structure, physical and physiological state, as well as on the microenvironment. MRI data acquisition methods that are designed to explore tissue diffusion are called diffusion imaging (Le Bihan 1986, Basser 1994). In diffusion imaging, the apparent diffusion coefficient (ADC) for a determined direction can be calculated, where the term apparent refers to the dependence of this coefficient on (biological) factors other than prior molecular mobility (Le Bihan 1995).

However, in anisotropic media, such as skeletal and cardiac muscle and white matter, where the measured diffusivity is known to depend on the orientation of the tissue, no single ADC can characterize the orientation-dependent water mobility. Diffusion tensor imaging is a technique that measures the spatial orientation anisotropy of the diffusion process (Pierpaoli 1996). It requires six or more independent diffusion gradients directions to produce a set of diffusion-weighted images sufficient to fully describe the orientation-dependent water mobility (Bernstein 2004). These diffusion-weighted images can be converted to scalar and vector maps that describe a variety of tissue diffusion properties.

---

## 3.2 Diffusion-weighted imaging (DWI)

### 3.2.1 Theory of diffusion

Molecular diffusion is a stochastic thermal phenomenon (Reif 1987). The diffusion of a substance is quantified by the constant tensor  $\mathbf{D}$ . If the concentration  $n(\mathbf{r}, t)$  of the substance is not homogeneous, a flux density  $\mathbf{J}$  is observed. The relation between  $n(\mathbf{r}, t)$  and  $\mathbf{J}$  is given by Fick's law:

$$\mathbf{J} = -\mathbf{D} \nabla n. \quad (3.1)$$

With the request that the number of particles remains constant, we obtain the equation of continuity

$$\partial n / \partial t = -\nabla \cdot \mathbf{J}. \quad (3.2)$$

And so we obtain the diffusivity equation:

$$\partial n / \partial t = \nabla \cdot (\mathbf{D} \nabla n). \quad (3.3)$$

For an isotropic medium, where  $\mathbf{D} = D\mathbf{1}$ , the diffusivity equation will be:

$$\partial n / \partial t = D \Delta n \quad (3.4)$$

and the behavior of the unrestricted diffusion is described by the Einstein equation:

$$r_{\text{rms}} = \sqrt{(6Dt)} \quad (3.5)$$

This relates the three-dimensional root-mean-square displacement  $r_{\text{rms}}$  to the diffusion time  $t$  and the diffusion coefficient  $D$ , where  $D$  is expressed in  $\text{mm}^2/\text{s}$ . Equation (3.5) is also valid, if the flux density is zero. This is the case of self-diffusion of water molecules in water.

### 3.2.2 Measurement principles

The principle of the diffusion measurement is based on the introduction of opposite magnetic field gradients in the MRI pulse sequence, which, due to the diffusion of water molecules, causes a phase dispersion of the transverse magnetization, resulting in the attenuation of the MRI signal (Figure 3.1) (Carr and Purcell 1954, Stejskal and Tanner 1965).

From the knowledge of the signal attenuation, it is possible to obtain a map of the diffusion coefficient  $D$ . The conventional measurement method in diffusion-weighted MR imaging is the Stejskal-Tanner pulse sequence (Stejskal and Tanner 1965). The Stejskal-Tanner method for the case of spin echo is shown in Figure 3.1:

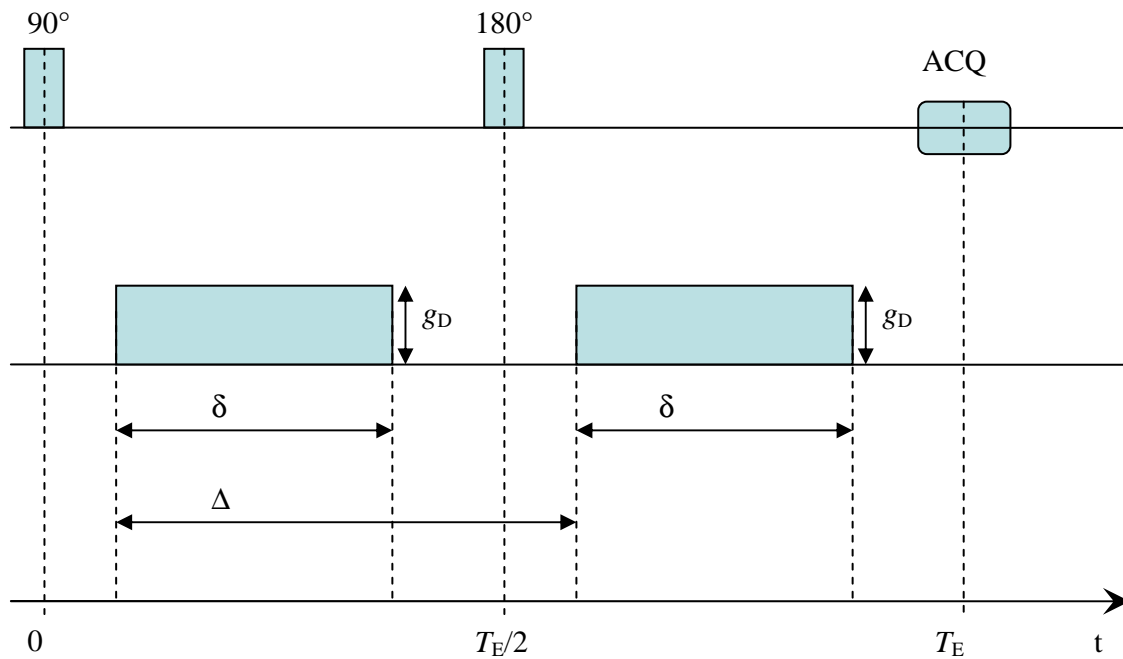


Figure 3.1: The sequence timing diagram illustrates the diffusion pulse sequence introduced by Stejskal and Tanner: its characteristic features are two strong symmetric gradient lobes placed on either side of the  $180^\circ$  refocusing pulse in a spin-echo sequence.  $\delta$  is the gradient duration and  $\Delta$  is the interval time between the onsets of the pulses.

Two diffusion-weighting gradients are incorporated into the spin-echo sequence. Both gradients have equal area, i.e. the same amplitude  $g_D$  and the same duration  $\delta$ ; they have the same polarity and are placed at either side of a refocusing radio frequency (RF) pulse, with interval time  $\Delta$  between the onsets of the pulses (Bernstein 2004). The first diffusion gradient induces the spins to dephase as a result of the Larmor frequency dependent on the position. If all spins remained at their original position, the second

diffusion gradient would rephase every spin. But due to the molecular diffusion, some spins will change their position in the direction parallel to the direction of the magnetic gradient  $g_D$ , and hence will not be fully refocused. In this case, a loss of phase coherence occurs. The macroscopic transversal magnetization will be attenuated dependent on the intensity of the diffusion.

Combining the Bloch's equations (Bloch 1946) with the diffusion equation, Stejskal and Tanner describe the transversal magnetization by the equation:

$$d/dt \mathbf{M}_T(\mathbf{r},t) = \gamma \mathbf{M}_T(\mathbf{r},t) \times \mathbf{B} - 1/T_2 \mathbf{M}_T(\mathbf{r},t) + D \Delta \mathbf{M}_T(\mathbf{r},t) \quad (3.6)$$

where  $\mathbf{M}_T(\mathbf{r},t)$  is the transversal magnetization and  $\mathbf{B}$  is the main magnetic field.

Analytic expressions have been derived for the pulse sequence shown above, which relate the measured signal intensity to the diffusion coefficient.

For isotropic media, the magnitude of the magnetization at the time of the echo  $T_E$ ,  $A(T_E)$ , is related to the scalar diffusion coefficient,  $D$ , by:

$$\ln(S(T_E)/S(0)) = -\gamma^2 \int_0^{T_E} (\mathbf{F}(t') - 2H(t' - T_E/2) \mathbf{f})^T \cdot D (\mathbf{F}(t') - 2H(t' - T_E/2) \mathbf{f}) dt'. \quad (3.7)$$

Above,  $\gamma$  is the gyromagnetic ratio of protons,  $S(0)$  is the initial transverse magnetization (at  $t=0$ ) just after the  $90^\circ$  pulse is applied, and  $H(t)$  is the Heaviside step function. In addition,

$$\mathbf{G}(t) = (G_x(t), G_y(t), G_z(t))^T \quad (3.8)$$

is the applied magnetic field gradient (column) vector, and  $\mathbf{F}(t)$  is defined as

$$\mathbf{F}(t) = \int_0^t \mathbf{G}(t') dt'; \quad \mathbf{f} = \mathbf{F}(T_E/2). \quad (3.9)$$

After the integration, the relationship between the diffusion coefficient and the logarithm of the echo intensity can be written as

$$\ln(S(T_E)/S(0)) = -b D \quad (3.10)$$

(in vivo it would be more exact to introduce  $\mathbf{D}_{\text{effective}}$ ) where the factor  $b$  is

$$b = \gamma^2 \int_0^{T_E} (\mathbf{F}(t') - 2H(t' - T_E/2) \mathbf{f})^T \cdot (\mathbf{F}(t') - 2H(t' - T_E/2) \mathbf{f}) dt'. \quad (3.11)$$

For rectangular gradient lobes in a spin-echo pulse sequence, the factor  $b$  is given by:

$$b = \gamma^2 G^2 \delta^2 (\Delta - \delta/3) \quad (3.12)$$

The degree of attenuation of the signal depends on the dimensionless product of the diffusion coefficient  $D$  and on the factor  $b$ , a quantity known as the b-value (in seconds

---

per millimeter square). The b-value is determined by the diffusion-weighting gradient waveform and can be adjusted in the pulse sequence. Increasing the diffusion gradient amplitude, the separation between both diffusion gradient, or the pulse width of each diffusion gradient, results in a higher b-value. (Bernstein 2004).

It is also possible to write:

$$S = S_0 \exp(-b D) \quad (3.13)$$

where  $S$  and  $S_0$  are the voxel signal intensity with and without diffusion weighting, respectively.

If we consider two different b-values  $b_1$  and  $b_2$ , from equation (3.13) we obtain:

$$S_1/S_2 = \exp(b_2 D) / \exp(b_1 D) = \exp((b_2 - b_1) D) \quad (3.14)$$

where  $S_1$  and  $S_2$  are the voxel signal intensity for  $b_1$  and  $b_2$ , respectively.

### 3.2.2 Apparent diffusion coefficient (ADC)

When various barriers and restricting factors such as cell membranes and microtubules interfere with the free diffusion and tissue perfusion, and partial volume averaging as well as other experimental errors (Le Bihan 1995) are present in the voxels, the diffusion coefficient  $D$  determined over the diffusion-sensitive interval  $\tau \approx \Delta - \delta/3$  is different from the diffusion coefficient of free water. We are measuring the ADC, the “apparent diffusion coefficient”, because the measurement misses all the local effects and treats it as if all the movement rates were solely due to Brownian motion. This is the case of microscopically heterogeneous, but macroscopically isotropic media (Basser 1994). Whereas in free water, the root-mean-square displacement  $r$  increases proportional to  $\sqrt{\tau}$ , in a porous medium the displacement will be limited by the porous walls. For the limit  $\tau \rightarrow \infty$ , for restricted diffusion and in absence of tissue perfusion, ADC equals a limit value  $D_\infty$ , dependent on the porosity of the medium (Tanner 1978).

---

## 3.3 Diffusion tensor imaging (DTI)

### 3.3.1 Determination of the diffusion tensor

In anisotropic media, such as skeletal and cardiac muscle (Cleveland 1976, Garrido 1994, Turner 1979) and in white matter (Henkelmann 1994, Moseley 1990, Moseley 1991), where the measured diffusivity is known to depend on the orientation of the tissue, no single ADC can characterize the orientation-dependent water mobility in these tissues. The next more complex model of diffusion that can describe anisotropic diffusion is to replace the scalar diffusion coefficient by a diffusion tensor of water,  $\mathbf{D}$  (Basser 2002). The MRI measurement of the diffusion tensor and the analysis and display of the information contained in each voxel, is called diffusion tensor imaging (DTI). The diffusion tensor,  $\mathbf{D}$ , is estimated from a series of diffusion-weighted images using a relationship between the measured echo attenuation in each voxel and the applied magnetic field gradient sequence. Just as in diffusion imaging, where a scalar b-value is calculated for each diffusion-weighted image, in DTI a symmetric b-matrix is calculated for each diffusion-weighted image. Whereas the b-value summarizes the attenuating effect on the MR signal of all diffusion and imaging gradients in one direction, the b-matrix summarizes the attenuating effect of all gradient waveforms applied in all three directions,  $x$ ,  $y$  and  $z$ .

With the diffusion tensor  $\mathbf{D}$ , equation (3.10) is generalized to:

$$\ln(S/S_0) = -\sum_{i=1}^3 \sum_{j=1}^3 b_{ij} D_{ij} \quad (3.15)$$

(in vivo it would be more exact introduce  $\mathbf{D}_{\text{eff}}$ ) where the  $b_{ij}$  are elements of the b-matrix,  $\mathbf{b}$  (Basser 1994) defined as

$$\mathbf{b} = \gamma^2 \int_0^{TE} (\mathbf{F}(t') - 2H(t' - T_E/2) \mathbf{f}) \cdot (\mathbf{F}(t') - 2H(t' - T_E/2) \mathbf{f})^T dt'. \quad (3.16)$$

There are two important distinctions between DWI and DTI. First, DWI is a one-dimensional technique, therefore it is sufficient to apply diffusion gradients along only one direction. DTI is three-dimensional: one has to apply diffusion gradients along at least six non-collinear, non-coplanar directions in order to provide enough information to estimate the six independent elements of the symmetric diffusion tensor. Second, the

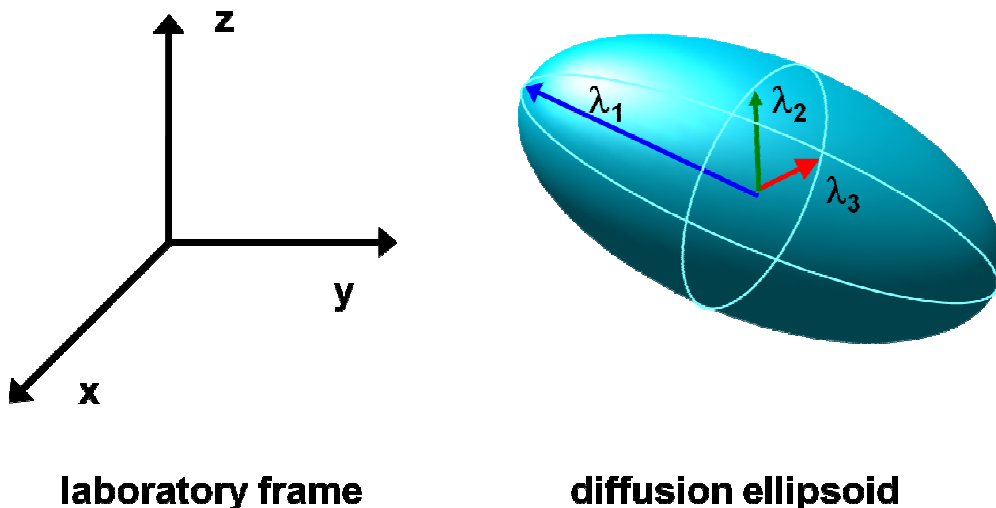
---

b-matrix formalism forces us to expand the notion of ‘cross-term’ effects between imaging and diffusion gradients that are applied in orthogonal directions, and even between imaging gradients that are applied in orthogonal directions. In isotropic media, gradients applied in orthogonal directions do not result in cross-term effects; in anisotropic media, however, they can (Basser 2002).

### 3.3.2 Quantitative parameters obtained by DTI

By diagonalization of the diffusion tensor obtained from equation 3.15, the characteristic values or eigenvalues of the tensor are calculated. Each eigenvalue  $\lambda_i$  ( $i=1,2,3$ ) corresponds to a characteristic vector or eigenvector  $\lambda_i$ . The eigenvectors and eigenvalues represent the three principal directions of diffusion and their magnitudes within the tissue.

If one eigenvalue is considerably larger than the other two (such as in the case of the white-matter fiber tracts in the brain), the largest eigenvalue is referred to as the principal diffusion coefficient and its eigenvector is aligned along the principal diffusion direction. This scenario is graphically represented by the diffusion ellipsoid (Figure 3.2) (Pierpaoli and Basser1996).



---

Figure 3.2: Peter J. Basser, James Mattiello and Denis Le Bihan showed how the classical ellipsoid tensor formalism could be deployed to analyze diffusion MR data. The three axes of the ellipsoid are now directly along the main orthogonal axes of the coordinate system so we can easily infer their lengths. These lengths are the eigenvalues or characteristic values (Picture with kind permission of Olaf Dietrich).

Anisotropic diffusion can be described by a diffusion ellipsoid with the semiaxes equal to the amplitude of the diffusion tensor eigenvalues  $\lambda_1, \lambda_2, \lambda_3$  (Bernstein, 2004).

Eigenvalues, eigenvectors, and parameters derived from these are rotationally invariant quantities; that is, they have the same numerical value if the matrix is expressed in a rotated coordinate system (Basser 1994, Basser 1992).

For example, each eigenvalue can be used to form its own map to show the ADC along each axis of the diffusion ellipsoid.

The first moment of the diffusion tensor field, the orientationally averaged value of the diffusion tensor field can be calculated at each point within an imaging volume as:

$$\langle \lambda \rangle = \text{Trace}(\mathbf{D})/3 = (\lambda_1 + \lambda_2 + \lambda_3)/3. \quad (3.17)$$

This is the mean diffusivity. Physically, an estimate of  $\langle \lambda \rangle$  can be obtained by taking the arithmetic average of ADCs acquired in all possible directions (Kärger 1988).

The second and higher moments of  $\mathbf{D}$  have been proposed for use as diffusion anisotropy measure, because they characterize different ways in which the diffusion tensor field deviates from being isotropic. This has resulted in a number of diffusion anisotropy measures based upon the second moment of the distribution of the eigenvalues of  $\mathbf{D}$ :

$$\alpha = (\lambda_1 - \langle \lambda \rangle)^2 + (\lambda_2 - \langle \lambda \rangle)^2 + (\lambda_3 - \langle \lambda \rangle)^2, \quad (3.18)$$

which characterize the eccentricity of the diffusion ellipsoid. (Basser 2002).

Such diffusion anisotropy measures are the relative anisotropy (RA)

$$\text{RA} = (\alpha / 3 \langle \lambda \rangle^2)^{1/2}, \quad (3.19)$$

the fractional anisotropy (FA)

---

$$FA = (3\alpha / 2\beta)^{1/2} \quad (3.20)$$

where

$$\beta = \lambda_1^2 + \lambda_2^2 + \lambda_3^2 \quad (3.21)$$

and the volume ratio (VR)

$$VR = \lambda_1 \lambda_2 \lambda_3 / \langle \lambda \rangle^3. \quad (3.22)$$

Both RA and FA are based on the standard deviation of the eigenvalues, but they are normalized by different denominators and coefficients. Relative anisotropy ranges from 0 to  $\sqrt{2}$ . Fractional anisotropy, which has values ranging from 0 to 1, has been found to be more sensitive than RA at low values of anisotropy (Pierpaoli and Basser 1996, Ulug and van Zijl 1999).

---

## 4 DTI of cartilage at 9.4 Tesla

### 4.1 Introduction

The first part of this work considers the application of DTI in articular cartilage from the human patella (Figure 4.1), employing a 9.4-T MR scanner. It was the first time that this application was realized. Therefore, the purposes of this study were to 1) assess the feasibility of DTI for analyzing human hyaline articular cartilage, and 2) evaluate whether DTI can demonstrate zonal architectural properties of articular cartilage.

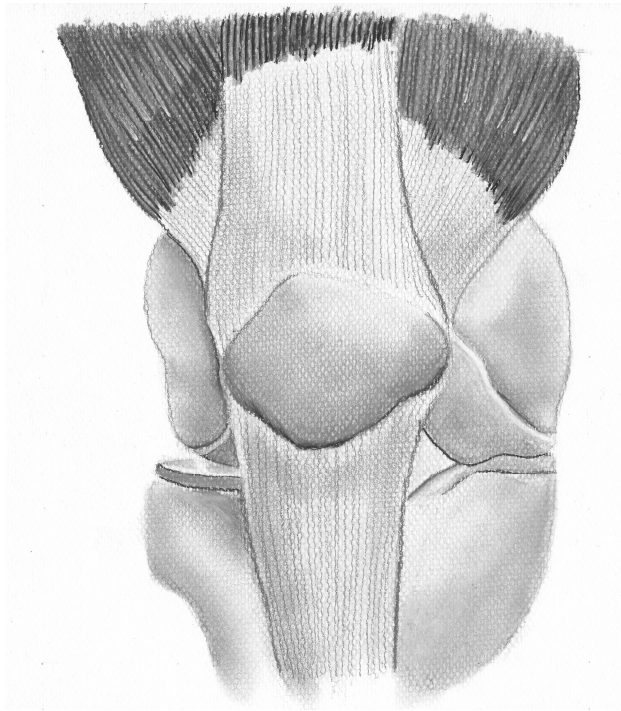


Figure 4.1: The patella is a thick, circular-triangular bone which articulates with the femur and covers and protects the anterior articular surface of the knee joint. It is the largest sesamoid bone in the human body.

---

## 4.2 Materials & Methods

### 4.2.1 Sample preparation

MRI measurements were performed on human patellar cartilage-on-bone samples (Figure 4.2). The patellae were harvested within 48 h after death (Dept. of Forensic Medicine, LMU Munich) from three individuals (mean age:  $47\pm 5$  years). Only patellae with a macroscopically normal aspect of the cartilage without any signs of OA were imaged. Cylindrical cartilage-on-bone samples (diameter 7 mm) were drilled from the center of the lateral patellar facets of three patellae for MRI. The use of a small water-level ensured that drilling was achieved perpendicular to the cartilage surface. During drilling the patellae were continuously rinsed with physiological saline. For MRI, the samples were put in a hollow Plexiglas cylinder (free inner diameter = 7 mm, outer diameter = 10 mm) filled with physiological saline. The cylinder was adapted to and closely fixed within the resonator of the MR system to prevent motion artifacts. The samples were oriented with their surface perpendicular to the main magnetic field.



Figure 4.2: Preparation of the sample. **a:** In the MR laboratory the samples were prepared for the MR measurement. **b:** The drilling apparatus and the patella will be hold stable in their positions using screw clamps. **c:** The patella was catalogued: it was cleaned with NaCl solution, checked for any signs of OA and then photographed. **d:** The patella was fixed under the drill, ensuring through a small water-level that drilling was achieved perpendicular to the cartilage surface. During drilling, the patellae were continuously rinsed with physiological saline. **e:** Cylindrical cartilage-on-bone samples.

---

## 4.2.2 MRI

### Imaging protocol

A 9.4-T magnet (Bruker Microimaging Systems, Rheinstetten, Germany) (Figure 4.3) with a maximum gradient strength of 1 T/m was used.



Figure 4.3: A 9.4-T magnet (Bruker Microimaging Systems, Rheinstetten, Germany) was used for the MRI experiment. Its main magnetic field was vertically oriented. The high magnetic field allows microscopy measurements (Picture with kind permission of Thomas Örtner).

---

We acquired DTI data applying a diffusion-weighted pulsed-gradient spin-echo sequence provided by the manufacturer. Repetition time (TR) was 2000 ms and TE was 11 ms. Diffusion gradient pulses had a duration  $\delta$  of 2.1 ms, and the time interval  $\Delta$  between the onsets of the pulses was 3.7 ms. Two measurements (Figure 4.4) with a b-value of 0 s/mm<sup>2</sup> and 12 measurements with a b-value of 1000 s/mm<sup>2</sup>, applying diffusion-sensitizing gradients in 12 isotropically distributed directions, were performed. Using a 10 × 10 mm<sup>2</sup> field of view (FOV) and a 256 × 128 matrix, a spatial resolution of 39×78×1500  $\mu\text{m}^3$  was achieved, providing 80 – 100 pixels from the surface of the cartilage to the tide mark. The total acquisition time (18 averages) was 15 hours.

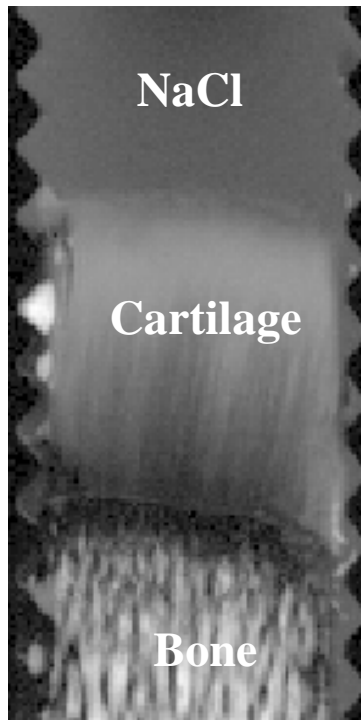


Figure 4.4: For MRI measurements, the samples were put in a hollow Plexiglas cylinder (free inner diameter = 7 mm, outer diameter = 10 mm) filled with physiological saline. The diffusion measurement with  $b = 0$  gives a  $T_2$ -weighted image: saline solution (NaCl), cartilage and bone were well distinguishable.

---

## Imaging processing

For evaluation and visualization of the DTI data, an AVS-based (Advanced Visual Systems Inc., Waltham, Massachusetts, USA) software package (programming language: C) was developed. We kept the evaluated number of different diffusion directions used for the diffusion tensor calculation variable between the required minimum of 6 (Basser 1998; Basser 1994-b; Jones 1999) and the maximum available 12 directions in order to be able to reject certain diffusion directions in case of artifacts in the measurements.

We calculated the diffusion eigenvectors and the corresponding diffusion eigenvalues ( $\lambda_1$ ,  $\lambda_2$ ,  $\lambda_3$ ) by diagonalizing the diffusion tensor. These quantities are independent of the scanner coordinates, and represent the three principal directions of diffusion and their magnitudes within the tissue, as mentioned above.

From these eigenvalues, the mean diffusivity (corresponding to ADC) and FA were determined using equations (3.17) and (3.20).

All parameters were calculated pixel-wise for the whole cross-sectional area of the cartilage determined by manual segmentation in standard  $T_2$ -weighted MR images. The mean diffusivity and FA were visualized as grayscale parameter maps (Figure 4.5a and 4.6a) and as a function of the normalized distance from the cartilage surface to the cartilage-bone interface (Figure 4.5b - e and 4.6b - e). For the latter, nine horizontally oriented rectangular regions of interest (ROIs) (each covering 11% of the individual sample's cartilage depth) were projected over the cross section of each sample and mean and standard deviation of each ROI were calculated as representative values for the diffusivity and FA in each depth in the cartilage. The first eigenvector (i.e., the eigenvector corresponding to the largest directional diffusivity) was visualized by projection on the MR section plane (Figure 4.7). Any line represents the main orientation (not its magnitude) of water movement within the cartilage matrix.

Additionally, we estimated the signal-to-noise ratio (SNR) in the cartilage. In our experiments, a volume coil (single receiver channel) was used and the reconstruction

---

was realized by Fourier transform with subsequent magnitude calculation. For a single receiver channel, without filter, the signal will be then described by a Rician distribution in general and a Rayleigh distribution in the image background (Edelstein 1984; Kellman 2005). Hence, the SNR was calculated as the quotient of the averaged signal intensity at  $b = 0$  in a rectangular ROI in the cartilage and the standard deviation in a ROI of a region without signal. The SNR of the cartilage was visualized as a function of the normalized distance from the cartilage surface to the cartilage-bone interface (Figure 4.8).

### 4.3 Results

All three samples showed comparable behavior of mean diffusivity, FA, and the eigenvector corresponding to the largest eigenvalues.

The mean diffusivity (Figure 4.5) was highest close to the cartilage surface, and showed a decrease from  $(1.28 \pm 0.14) \times 10^{-3} \text{ mm}^2/\text{s}$  at the cartilage surface down to  $(0.74 \pm 0.19) \times 10^{-3} \text{ mm}^2/\text{s}$  at the cartilage-bone interface. The mean diffusivity of the physiological saline surrounding the cartilage was  $2.26 \times 10^{-3} \text{ mm}^2/\text{s}$ . Signal attenuation in NaCl was homogeneous with a coefficient of variation (COV) of 2.5% in the different diffusion directions indicating sufficient gradient calibration.

In contrast to the clear gradient of mean diffusivity along an axis perpendicular to the cartilage surface, no systematic variation in mean diffusivity could be detected parallel to the cartilage surface (average COV: 3%). The highest change in mean diffusivity (as plotted against the normalized distance from the cartilage surface, Figure 4.5b - e) occurred in the lower half of the cartilage.

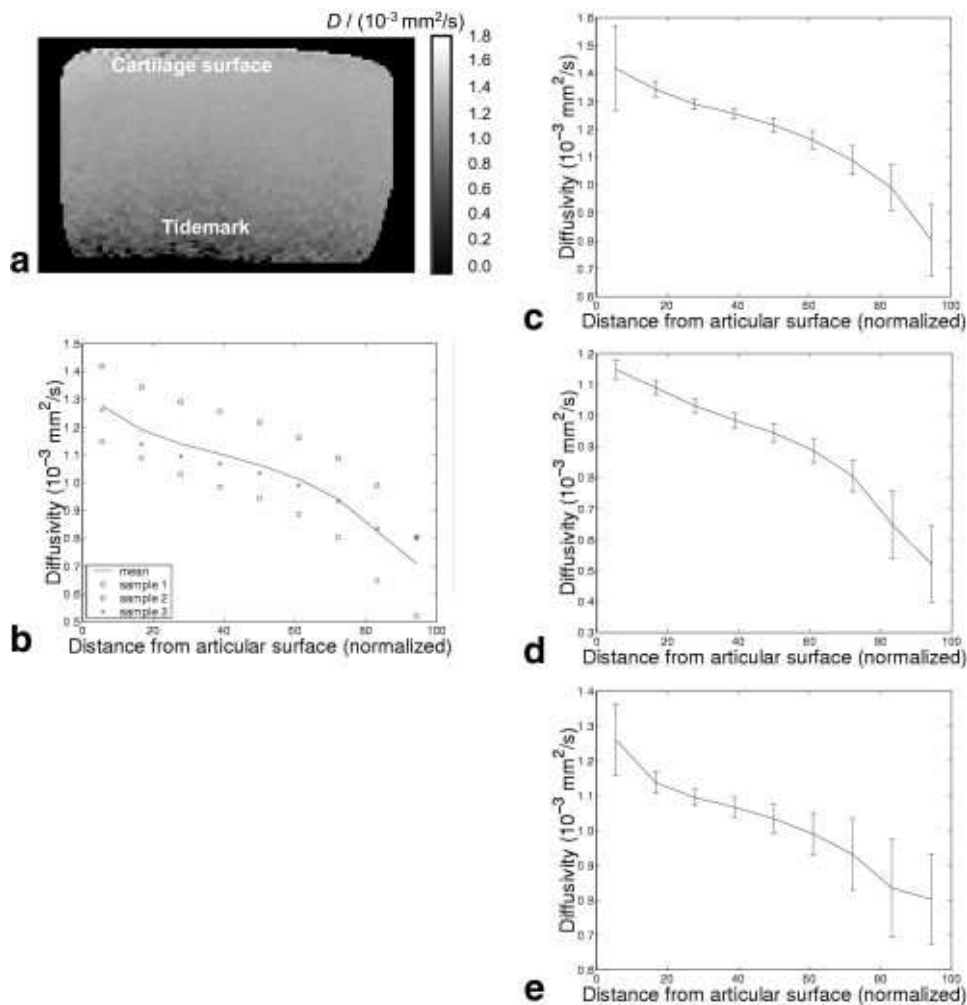


Figure 4.5: Mean diffusivity of human patellar articular cartilage. The mean diffusivity shows maximum values at the cartilage surface, and decreases closer to the cartilage-bone interface. In contrast to the high variability in the radial direction, diffusivity appears fairly homogenous parallel to the surface. **a:** Grayscale parameter map of mean diffusivity. **b:** Mean diffusivity in the cartilage as a function of the normalized distance from the articular surface (values of the separate samples (dots) and averaged values (drawn line)). The diffusivity values vary between  $1.15$  and  $1.45 \times 10^{-3} \text{ mm}^2/\text{s}$  at the cartilage surface, and between  $0.52$  and  $0.68 \times 10^{-3} \text{ mm}^2/\text{s}$  at the cartilage-bone interface. The relative variation of diffusivity from the cartilage surface to the bone is up to 50%. The highest changes in diffusivity appear to occur in the uppermost portions and the lower 60% of the cartilage. **c-e:**

Diffusivity plot (mean and SD) of samples 1-3 calculated from rectangular ROIs each covering about 10% of the total cartilage height.

FA (Figure 4.6) varied between  $0.05 \pm 0.02$  at a depth of approximately 20 to 40% of the total height of the cartilage, and  $0.28 \pm 0.09$  close to the cartilage-bone-interface. Immediately underneath the cartilage surface, FA was about  $0.06 \pm 0.03$ . Similar to mean diffusivity, variations of FA occurred primarily along an axis perpendicular to the cartilage surface and not parallel to it.

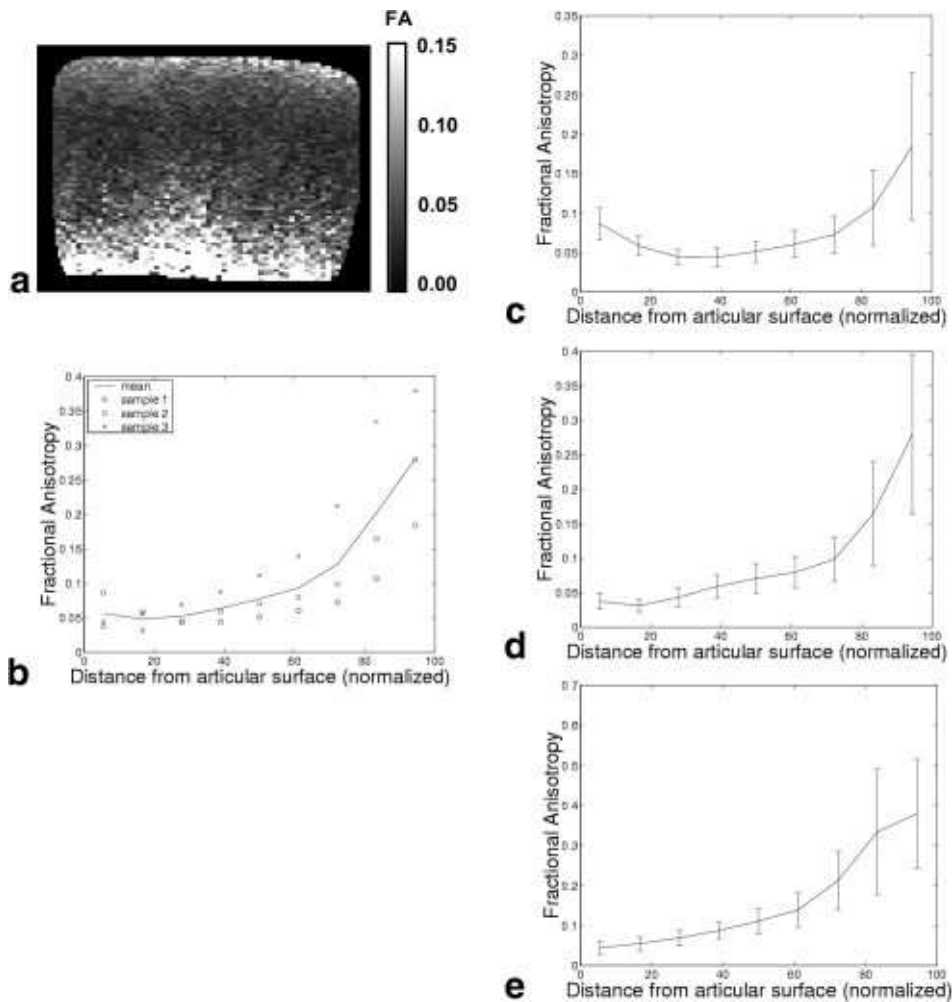


Figure 4.6: FA of human patellar articular cartilage. **a:** Grayscale map of FA. **b:** FA in the cartilage as a function of the normalized distance from the articular surface (values of the separate samples (dots) and averaged values (drawn

---

line)). The FA is comparably small throughout the whole sample, and varies between 0.04 and 0.38. Similarly to the mean diffusivity, FA varies predominantly in the radial direction from the cartilage surface to the bone. The values indicate a high degree of isotropy in the intermediate portion of the samples, a moderate degree of anisotropy immediately underneath the surface, and a steep increase of anisotropy in the lower third of the cartilage toward the cartilage-bone interface. **c-e:** FA plot (mean and SD) of samples 1-3 calculated from bar-shaped ROIs covering about 10% of the total cartilage height.

Like the other evaluated parameters, the eigenvector projection map showed variations mainly with increasing distance from the surface and not parallel to the surface. In this direction the eigenvector projections (Figure 4.7) showed a strong zonal distribution of the predominant alignment of the eigenvectors. We were able to distinguish two layers with a distinctly predominant eigenvector orientation alternating with two comparably thin layers showing isotropic eigenvector alignment. In the upper portions of the cartilage, the eigenvector projections lay predominantly in a plane parallel to the cartilage's surface. In our samples, this region had a thickness of up to 30% of the entire cartilage's thickness. In the lower 50 – 70% of the cartilage, the eigenvector projections were oriented mainly radially. Between these two areas a thin transitional region exhibiting a random orientation of the eigenvectors was detected. This isotropic alignment of the eigenvectors was also observed immediately above the tide mark.

The share of all tangentially oriented (within  $\pm 15^\circ$  around the horizontal plane) first eigenvectors was  $75.3 \pm 7.5$  % in the upper 20% (surface layer) and  $35.3 \pm 9.6$  % close to the tide mark of the cartilage.

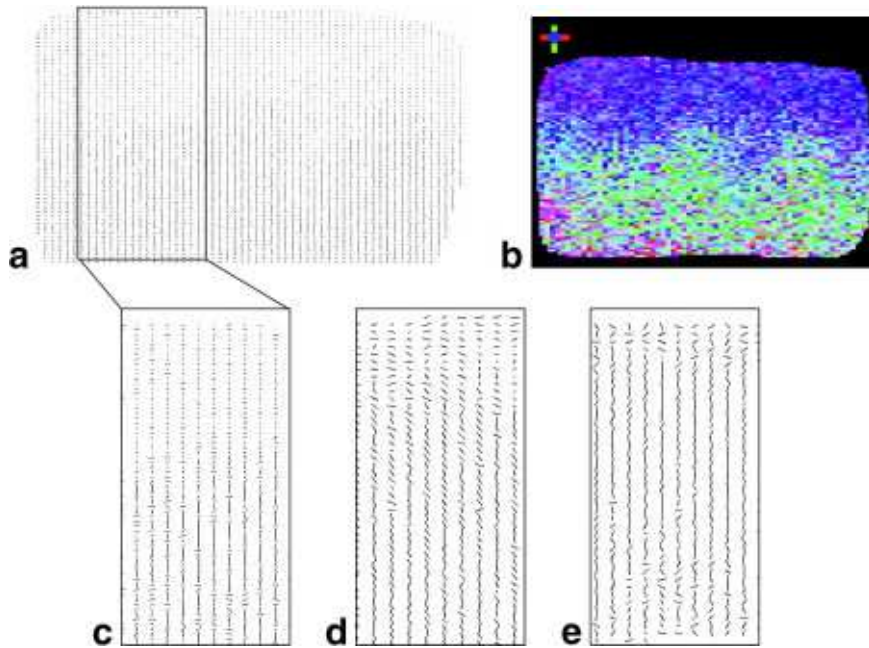


Figure 4.7: Pixelwise projection of the first eigenvector on the plane of the MR image.

**a:** Any line represents the main orientation of bulk water movement within the cartilage matrix, and dots represent diffusion into or out of the imaging plane. **b:** Color map of the first eigenvector orientation. Blue indicates vectors in/out of the imaging plane, and red and green represent vectors parallel and perpendicular to the cartilage surface within the image plane. **c-e:** Magnified ROI of eigenvector plots of samples 1-3. The orientation of the eigenvectors exhibits a zonal pattern. In the upper portion of the cartilage the predominant orientation of the eigenvectors is parallel to the cartilage surface. Similarly, in a small ribbon-like area close to the tide mark a predominantly tangential alignment of the eigenvectors can be seen. In between these two regions, covering an area of about 50-60% of the total height of the cartilage, the predominant orientation of the eigenvectors is perpendicular to the cartilage surface. Variations of the thickness of the respective layers in the three samples from three different individuals are likely to reflect biological interindividual heterogeneity of the cartilage microstructure (Clarke 1971; Glaser 2002; Egli 1988).

SNR averages on all three measurements (Figure 4.8a) showed a maximum in the transitional zone, a low decrease in the tangential zone and a strong decrease close to the cartilage-bone interface. SNR was higher than 5 in all cartilage areas.

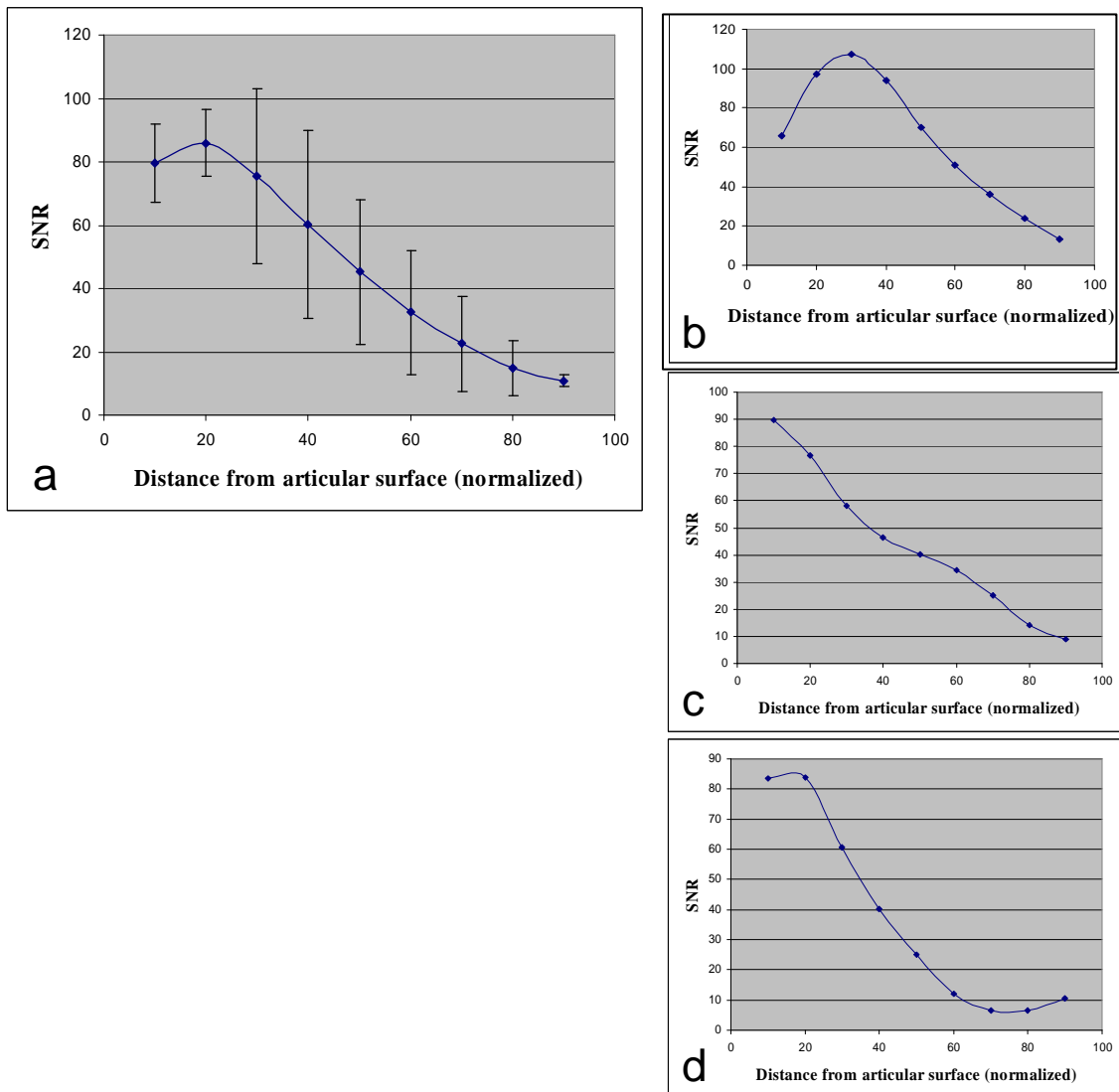


Figure 4.8: SNR profiles in the samples. 9 ROIs in the direction perpendicular to the cartilage surface were considered. **a:** the values of SNR were averaged on all three samples. SNR had a maximum of 86 at a distance from the surface of circa 20% of the total thickness. Direct at the surface was the SNR about

---

7% lower than at the maximum and the averaged value of SNR decreased to 11 at the cartilage-bone interface. **b-d**: SNR plot of samples 1-3.

## 4.4 Discussion and conclusions

In this study we assessed the applicability of DTI for analyzing articular cartilage, and investigated whether DTI can demonstrate regional structural properties of the matrix of articular cartilage.

The matrix of hyaline articular cartilage constitutes a highly structured tissue composed of a network of collagenous fibers in which a proteoglycan-water gel is entrapped. Only the reciprocal stabilization of both constituents achieves the amazing long-term compressive and tensile stiffness of the cartilage matrix as a whole (Buckwalter 1997; Glaser 2002; Maroudas 1976). It is commonly agreed upon that the main structure-giving element of the cartilage matrix are the collagenous fibers. Their predominant alignment relative to the cartilage surface as observed by scanning electron microscopy (SEM) is used to describe the zonal architecture of cartilage (Clarke 1971). The most superficial zone, the tangential zone, with a high content of collagenous fibers which are aligned predominantly parallel to the surface is followed by the transitional zone with an isotropic alignment of collagenous fibers and finally by the radial zone with fiber orientation predominantly perpendicular to the surface (Buckwalter 1997; Glaser 2002). Loss of integrity within this fiber network is regarded to be the hallmark of irreversible damage to cartilage, leading to further deterioration and finally cartilage loss in advanced OA.

As expected, all of the assessed DTI parameters showed a high variation from the cartilage surface towards the cartilage-bone interface, in contrast to almost no detectable variation parallel to the cartilage surface.

The high-field MR system allows achieving an in-plane resolution of  $39 \times 78 \mu\text{m}^2$ , sufficient to investigate the structure of the articular cartilage as suggested from the previous literature (Clarke 1971; Glaser 2002; Egli 1988). The lower variations of the

---

values of ADC and FA in the direction parallel to the cartilage surface in comparison to the variations of ADC and FA in the direction perpendicular to the cartilage surface, validate the setting of an asymmetric in-plane resolution.

Both the range of the values for the mean diffusivity ( $1.45 - 0.52 \times 10^{-3} \text{ mm}^2/\text{s}$ ) and their decrease from cartilage surface to bone observed here are in the same order of magnitude as data reported by Mlynarik et al. (Mlynarik 2003) and Xia et al. (Xia 1995). These authors measured ADC values using unidirectional diffusion sensitizing gradients in human femoral condyle (Mlynarik 2003) and canine humeral head (Xia 1995) cartilage, which varied between  $0.75 \times 10^{-3} \text{ mm}^2/\text{s}$  in the radial zone and  $1.20 \times 10^{-3} \text{ mm}^2/\text{s}$  near the cartilage surface.

The absolute values of FA were relatively small in the cartilage samples, especially in the upper 60% of the cartilage. However, the relative changes in FA between adjacent regions in the cartilage were quite high (Figure 4.6) indicating a zonal variation in the samples. They amounted up to 60% when the most superficial layer (uppermost 10% height) was compared with an intermediate layer (30 – 50% depth) and even up to 400% between this intermediate layer and the deepest 20% of cartilage.

These findings appear consistent with the assumption that the diffusional properties of cartilage are principally determined by two components: 1) a rather homogeneous “ground substance” (probably the proteoglycan-water gel) that gives a baseline diffusivity, and 2) a highly anisotropic structure (the collagenous fiber network) that overlays the baseline and characterizes separate layers. The decrease of diffusivity from surface to bone (Figure 4.5) may be explained by the distribution of proteoglycan concentration in cartilage. It follows a slightly asymmetric bell shape (O’Connor P 1988) with low concentration near the surface, increases to a maximum concentration in a depth of 50 – 90 %, and decreases again when it approaches the tide mark. It has been assumed that proteoglycans may constitute obstacles to and restrict the free

---

mobility of water protons (Xia 1995; Mlynarik 2003). Thus, regions of high proteoglycan concentration may well show a comparably low mean diffusivity.

Similar data on anisotropy throughout the depth of cartilage have been reported 2003 by Nissi et al. (Nissi 2003) and 2001 by Nieminen et al. (Nieminen 2001) using T2-relaxation time mapping correlated with optically determined birefringence of histologically prepared samples. In bovine articular cartilage, they showed comparably long T2-relaxation times at approximately a depth of 20% down from the surface, and a second small relative peak of T2-relaxation time at a depth of about 90% from the surface, close to the tide mark.

Still neither FA nor T2 mapping gives (by definition) directional information. This is provided by the eigenvector projections (Figure 4.7). They show a clear distinction of diffusional properties between upper and lower zones of the cartilage, with a small zone of transition between them. There is a distinct predominance of tangentially oriented eigenvectors in the upper zone, and a clear predominance of radially oriented eigenvectors in the lower zone of cartilage. Wentorf et al. (Wentorf 2003) performed experiments with human femoral and bovine patellar cartilage where two diffusion sensitizing gradients were applied parallel and perpendicular to the cartilage surface. Their results also showed larger parallel diffusion coefficient close the cartilage surface, and a higher perpendicularly oriented diffusion coefficient deeper in the cartilage.

Our findings correlate well with the results of SEM analysis of the collagenous fiber network of cartilage (Clarke 1971; Glaser 2002; Broom 1986). This strongly suggests that DTI eigenvector alignment reflects the predominant alignment of the collagenous fiber network in articular cartilage. The clear distinction between tangential (upper zone) and radial (lower zone) alignment is in agreement with previous findings regarding the collagenous fiber architecture of cartilage in skeletally mature individuals (Clark 1997).

The eigenvector map is in good agreement with the FA values. This is obvious for the lower third of the cartilage where the FA is highest, and for the intermediate portions of the cartilage samples, where minimal FA appears to correspond to an

---

isotropic collagenous fiber architecture. The small increase of FA underneath the surface can be explained by the 3D characteristics of collagenous fiber anisotropy: there is some anisotropy related to an axis perpendicular to the surface, but within the tangential plane a rather random distribution of diffusivity/fibers occurs. It is known that in some joint surfaces that are prone to unidirectional movement (e.g. femoral condyles), the alignment of the collagenous fibers within the tangential zone of the cartilage follows the trajectories of the main tensile stresses (Pauwels 1960).

The small number of samples imaged and the lack of direct histologic or electron microscopic correlation are limitations of this study. However, such issues were beyond the scope of this preliminary work on DTI of articular cartilage, which was confined to a qualitative and descriptive comparison of MRI results with literature data on the ultrastructure of cartilage. In this study, a comparably small diffusion time  $\Delta$  was used, which allowed only for a relatively short diffusion distance (approximately 3 – 4  $\mu\text{m}$ ) to be experienced by the water protons. According to previous findings by Frank et al. (Frank 1999), this may have reduced the sensitivity of the technique to detect macromolecular influence on the direction of diffusion, and may thus have led to underestimation of spatial anisotropy.

In conclusion, our results indicate the feasibility and applicability of DTI experiments for structural analysis of hyaline articular cartilage in high-field-strength MRI. The mean diffusivity, FA, and the eigenvector projection map showed characteristic variations throughout the depth of cartilage. Eigenvectors appear to be the most promising parameters to characterizing the zonal architecture of cartilage, and reflected a tangential zone and a radial zone with a small zone of transition. These results are in good agreement with the current literature about hyaline articular cartilage architecture as defined by the collagenous fibers. They suggest that DTI eigenvector analysis is related to the alignment of the collagenous fibers in cartilage, which is relevant to the detection of early cartilage damage in OA.

---

# **5 DTI of cartilage at 17.6 Tesla: feasibility and limitations**

## **5.1 Introduction**

Since the signal-to-noise ratio in MRI increases with the magnetic field strength, there is a continuous trend towards applying higher fields to improve spatial resolution (Behr VC 2004). Thus, further MR measurements of the diffusion properties of cartilage were performed at 17.6 T on a Bruker Avance 750 MHz wide-bore vertical NMR system (Bruker Biospin GmbH, Rheinstetten, Germany). This field strength is 360 000 times stronger than the earth's magnetic field. With its large bore size of 89 mm, it allows imaging and spectroscopy of samples ranging in size from rats and mice down to single cells.

The work described in this chapter includes the analysis of the characteristics of the instrument to understand limits and feasibility of DTI of articular cartilage with a 17.6-T scanner and the optimization of the measurement protocol.

## **5.2 Instrument**

The basic hardware components of all MRI systems are the magnet, producing a stable and very intense magnetic field, the gradient coils, creating a variable field to encode spatial positioning, and RF coils which are used to transmit energy and receive the MR signal. A computer controls the MR scanning operation and processes the information (Haacke 1999).

---

### 5.2.1 Main magnet

The main magnet (Figure 5.1) produces the time-constant and homogeneous magnetic field  $B_0$ . This field must satisfy high requirements of stability and homogeneity. The higher the field strength, the higher will be the SNR. Drawbacks of high field strength are the prolongation of the relaxation time T1 and consequently the longer acquisition time, stronger susceptibility discontinuities and heavier chemical-shift artifacts and still higher motion sensitivity (Haacke 1999).

Because of fabrication tolerances and the influence of the investigated sample, spatial inhomogeneities occur in the  $B_0$  magnetic field. The shim system creates an additional small magnetic field to correct these inhomogeneities.



Figure 5.1: A 17.6 T magnet (Bruker Biospin GmbH, Rheinstetten, Germany) was used for the MRI experiment. Its main magnetic field was oriented perpendicular to the floor (vertical).

---

### 5.2.2 Gradient system

The gradient coils produce linear magnetic fields that are superimposed on the main magnetic field ( $B_0$ ) and provide slice selection and position encoding within the slice. The efficiency of the gradient system determines the quality of the acquisition: proper design of the size and configuration of the coils is realized to produce a controlled and uniform gradient.

For our measurements, a gradient system Bruker Micro 2.5 with maximal field strength 1 T/m was used (Figure 5.2).

The Micro 2.5 probe has been developed for micro-imaging of small objects (max. diameter 30 mm) in wide bore magnets (89 mm internal diameter). The probe is assembled from its separate modular components: gradient system, probe body (with variable temperature fittings), and exchangeable RF-inserts.



Figure 5.2: Micro 2.5 gradient system (top), probe body (bottom) and exchangeable resonator (middle).

---

### 5.2.3 RF coil

When the sample resides in the MR system, it acts as a resonant circuit for each decoupled nucleus (Haacke 1999). Each of these circuits has a resonant frequency at which it is most sensitive. The RF system in a magnetic resonance imaging apparatus has the function to produce the RF pulse to excite resonantly the nuclei, to receive the signal from the precessing nuclei and to prepare the signal for further processing. This system is composed of dedicated coils. The frequency of the RF coils is defined by the Larmor relationship. Large coils have large measurement fields, but low signal intensity and vice versa. The closer the coil to the object, the stronger is the signal; and the smaller the coil volume, the higher is the SNR.

Tuning is the process of adjusting the transmitter and receiver circuit so that it provides optimal signal performance at the Larmor frequency. A properly tuned system will produce images with a higher SNR, and therefore improved diagnostic versatility.

Matching is the process of adjusting the impedance of the resonant circuit until it corresponds with the impedance of the transmission line connected to it. Correct matching maximizes the energy transmitted to the coil. The purpose of this operation is to increase the SNR.

The adjustments of tuning and matching must be repeated for every sample.

For our experiments, we used a birdcage quadrature resonator (resonant frequency 750 MHz, Larmor frequency of  $^1\text{H}$  at 17.6 T), with inner diameter of 20 mm (Bruker, Rheinstetten, Germany). The bird cage coil design provides the best field homogeneity of all RF imaging coils.

To verify the quality of our measurements, we first analyzed every single repetition of a T2-weighted measurement (Figure 5.3). We performed the measurement with 32 repetitions and calculated in an arbitrary ROI the signal intensity for every repetition. Thereby, we found that the signal intensity had fluctuations of up to 100% between different repetitions with correspondingly high SNR fluctuations (Figure 5.3).

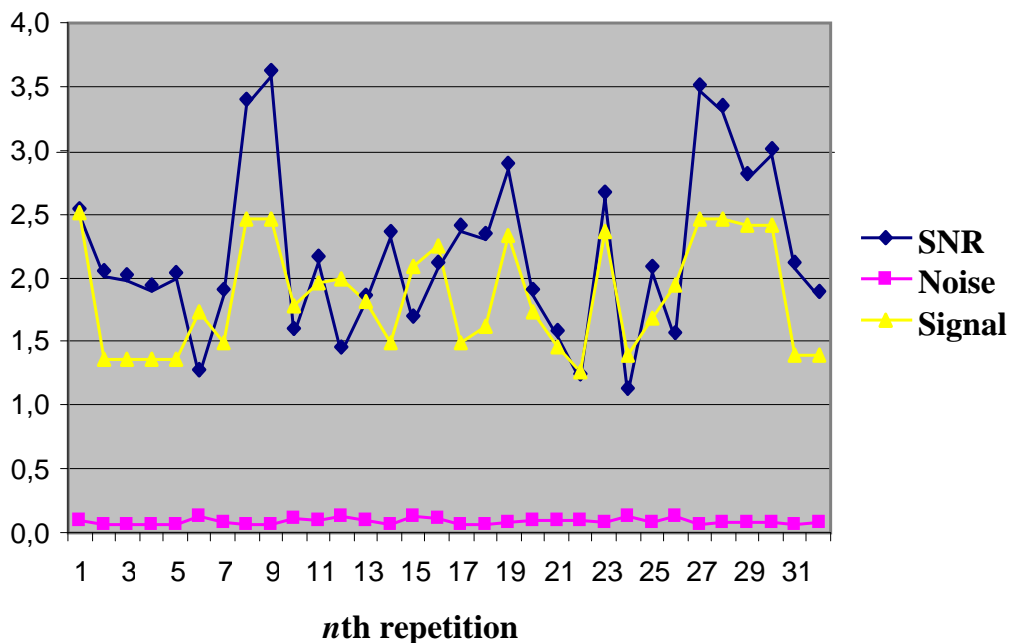


Figure 5.3: The SNR was estimated for every repetition in an arbitrary ROI. Strong fluctuations between repetitions indicated an error in the acquisition.

We could identify that these oscillations were caused by a mechanical instability of the resonator. Strong mechanical vibrations from the gradient system induced in the resonator a change of tune/match setting and, as a result, fluctuations of the signal intensity were determined. After these first experiments, the resonator was repaired and for all successive experiments, the quality of every repetition was tested.

### 5.3 Optimization of the DTI protocol

To avoid the problems corresponding to susceptibility effects, which are known to be particularly severe at 17.6 T, a diffusion-weighted spin-echo sequence (Basser 1994; Bernstein 2004) was employed. Because of the short relaxation time of the cartilage, the

---

echo time TE should be as short as possible. For our experiment, TE was 16 ms, which is the minimal achievable TE with the available gradient strength. The repetition time TR was 1000 ms.

The FOV was 16×16 mm<sup>2</sup> and an in-plane asymmetric matrix 256×64 was chosen, because previous results (see chapter 4 and Filidoro 2005) showed that the cartilage structure is approximately homogenous along the (tangential) phase direction compared to the radial direction. This matrix causes a reduction of the acquisition time and an in-plane resolution of 62.5×250 μm<sup>2</sup>, which satisfies the request of a resolution in the radial direction in the scale of 50 μm. The bandwidth was 130 kHz.

The *b*-values were calculated from the pulse sequence including all imaging gradient, resulting in *b*-values of 0.5 s/mm<sup>2</sup> and 550 s/mm<sup>2</sup>. They were the best compromise between sufficient diffusion contrast and adequate SNR.

The diffusion-weighted spin-echo sequence included two diffusion-sensitizing gradient pulses with duration of 3 ms situated around the 180° pulse separated by 8 ms. Diffusion-weighting gradient were applied in 6 isotropically distributed directions:

$$(G_x, G_y, G_z) = \{(1, 0, 0), (0, 1, 0), (0, 0, 1), (\sqrt{2}, \sqrt{2}, 0), (\sqrt{2}, 0, \sqrt{2}), (0, \sqrt{2}, \sqrt{2})\}$$

### 5.3.1 DTI in an isotropic phantom

For an initial analysis of diffusion tensor measurements at the 17.6-T MRI system, DTI measurements of an isotropic liquid phantom are discussed. The phantom consists of a Plexiglas cylinder containing a saline solution (NaCl 0,9% B. Braun). DTI measurements were realized with the diffusion protocol described in the previous subsection. After the measurement, we estimated the effective diffusion tensor  $\mathbf{D}^{\text{water}}$  using the equation (3.15). We wanted to assess whether  $\mathbf{D}^{\text{water}}$  was an isotropic matrix subject to explainable experimental statistical variability. In this case,  $\mathbf{D}^{\text{water}}$  could be represented by a sphere with radius  $\lambda^{\text{water}}$  and should have the form (Basser 1994 b):

$$\mathbf{D}^{\text{water}} = \lambda^{\text{water}} \mathbf{1} \tag{5.1}$$

where  $\mathbf{1}$  denotes the unit matrix

---


$$\mathbf{1} = \begin{pmatrix} 1 & 0 & 0 \\ 0 & 1 & 0 \\ 0 & 0 & 1 \end{pmatrix} \quad (5.2)$$

This condition is necessary and sufficient for isotropy and can also be expressed by the identity equation:

$$D_{xx}^{\text{water}} = D_{yy}^{\text{water}} = D_{zz}^{\text{water}} = \lambda^{\text{water}} \quad (5.3)$$

and

$$D_{xy}^{\text{water}} = D_{xz}^{\text{water}} = D_{yz}^{\text{water}} = 0 \quad (5.4)$$

We calculated the elements of  $\mathbf{D}^{\text{water}}$  in a sufficiently large ROI (containing at least 20 pixels) in the bulk of the saline solution, far from the surface to avoid susceptibility artifacts, and we averaged on all pixels of the ROI. We considered the diagonal elements of the tensor and we found them to be different from each other: the difference between the higher and lower value was 25%.

We also calculated the diffusion coefficient pro diffusion direction as in equation (3.14):

$$D^g = \ln(S_i^g/S_j^g) / (b_j^g - b_i^g) \quad (5.5)$$

for every diffusion direction  $g$ . (Figure 5.4). The necessary isotropy condition is that the diffusion coefficients were the same for every  $g$ . We found a maximal difference between these coefficients of circa 30%.

With both calculations, the obtained differences were considerably higher than the coefficient of variation of 2.5% at 9.4 T (Section 4.3).

To better understand this apparent anisotropy, we considered the equation (3.15). If the calculated  $\mathbf{D}^{\text{water}}$  does not correspond to the physical diffusion tensor, several causes could be responsible for this effect. A first possibility is that the post-processing program is incorrect. However, the validity of several previous experiments confirmed the quality of this program. The reliability of the values for the signal intensity obtained from the processing console of the instrument was verified in previous measurements as well. Another cause could be that time-dependent temperature variations may generate

corresponding variations of the diffusivity. In this regard, a more accurate analysis of the temperature during the experiment is presented in the next section. At last, one had to take possible errors in the b-matrices into account.

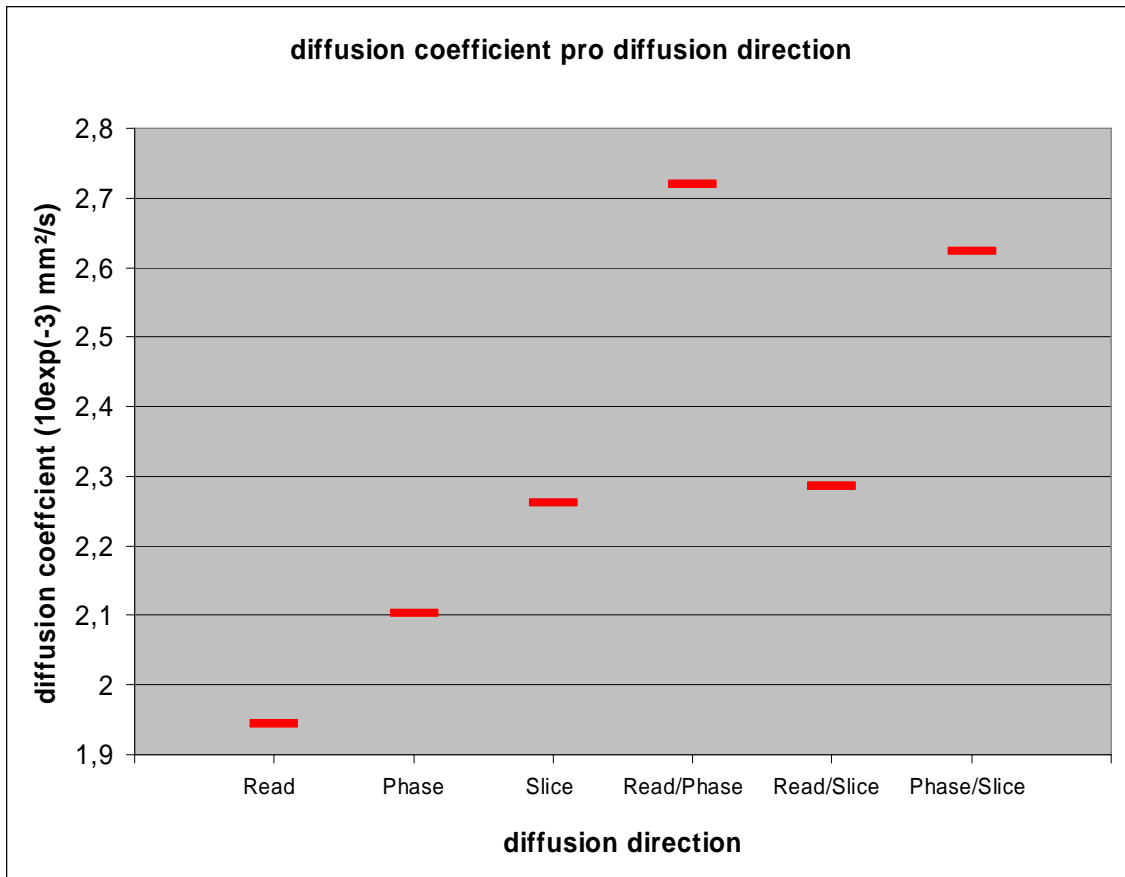


Figure 5.4: The diffusion coefficients in the isotropic saline solution were calculated for each diffusion direction. Differences of up to 30% were registered.

### 5.3.2 Analysis of temperature influences

In the case of variations of the temperature during the measurement, corresponding deviations of the diffusivity are induced. Temperature variations could be caused e.g. by problems of the cooling system of the gradient system or by the released sequence energy. Therefore, we controlled the temperature of the sample during the experiment. At first, during the acquisition, the temperature of the gradient cooling system was kept

between 17 °C and 19 °C (precision 5%). Second we measured the sample temperature directly in the sample box, in brief time intervals, with a fiberoptic thermometer. An example of the temperature behavior is reported in Figure 5.5. The sample was inserted in the RF coil in the center of the gradient system and we found that the sample needed about 1 hour to reach the temperature of the gradient system. Diffusion-weighted imaging did not cause any substantial temperature variations. We paid attention to measure DTI only in the temperature equilibrium.

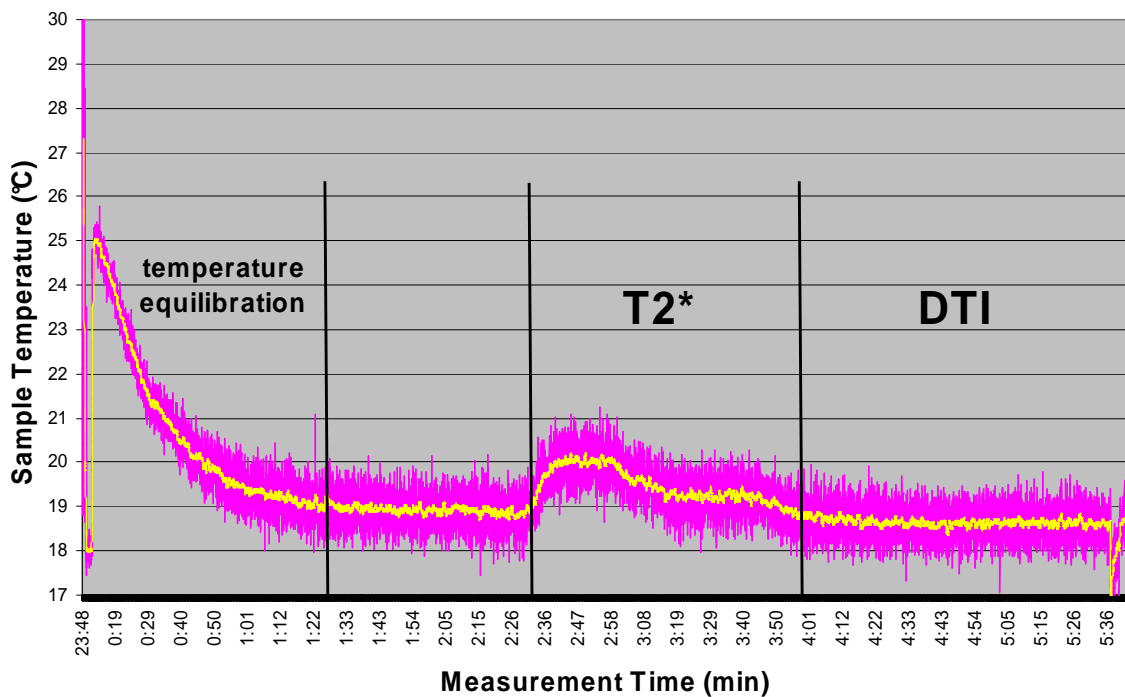


Figure 5.5: The temperature of the sample was measured during the entire experiment. About 1 hour after the start, the sample had the same temperature as the gradient system. Standard diffusion-weighted sequences do not cause a significant increase in the temperature. Pink are the experimental values and yellow the averaged values.

The oscillations of the temperature during the DTI measurement correspond to the precision of 5% of the cooling system and cannot explain the high differences in the diffusivities.

---

### 5.3.3 Analysis of b-matrix

Another possible source of the inaccuracy in the determination of diffusion coefficients could be the effective b-matrix employed in the experiment and the calculated values of the b-matrix. As shown in chapter 3 (equations 3.9 and 3.16), the b-matrix depends on the values of the magnetic gradients. For diffusion-weighted sequences, the magnetic gradients work only at circa 50% of their efficiency and only for circa 3 ms (the gradient ramp-up time). Hence the gradient system was not at its performance limit and substantial non-linearity in the gradient scaling was improbable.

As next step, we verified the calculation of the b-matrix elements. In DTI, we estimated the effective diffusion tensor,  $\mathbf{D}$ , from the measured spin-echo signals, using equation 3.15. By calculating an analytical expression for the b-matrix, we have accounted for all gradient pulses that typically arise, including localization, crusher, and diffusion gradients; all of which are known to affect the echo intensity. Therefore, so-called “cross-terms” have to be considered as well. Considering all imaging and diffusion gradients, each element of the b-matrix can be decomposed into three parts

$$b_{ij} = b_{Dij} + b_{CTij} + b_{IMGij} \quad (5.6)$$

$b_{Dij}$  is the diffusion term and is proportional to the product of the strength of two diffusion gradients. The second term  $b_{CTij}$ , also called the “cross term”, depends on the product of a diffusion gradient pulse and one imaging gradient. The third term  $b_{IMGij}$  is generated by the imaging gradients alone; it usually has the smallest contribution to  $b_{ij}$  and can be ignored in the calculation of  $b_{ij}$ . An additional assumption is that the influence of the phase-encoding gradient on the b-matrix elements can be neglected. This is a reasonable approximation because the main signal intensity is related to the center of k-space where the amplitude of this gradient is zero or close to zero (Güllmar 2008).

Calculating the above b-matrices with equation 3.16, we obtained diagonal elements of the diffusion tensor better matching the expected equality of equation 5.3, such that these b-matrices were used for the following.

---

### 5.3.4 Eddy-current effects

As an additional possible cause for the diffusion tensor anisotropy in the water phantom, we investigated the influence of gradients induced from eddy currents.

Large, rapidly switched magnetic field gradients during the diffusion sequence produce electric fields that result from changing magnetic flux (Faraday's law). These electric fields induce eddy currents in the MR system. In turn, the eddy currents produce additional unwanted, rapidly and slowly decaying magnetic fields (Basser 2002; Bernstein 2004). Depending on their spatial dependence, eddy currents will be classified into  $B_0$  eddy currents which are spatially constant over the image volume, and linear eddy currents, which have a linear spatial dependency similar to imaging gradient fields (Bernstein 2004). Linear eddy currents results in two undesirable effects: first, the effective magnetic gradient at the sample differs from the set magnetic gradient, resulting in a difference between the effective and calculated b-matrix; second, the eddy current produces a slowly decaying field during readout of the image causing geometrical distortions of the diffusion-weighted image. (Basser 2002). In our measurements, the linear eddy currents were predominant compared to the  $B_0$  eddy currents. The resulting preemphasized waveform for the linear component looks like a high-pass-filtered version of the original gradient waveform (Bernstein 2004). The result was that geometrical distortions were corrected. Nevertheless, the eddy current induced an apparent anisotropy in the isotropic phantom. To reduce this effect, correction strategies based on the acquisition of diffusion-weighted data with opposite polarity diffusion gradients were adopted (Bodammer 2004; Neeman 1991).

### 5.3.5 Chemical-shift artifacts

Chemical shift is a variation in the resonance frequency of a nuclear spin due to the chemical environment around the nucleus. In an image, the chemical-shift artifact is a misregistration between the relative positions of two tissues with different chemical shifts. Most common is the misregistration between fat and water (Haacke 1999).

---

In our samples, the water of the cartilage as well as the fat of the bone was present; hence, the relevance of the chemical-shift artifact in the DTI measurement will be investigated.

During the slice selection process, there is a slight offset between the location of the fat and water spins which have been rotated by an RF pulse. During the frequency-encoding gradient, fat and water spins located in the same voxel precess at rates differing by 3.35 ppm. The net effect is that the fat and water located in the same voxel are encoded as being located in different voxels. Even though the phase is different, the fat is not encoded as being in a different phase-encoding-direction voxel (Haacke 1999); instead, the chemical shift artifact will manifest along the frequency-encoding direction (Haacke 1999). Furthermore, the sign of the shift depends on the orientation of the growing frequency-encoding steps, feet first or head first.

To quantify the effect of the chemical-shift artifact, we analyze the position of the fat in the image in comparison with his effective position in the sample. This displacement is  $N_{\text{shift}}$ , the number of shifted pixels along the frequency-encoding direction.  $N_{\text{shift}}$  is given by the ratio of the frequency shift  $\Delta f$  between water and fat and the bandwidth per voxel  $\Delta f_{\text{voxel}}$ :

$$N_{\text{shift}} = \Delta f / \Delta f_{\text{voxel}} \quad (5.7)$$

The frequency shift of fat relative to water, in the human body, is:

$$\Delta f = f_{\text{fat}} - f_{\text{water}} \quad (5.8)$$

and

$$f_{\text{fat}} - f_{\text{water}} = -\sigma \gamma B_0 \quad (5.9)$$

where  $\sigma = 3.35 \cdot 10^{-6}$ ,  $\gamma = 42.577 \cdot 10^6$  Hz/T and  $B_0 = 17.6$  T.  $\Delta f$  was 2510 Hz.

From (Haacke 1999), we know that the bandwidth per voxel is:

$$\Delta f_{\text{voxel}} = \gamma G_{\text{read}} \text{FOV}_{\text{read}} / N_{\text{read}} \quad (5.10)$$

where  $G_{\text{read}}$  is the applied magnetic gradient in read direction,  $\text{FOV}_{\text{read}}$  the FOV in read direction and  $N_{\text{read}}$  the frequency encoding steps. Known that  $G_{\text{read}}$  is  $43 \cdot 10^{-3}$  T/m,

---

FOV<sub>read</sub>  $16 \cdot 10^{-3}$  m and  $N_{\text{read}}$  256. Hence the value of  $\Delta f_{\text{voxel}}$  is 116.3 Hz. Then, for our measurements, we obtain  $N_{\text{shift}} \sim 22$  pixels, which cannot be neglected.

We verified with an experiment the dependence of the fat shift on the bandwidth (Figure 5.6). The experimental curve is in good agreement with the theoretical profile. The bandwidth of 130 kHz selected for the DTI measurements results in a chemical shift that is relatively low in the tested interval but still relevant due to the very high spatial resolution of about 50  $\mu\text{m}$  in readout direction.

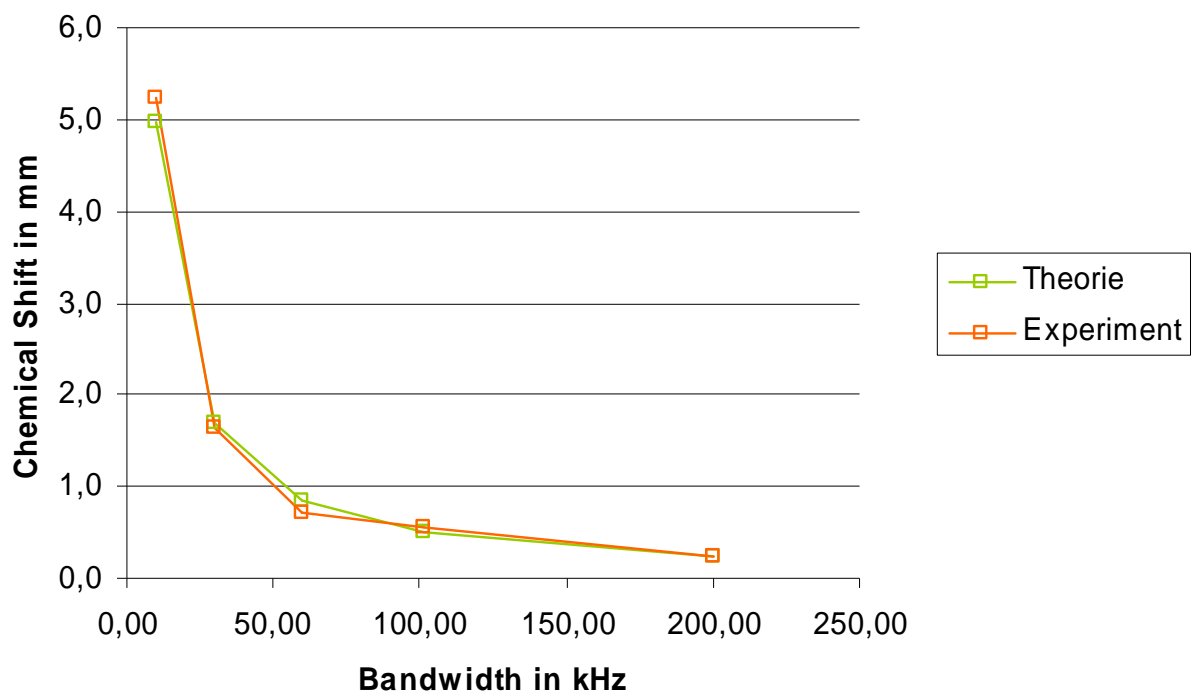


Figure 5.6: The experiment was realized with different bandwidths and the chemical shifts were obtained from the measured values as well as calculated with the theoretical equations (5.7-5.10). Both curves show a similar profile and agree well.

In our experiment, however, the measurement geometry is very helpful (Figure 5.7). In the slice direction the fat shift from bone concerned only the bone region and not the cartilage part of the sample. Additionally, the sample was positioned so that bone, cartilage and water were aligned along the read-out direction. With the setting “Feet

---

First”, the fat signal was shifted away from the bone outside the sample, whereas with “Head First” the fat signal overlapped the cartilage image. For this reason, we realized all experiments with “Feet first” setting and further strategies to avoid chemical-shift effects were not necessary.

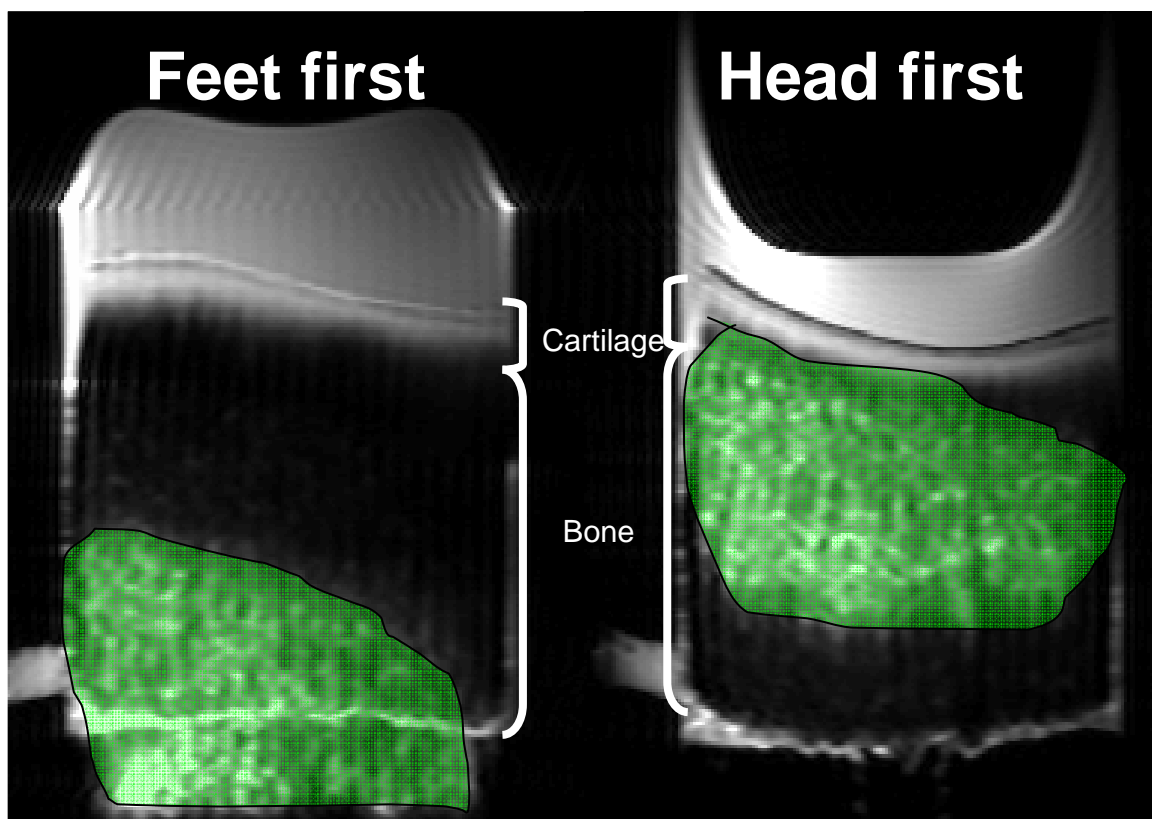


Figure 5.7: Chemical shift of the fat signal relatively to the water signal. The read-out direction is the vertical direction. The green spot represents the fat signal from the bone fat. With the setting “Head First” in the read direction, the fat signal was shifted towards the cartilage; whereas with the setting “Feet First”, the fat signal was shift away from the cartilage. The distortion of the cartilage was caused by the low bandwidth of 20 kHz.

---

## 5.4 Coordinate systems

A significant parameter obtained from DTI is the first eigenvector, which represents the principal direction of diffusion. The projection of the first eigenvector in the image plane is helpful to analyze the microstructure of the cartilage.

To correctly project this eigenvector, it is necessary to analyze the coordinate systems involved in the measurement. The laboratory frame is the reference system in which the MR instrument is located. The gradient coil frame is the frame with coordinates in readout, phase-encoding, and slice-selection (RPS) directions. The image will finally be displayed in the post-processing frame. The transition from the RPS-frame to the post-processing frame has to be correctly described. But the directions of the axis in the RPS-frame are a priori unknown. Therefore, we determined the axis direction in the RPS-frame with a phantom measurement, by considering a phantom with a known pronounced anisotropy, and measuring it with DTI in two different positions (Figure 5.8). Then we chose the representation of the RPS-frame in the post-processing frame so that the known anisotropy is displayed correctly.

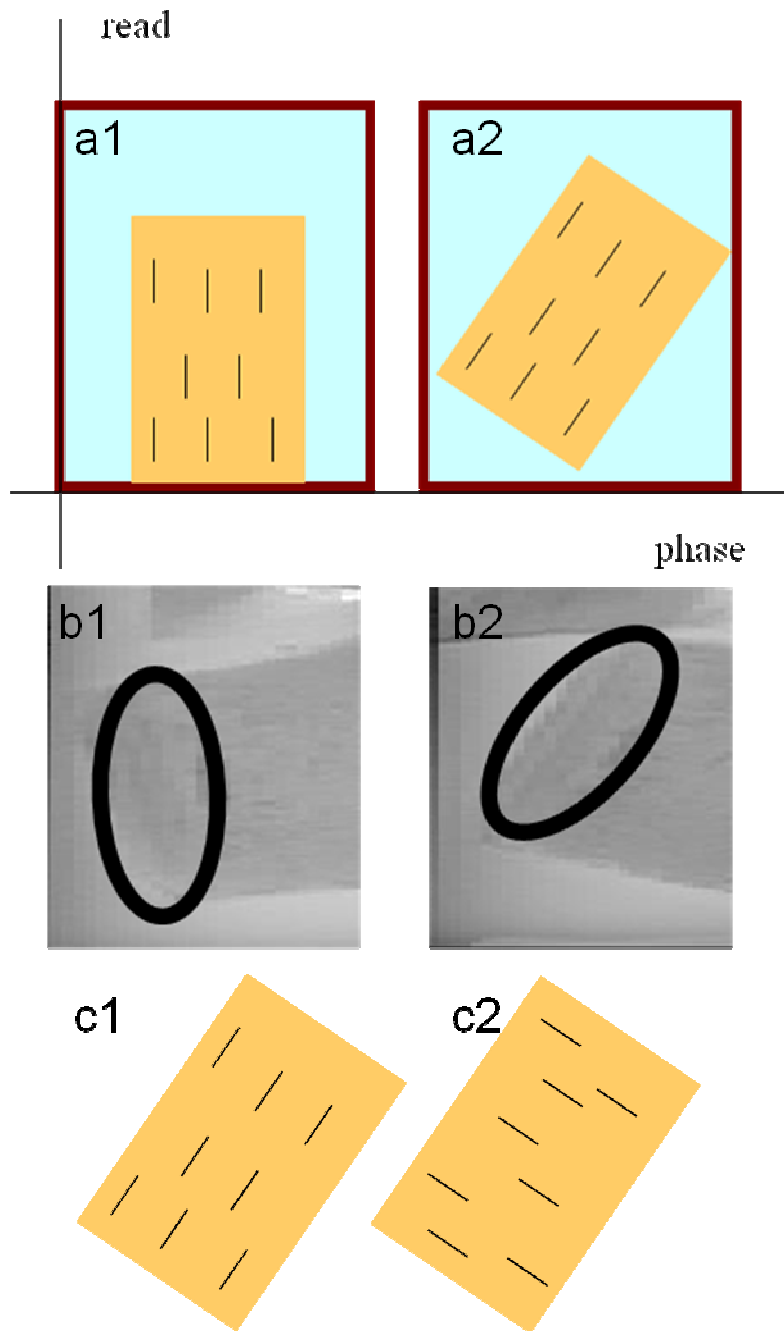


Figure 5.8: The anisotropy of the phantom is known. a) Schematic representation of the anisotropic phantom in two different positions: a1) main anisotropy parallel to the read direction; a2) main anisotropy in the diagonal between read and phase direction; b) Our phantom was a part (encircled) of a carrot with known fiber structure; c) After the measurement, the data were processed.

---

Different orientations of the coordinate system in the post-processing result in images with c1) correct anisotropy or c2) erroneous anisotropy.

## 5.5 FA versus SNR

Image noise in DTI can introduce a significant bias in the estimates for the eigenvalues, which makes isotropic media appear anisotropic, and anisotropic media appear more anisotropic. Therefore, it is important to analyze the dependency of FA on the SNR (Figure 5.9) (Weber DL 2007, Bastin 1998, Pierpaoli and Basser 1996).

The cartilage was divided in three regions of interest with different distances to the surface (Figure 5.9). To obtain different SNRs we averaged different numbers of repetitions (1, 2, 4, 8 and 16). The noise in the regions of interest was determined using difference images of identical acquisitions (Firbank 1999).

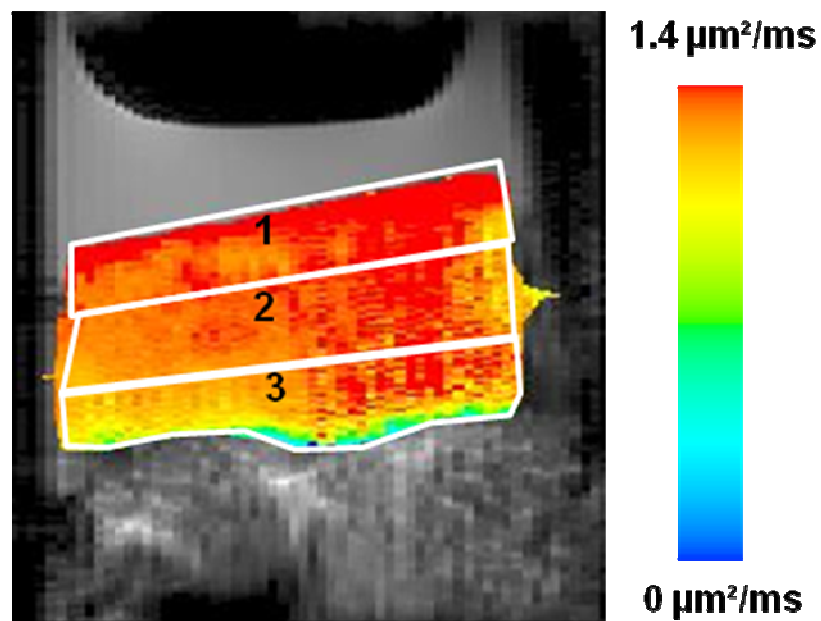


Figure 5.9: ADC in the articular cartilage. The cartilage is divided in 3 areas: 1 = surface, 2 center, 3 = close to bone.

---

In Figure 5.9 an ADC-map of the probe is shown. The SNR dependency of the FA is shown in Figure 5.10. The FA decreases as expected with increasing SNR and reaches approximately constant values for SNRs greater than 70.

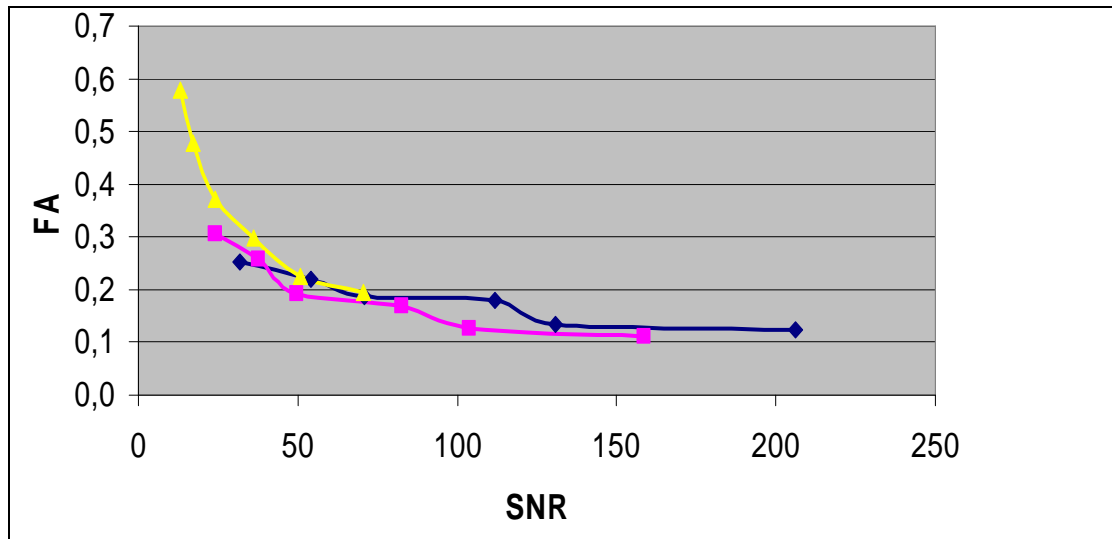


Figure 5.10: The dependency of the fractional anisotropy from the SNR is shown.

Diamonds are area 1, squares are area 2, and triangles are area 3.

An accurate analysis of diffusion tensor data can only be done if it is guaranteed that the SNR is high enough to determine the correct ratio between the eigenvalues of the diffusion tensor. Figure 5.10 shows that this is given in our setup for an SNR of 70 and higher.

## 5.6 Discussion and conclusions

On the one hand, cartilage exhibits short T2 relaxation times (20-60 ms) (Mlynarik 1999, Mosher 2000) and its thickness is limited to (at best) 5-6 mm. On the other hand, it is important to achieve an optimal spatial resolution at sufficient SNR to differentiate the zonal properties of the cartilage. Based on literature data on the thickness of the various cartilage layers (Clarke 1971, Glaser 2002, Egli 1988), a resolution of circa 50  $\mu\text{m}$  providing approximately 100 voxels for the analysis of variations of DTI

---

parameters in the radial direction, seems high enough to reliably monitor regional differences in diffusivity (Filidoro 2005). Such resolution is usually achieved by combining dedicated gradient systems with high magnetic field strength. On account of this, our measurements were realized at 9.4 T and 17.6 T.

With high-field-strength magnets, the problems corresponding to susceptibility effects will become very severe, particularly at 17.6 T. For this reason, a spin-echo sequence, less sensitive to susceptibility effects than echoplanar imaging techniques, is preferred (Basser 1994; Bernstein 2004). However, the spin-echo sequence is highly sensitive to motion. Motion could arise from two sources: patient or sample bulk motion and vibrations of the sample apparatus induced by the strong diffusion-weighting gradient pulses. In our experiments, there was no patient motion and it has been taken care that gradient-induced vibration was avoided through mechanical stiffness of the measurement device. The spin-echo sequence is also characterized by very long data acquisition time, but this point is decisive in the first instance only for clinical applications.

In conclusion, we introduced and optimized a measurement protocol for cartilage DTI at 17.6 T that respected all requirements to achieve the best compromise between good SNR and high in-plane resolution. With this protocol, the diffusion tensor was calculated in an isotropic phantom. The results showed an undesirable apparent anisotropy, which causes were further investigated by a detailed analysis of the influence of temperature, of eddy-current effects, b-matrix calculation, and chemical-shift artifacts. The main factors influencing the precision of the DTI measurements turned out to be the calculation of the b-matrix considering cross-term contributions due to the imaging gradients and the influence of gradient eddy currents, which could be reduced by improved diffusion-gradient encoding schemes. The amount of chemical shift of bone fat was determined and the potentially interfering effect was removed from our cartilage image data by geometrical considerations. Finally, the representations of the diffusion tensor eigenvectors in the laboratory frame, gradient coil frame and post-

---

processing frame and the dependence of the FA on the SNR were analyzed in order to ensure a correct and accurate DTI measurement.

---

# **6 DTI of cartilage at 17.6 T: correlation with histology and scanning electron microscopy**

## **6.1 Introduction**

The results on DTI of the cartilage presented in Chapter 4 showed that the orientation of the first eigenvector likely represents the zonal architecture of the cartilage (Filidoro 2005). Further, a recent study demonstrated that the orientation of the first eigenvector correlates with the orientation of polarization in polarization light microscopy (de Visser08), while mechanical loading of the cartilage leads to reduced ADC, increased FA and reorientation of the first eigenvectors (Filidoro 2004; Raya 2008; Raya 2011; de Visser 2008b). Degradation of the cartilage with trypsin, which selectively removes proteoglycans from cartilage, resulted in increased ADC (Knauss 1999; Meder 2006; Deng 2007) and unchanged FA (Meder 2006; Deng 2007), thus indicating a dependence of ADC on the proteoglycan content and a dependence of FA on the collagen content. A main question, however, remains to be assessed: What is the dependence between the DTI parameters and the constituents of the extracellular matrix, especially the relationship of the first eigenvector and the collagen structure of the cartilage.

After the analysis of the feasibility and the limitations of DTI at the 17.6-T system (cf. chapter 5), DTI measurements with this system were realized. The aim of the work presented in this chapter was to confirm the results of DTI at 9.4 T and to investigate the relationship of the different diffusion tensor imaging parameters with the

---

constituents (proteoglycans and collagen) and the mechanical properties of articular cartilage.

## **6.2 Materials & Methods**

### **6.2.1 Sample preparation**

MRI was performed on human patellar cartilage-on-bone samples. The patellae ( $n = 8$ ,  $(31 \pm 15)$  y) were harvested within 48 h after death and conserved at 5 °C until the imaging session, which was performed between 6 and 72 hours after harvest. Only patellae with macroscopically intact cartilage (white color, integrity of the surface of the articular cartilage and stiff mechanical properties by manual testing), were considered for MRI examination.

From each patella a cylindrical cartilage-on-bone sample of 14 mm diameter was drilled perpendicular to the articular surface from the centre of the medial patellar facet. During drilling, the patella was continuously rinsed with cooled (5 °C) physiological saline. The desired MRI slice was visually selected and marked with an incision in the bony part of the sample which could be seen in MRI. The sample was placed in a cylinder of acrylic glass (plexiglas, 20 mm outer diameter) tightly fitting into the coil to prevent motion artifacts. The inner diameter of the cylinder was equal to the diameter of the sample and had a thread of 1 mm pitch matching with a cylindrical screw for loading experiments. After inserting the sample in the plexiglas cylinder, physiologic saline was added to prevent cartilage dehydration during MRI. The sample was positioned so that its articular surface was oriented perpendicular to the external magnetic field.

### **6.2.2 MRI**

#### **Imaging protocol**

All samples were imaged at a 17.6-T scanner (Bruker, Rheinstetten, Germany), with a

---

maximum gradient strength of 1 T/m and using a 20 mm birdcage coil (Bruker, Rheinstetten, Germany). The imaging protocol included a high resolution FLASH sequence (TR/TE = 60/3.1 ms, FOV = 16×16 mm<sup>2</sup>, matrix = 512×512, in-plane resolution = 31×31 μm<sup>2</sup>, slice thickness = 1 mm, bandwidth = 101 kHz, averages = 8, acquisition time = 4:06 min), and a diffusion-weighted spin-echo sequence (described in section 5.3). During the acquisition, the temperature of the gradient cooling system was kept between 17 °C and 19 °C.

Three of the samples were measured under mechanical loading conditions in addition to imaging without loading. Therefore, immediately after MRI, the samples were taken out of the scanner and indented using a 5 mm non-porous cylindrical indenter of acrylic glass (plexiglas) with slightly rounded borders to avoid susceptibility artifacts (Figure 6.1). A strain of 20% of the cartilage thickness as measured on the high resolution FLASH image was applied. The angle, by which the screw must be rotated to get the desired strain, was calculated using the pitch of the thread. The strain was applied in three steps with a rest-time of 30 min after each stepwise indentation to ensure that the cartilage reached equilibrium. The sample was introduced in the scanner and imaged at the same slice position as in the measurement without loading.

One of the three samples measured under loading conditions was additionally measured after 1 hour of relaxation from the loading experiment to demonstrate the process of recovery.

After MRI, the samples were extracted from the cylinder and conserved in physiologic saline at 4 °C for analysis/preparation.

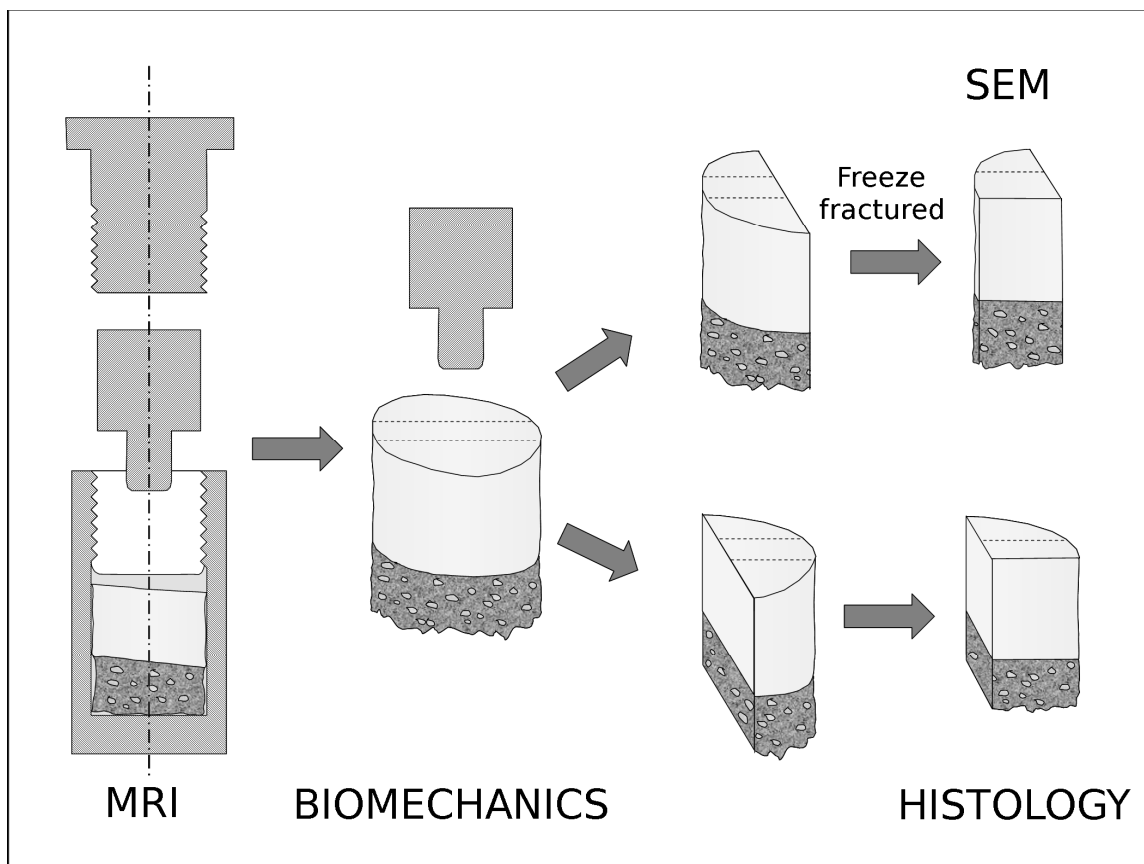


Figure 6.1: Schema of the experiment design. First, MRI was performed with and without mechanical loading. Second, the sample was tested for biomechanics: the load was applied from the indenter on the region of the MRI slice. Then the sample was cut perpendicular to the MRI slice and further analyzed in SEM and histology.

### Imaging processing

DTI data were processed using self-written programs in Matlab (MathWorks Inc., Natick, Massachusetts, USA). For each voxel the three eigenvalues ( $\lambda_1$ ,  $\lambda_2$  and  $\lambda_3$ ) and their corresponding eigenvectors were calculated. ADC and FA were calculated for each voxel from the eigenvalues according to the formulas in chapter 3.

In order to perform interindividual comparisons of the distribution of ADC and FA values across the cartilage, the complete cartilage was automatically segmented in the ADC and FA maps and stretched to fill a rectangle. The height of the rectangle was

---

normalized from zero at the bone-cartilage interface to one at the articular surface to simplify interindividual comparison. Average ADC and FA profiles of each sample were obtained. These profiles were used to test significant differences between samples with and without loading (two-sample t-test  $P < 0.01$ ).

Automatic segmentation of the cartilage was performed using the ADC and SNR maps. SNR maps were obtained as the quotient of the signal intensity at  $b = 0.5 \text{ s/mm}^2$  and the standard deviation of noise,  $\sigma$ , automatically calculated by fitting the first peak in the histogram of the signal intensity of the DTI measurements to a Rician distribution. The segmentation algorithm automatically identified the center of the cartilage in the image, and placed an initial ROI with a width of 16 voxel symmetrically around the center. With a growing algorithm the initial ROI was extended to include the complete cartilage height. At the articular surface, the growing algorithm stopped when the ADC was larger than ADC in water minus five times the standard deviation of the ADC in water (both calculated automatically from the histogram of ADC), or when the SNR was lower than 10 (in the case of indentation). At the bone-cartilage interface the algorithm stopped if the SNR dropped below 5 or if the ADC became lower than  $0.1 \times 10^{-3} \text{ mm}^2/\text{s}$  (i.e., the difference in signal intensity between the images with  $b = 0.5 \text{ s/mm}^2$  and  $b = 550 \text{ s/mm}^2$  were lower than two times the standard deviation of noise).

The projection of the first eigenvector (i.e., the eigenvector corresponding to the largest eigenvalue) in the imaging plane together with the information of the FA maps were used to calculate the height of the different cartilage zones (tangential, transitional and radial). The radial zone was characterized by a high anisotropy and a predominant orientation of the first eigenvector along the vertical direction (Figure 6.3). In the transitional zone, the eigenvectors showed no preferred orientation with the FA taking very low values. In the tangential zone, the FA slightly increased and eigenvectors clearly orientate in the direction of the articular surface. With this criterion the height of the different zones was calculated for each sample at five different positions along the

---

bone-cartilage interface. After normalization to the cartilage thickness in each position, the relative heights of all zones in a sample were averaged.

### 6.2.3 Biomechanical testing

Samples underwent biomechanical testing within 12 hours after MRI. The mechanical properties of the cartilage samples were assessed with a high-precision material testing machine (Zwick/Roell Z2.5, Ulm, Germany), with a spatial and force resolution of 0.1  $\mu\text{m}$  and 0.001 N, respectively. Samples were indented under non-confined conditions using a non-porous indenter with the same diameter (5 mm) and shape as the indenter used in the MR experiments (Figure 6.2).

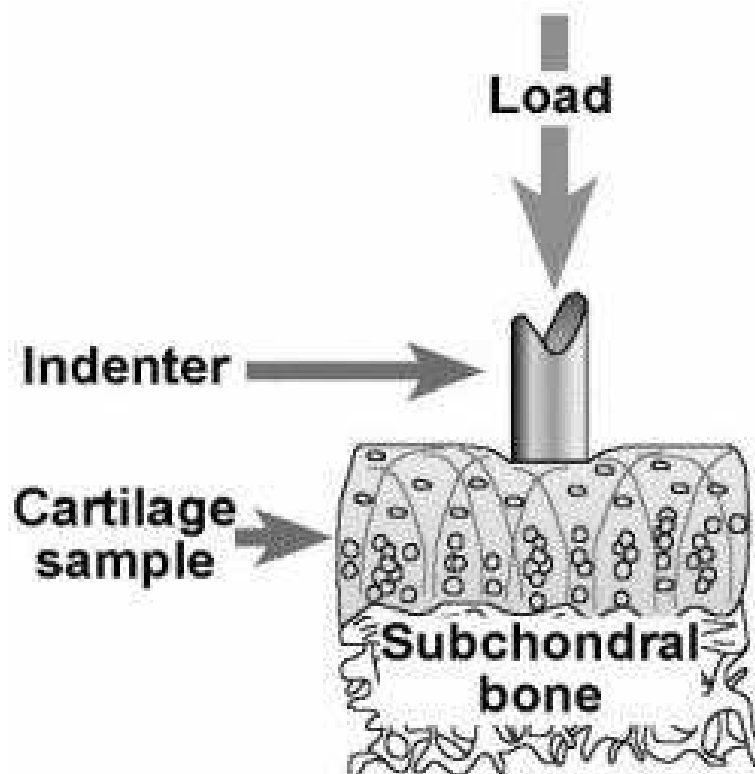


Figure 6.2: The indentation experiment simulates better than other mechanical tests the anatomical loading on the cartilage in the body: the load is local, the cartilage is still anchored to the bone and the cartilage fluid can move freely in the sample.

---

With the indentation test, physiological conditions in the loaded region were maintained: fluid distribution and collagen fibers structure were the same as in intact cartilage (Hayes 1972, Korhonen 2002). During the biomechanical testing, samples were continuously rinsed with physiologic saline using a perfusion pump to avoid drying of the sample.

After equilibration under an offset force of 0.5 N, four stepwise stress-relaxation tests each one of 5% of the uncompressed cartilage thickness were performed. In each step, indentation was performed at a constant velocity of 1  $\mu\text{m/s}$ . The time duration of each stress-relaxation test was 20 min to ensure complete relaxation of the cartilage. This setup was identical to the procedure used for loading experiments in MRI.

The Young's modulus was calculated from the non-confined strain-stress experiments using the model for a single phase, elastic material of Hayes et al. (Hayes 1972),

$$E_s = (1 - \nu_s^2) \frac{\pi a E}{2 \kappa h} \quad (6.1)$$

where  $E_s$  is Young's modulus,  $\nu_s$  is Poisson's ratio (the theoretical value of Korhonen et al. where used),  $a$  is the radius of the indenter,  $\kappa$  is a geometric factor, which is tabulated for  $\nu_s$  and  $a/h$  in (Hayes 1972), and  $E$  is the slope of the equilibrium stress-strain curve calculated as follows,

$$E = \frac{h}{\pi a^2} \frac{\Delta f}{\Delta h} \quad (6.2)$$

where  $h$  is the height of the cartilage,  $\Delta f / \Delta h$  is slope of the linear fit to the force  $\Delta f$  at equilibrium with the indentation  $\Delta h$ . Young's modulus of the samples was correlated with the bulk ADC and FA to demonstrate a possible relationship of the diffusion and biomechanical properties.

---

After biomechanical testing, all samples were put in a 4% paraformaldehyd solution in phosphate buffered saline (pH 7.2) at 4 °C. The samples were then split in two equal parts (Figure 6.1) perpendicular to the MR slice as indicated by the incision in the subchondral bone. One half of the divided sample underwent histology and the other half SEM.

### **6.2.3 Scanning electron microscopy (SEM)**

Sample parts undergoing SEM were incubated for 24 h in 2 M CaCl<sub>2</sub> solution at room temperature (20±2)°C for proteoglycan extraction. Afterwards, samples were fixed in a phosphate buffered 4% formaldehyde solution for another 24 h and dehydrated by immersion in an ascending acetone series (30 min at concentrations of 50%, 70%, 80%, 90%, 96%, 100% and twice for 1 h at 100%) for CO<sub>2</sub> critical-point drying (Critical Point Dryer CDP 030; Bal-Tec, Balzers, Principality of Liechtenstein). Samples were then frozen by 30 s immersion in liquid N<sub>2</sub> and freeze-fractured in two parts along the MRI imaging plane. One of the two fractured cartilage pieces was selected to undergo SEM and was 30 nm gold-coated (2.4 kV and 20 mA) using a sputter coater unit (Polaron SEM E5000; Polaron Equipment, Watford, England).

The gold-coated samples were analyzed with a scanning electron microscope (JSM-35 CF; Jeol, Tokio, Japan) at a 6000× magnification to resolve the course of the collagen fibers (Glaser 2002). In SEM the height of the different zones of the cartilage (tangential, transitional and radial zones) is measured. From the articular surface to the tide mark, the fiber orientation in the SEM 6000 × FOV was visually classified in steps of 50 μm as predominantly tangential, predominantly radial or with no predominant orientation. The boundary between two zones (tangential-transitional or transitional-radial), were calculated as the mean of the position of the nearest SEM 6000 × FOV showing the adequate fiber orientation in each cartilage zone. The height of the cartilage zones was calculated at five different locations across the cartilage. After normalization

---

to the cartilage thickness as measured in SEM, the relative height of the zones calculated at the five positions were averaged.

The heights of the zones calculated with SEM were compared to the zonal heights measured from DTI images. Correlation of the SEM and DTI heights was calculated and significant differences in the median of the heights were assessed with the Wilcoxon signed-rank test.

For documentation and semi-quantitative assessment of relative collagen content, SEM 6000 × FOVs with well defined fiber orientation were photographed for each sample (camera Mamiya 6×7; Mamiya, New York, USA, with film Ilford (FP4 Iso 125/22°; Ilford Imaging Switzerland GmbH, Marly, Switzerland)). For collagen content quantification, negatives were scanned for further processing. In each digitalized image, the collagen fibrils appeared bright (with high intensity), showing a good contrast to the image background (Figure 6.3). Therefore, the amount of collagen was semiquantitatively estimated as the fraction of high intensity voxels (i.e. voxels whose intensity was larger than a cutoff) compared to the total sum of voxels in an image.

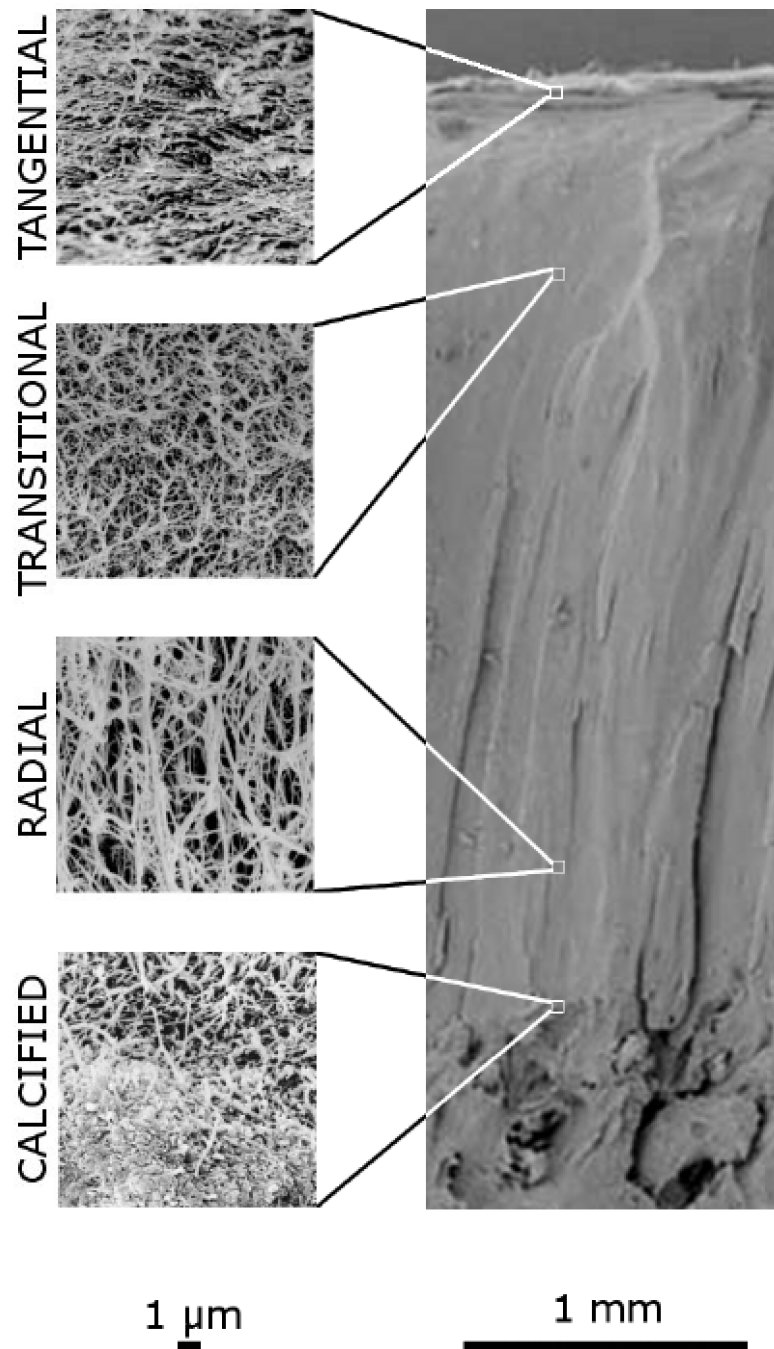


Figure 6.3: Example of fibril arrangement in the different zones of the articular cartilage from top to bottom tangential, transitional, radial and calcified zones. On the right a panoramic SEM view of the complete cartilage height. White squares

---

indicate the position of the high resolution  $6000 \times$  FOV. Imaging scales are given at the bottom.

#### **6.2.4 Histology**

The digitalized Safranin-O stained cuts is an indirect measured of the proteoglycan content. Samples for histological analysis were immersed  $6 \pm 2$  weeks in a 7% EDTA solution at  $37^\circ\text{C}$  for bone decalcification. EDTA solution was changed each 48 h. After decalcification samples were soaked with flowing supply water for two hours to guarantee complete elimination of any remaining EDTA. Decalcified samples were dehydrated in ascending ethanol series (1 h at concentrations of 50%, 70%, 80%, 90% and 100% und subsequently twice for 1 h in Xylol). Samples were embedded in fluid paraffin, cooled at  $4^\circ\text{C}$  for 24 h and microtomed to a thickness of  $7\ \mu\text{m}$  (Schlittenmikrotom, Jung AG, Heidelberg, Germany). Three cut sections were placed on a transparent microscopy slide and dried overnight at  $60^\circ\text{C}$  in an incubator.

The GAG chains of the proteoglycans were then stained by placing deparaffinized cut sections in buffered 0.5% Safranin-O solution for 7 min. For deparaffination, cut sections were burned in for 10 min on a heating plate at  $60^\circ\text{C}$  and dipped in decreasing ethanol series (twice 5 min Xylol and 5 min each in 100%, 96%, 90%, 80%, 70% ethanol). After staining, the cut sections were placed at 100% ethanol and rapidly changed to Xylol for twice 5 min. The cut section was finally covered with a cover slip using a mounting media (Neo-Mount, Merck, Merck, Darmstadt, Germany) and avoiding the formation of air bubbles.

Two representative cut sections of each sample were imaged using a  $1.25\times$  microscope (Wild Makroskop M420, Leica, Heerbrugg, Switzerland) with a  $0.5\times$  objective. Special attention was paid to acquire the images under the same illumination conditions. Images of the cut sections were converted to an inverted grey scale (255-grey values, 255 being the highest grey value), so that relative Safranin-O content could

---

be quantified with the grey level. The contour of the cartilage in each cut section was automatically identified with a self-written program in Matlab. After manual selection of two points at the bone-cartilage interface (BCI) in the center of the cut section, the cartilage was automatically segmented and stretched to a normalized rectangle similarly to the processing of MRI images (see MRI processing). Mean profiles of the grey values between the articular surface (AS) and the BCI were calculated by averaging the rectangle. To facilitate comparison the grey values with the MRI images the resolution of the grey profiles were averaged down to the resolution of MRI images and the grey values scaled between 0 (minimum) and 1 (maximum).

## 6.3 Results

### 6.3.1 MRI

Maps of ADC, FA and of the projection of the first eigenvector in the imaging plane are shown in Figure 6.4 for measurements performed in cartilage with and without loading conditions. Figure 6.5 represents the averaged ADC and FA profiles from the bone-cartilage interface to the articular surface. ADC continuously increased from the BCI,  $(0.72\pm 0.11)\times 10^{-3}$  mm<sup>2</sup>/s, to the AS,  $(1.30\pm 0.07)\times 10^{-3}$  mm<sup>2</sup>/s. FA took large values at the BCI,  $(0.61\pm 0.14)$ , and rapidly decreased towards a minimum,  $(0.06\pm 0.05)$ , at approximately 20% distance from the surface. There was a slight increase of FA closer to the AS,  $(0.09\pm 0.06)$ , which coincides with a region in which the first eigenvector was predominantly oriented parallel to the AS (Figure 6.4).

Loading of the cartilage resulted in significantly ( $P<0.05$ ) reduced ADC in approximately one third of the superficial cartilage (Figure 6.5), and significantly increased FA in the 5% of the cartilage under the articular surface. Interestingly, a significant *reduction* in the FA was found around at 75% distance from the BCI. Loading also led to a reorientation of the first eigenvectors as can be seen in Figure 6.4.

---

The first eigenvectors showed a more horizontal average orientation directly underneath the indenter.

Laterally to the area direct under the indenter a decrease in ADC was observed as far as  $(1.12 \pm 0.06)$  mm both in left and right directions (Figure 6.4). In contrast, no significant changes in FA or first eigenvector were observed laterally to the samples, apart from an increased FA in the tangential zone far away from the indenter.

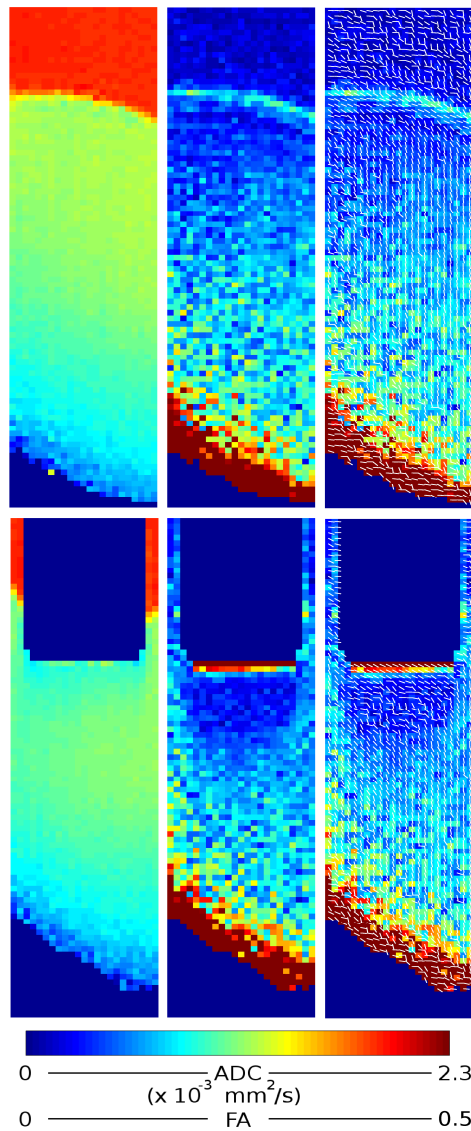


Figure 6.4: Example (from left to right) of ADC, FA and the projection of the first eigenvalue in the image plane. Top: without loading, bottom: with loading.

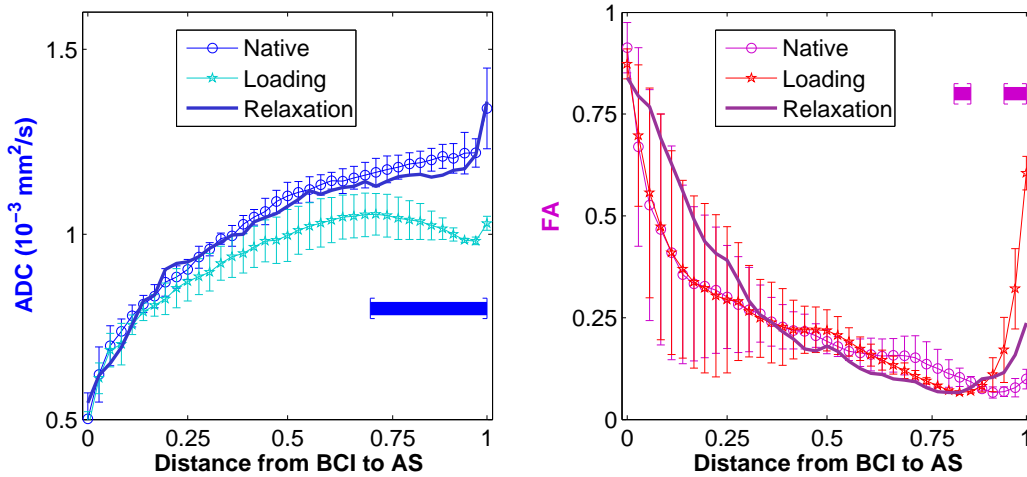


Figure 6.5: ADC and FA without loading (circle, eight samples) and under loading conditions (pentagon, three samples) and after loading (relaxation; solid line, one sample) from the BCI to the AS. Error bars represent the interindividual variability of the data. The horizontal bars indicate the regions where parameters differ significantly (two sample t-test,  $P < 0.05$ ) between loaded and unloaded conditions.

### 6.3.2 Biomechanical testing

The results of the biomechanical testing in the samples are summarized in Table 6.1 together with the mean ADCs, FAs, and grey values of the samples. There was a significant difference in Young's modulus of young ( $\leq 30$  years), ( $0.77 \pm 0.18$ ) MPa, and the older samples ( $> 30$  years), ( $0.63 \pm 0.39$ ) MPa. Samples 4 and 5 were used in a different experiment not reported here and are thus missing in Table 6.1.

There was no significant correlation between Young's modulus and the mean ADC ( $r^2 = 0.19$ ,  $P = 0.7$ ), mean FA ( $r^2 = -0.24$ ,  $P = 0.6$ ) and mean grey ( $r^2 = 0.06$ ,  $P = 0.9$ ) values of the cartilage samples.

---

Sample	Age Y	ADC ( $10^{-3}$ mm <sup>2</sup> /s)	FA	$E_s$ MPa	Grey value
1	17	1.04 (0.12)	0.22 (0.12)	0.56	144.5
2	30	1.08 (0.15)	0.25 (0.13)	0.85	128.3
3	63	1.05 (0.19)	0.28 (0.14)	0.25	96.5
6	47	1.04 (0.15)	0.26 (0.23)	1.03	88.6
7	55	1.07 (0.22)	0.21 (0.18)	0.61	79.2
8	10	1.07 (0.21)	0.21 (0.11)	0.89	123.8

<sup>1</sup> Mean value (standard deviation).

### 6.3.3 SEM

The zonal height measured with DTI and SEM showed a significant ( $P < 0.01$ ) correlation coefficient for the radial ( $r^2 = 0.89$ ) and transitional zones ( $r^2 = 0.87$ ) and a low correlation of 0.10 for the tangential zone. Bland-Altman plots (Figure 6.6) show that DTI has a tendency to overestimate the radial zone, although not significantly ( $P > 0.01$ ).

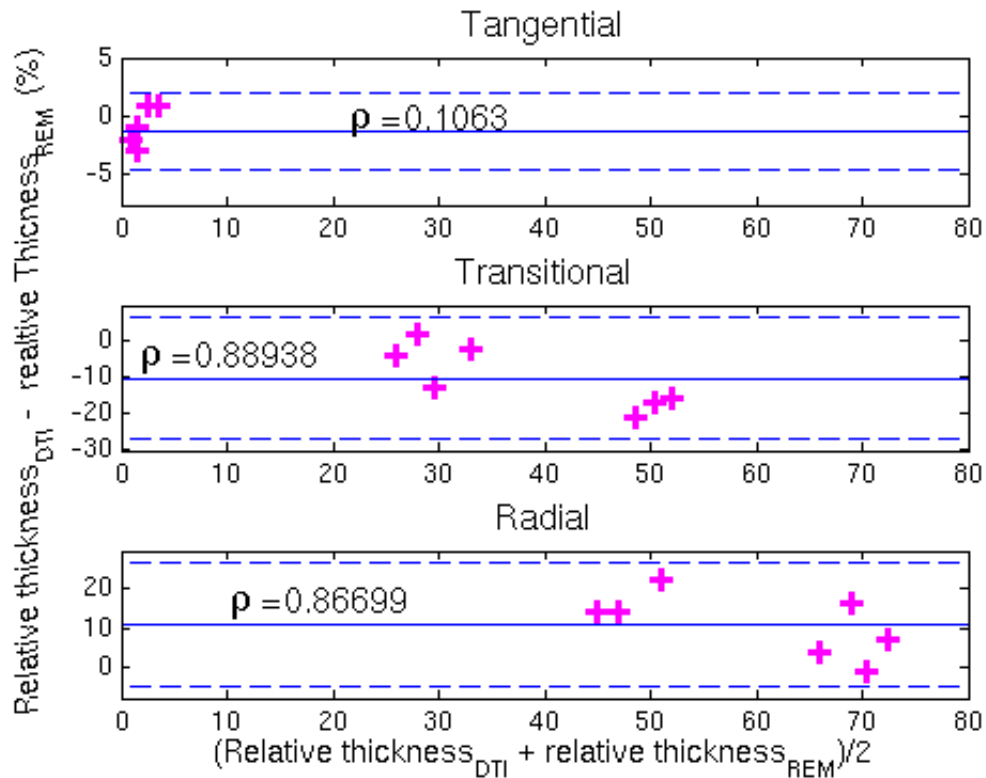


Figure 6.6: Bland-Altman plots of the thickness measured in the DTI and SEM for the radial, transitional and tangential zones. Correlation coefficients,  $\rho$ , are displayed on the axis.

The semiquantitative evaluation of the collagen content in all regions of the cartilage is summarized in Table 6.2. Collagen content decrease from the AS to the transitional zone and increased from the tangential zone to the BCI.

Zone	Mean	Std.dev.	Min	Max
Tangential	73.1	11.4	57.4	87.5
Transitional	52.7	9.3	42.6	63.7
Radial	65.0	8.9	49.6	75.4
Calcified <sup>1</sup>	63.9	4.3	60.8	67.0

<sup>1</sup> Only two images of the calcified zone were acquired

---

### 6.3.4 Histology

Figure 6.7 shows an example of the histological cut of one of the samples, together with the steps in image processing. The averaged normalized grey profile over all samples is represented in Figure 6.8. The grey values grew continuously from the AS to approximately the 75% of the cartilage depth and remained constant or slightly decreasing, in the depth radial zone. Interestingly, in most of the samples an increased grey value was found close to the AS.

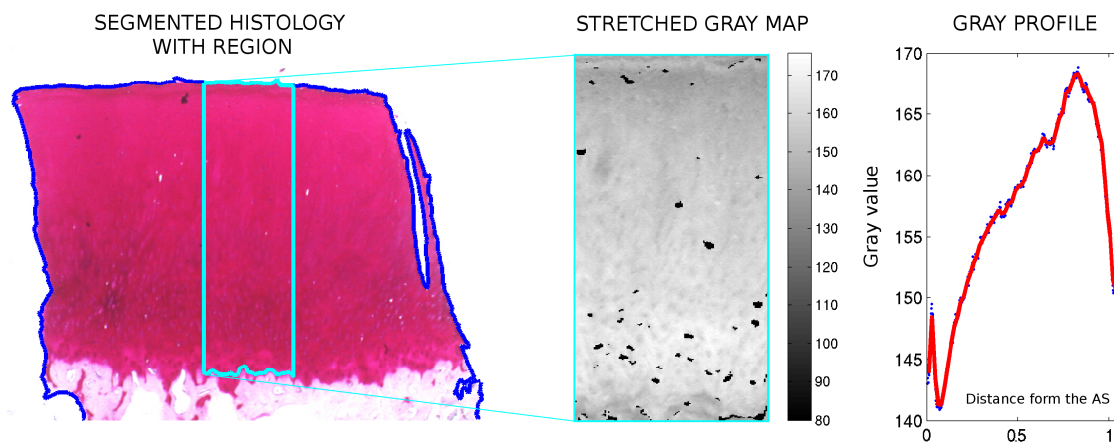


Figure 6.7 Example of a histological cut with the automatic contour and the segmentation overlaid. Segmented cartilage is converted to grey and stretched to fill a rectangle. Averaging in the horizontal direction resulted in a grey profile (blue points). The resolution of the grey profile is averaged down to fit the resolution of MRI images (red line).

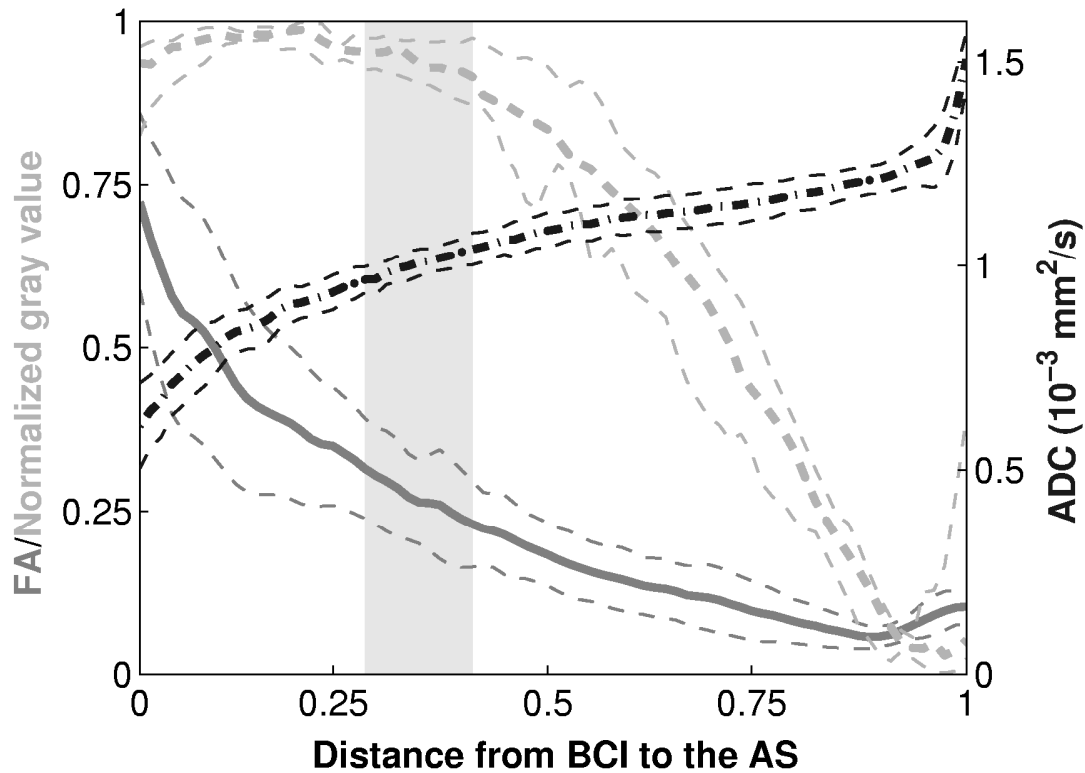


Figure 6.8: ADC (black dashed line), FA (dark grey continuous line) and grey values (light grey dashed line) averaged over all samples from the BCI (distance=0) to the AS (distance=1). The 1- $\sigma$  interval is represented for each parameter as thin dashed lines.

Pooled FA and ADC values of all samples have been plotted against their corresponding grey values (Figure 6.9). Both ADC and FA showed two well-differentiated regions with respect to the grey values, which are related to the proteoglycan content. ADC values larger than approximately  $1.0 \cdot 10^{-3} \text{ mm}^2/\text{s}$  (values in the superficial 75% of the cartilage) decayed inversely proportional to the grey values. Below  $1.0 \cdot 10^{-3} \text{ mm}^2/\text{s}$ , the grey values did not account for the decay in ADC. The FA slightly increased with the increased grey values up to a value around 0.25, which again occurs at a 75% of the cartilage height from the AS. Beyond this point, large increments on FA occurred at almost constant grey values. The transition of these two regions is indicated in Figure 6.8 by a grey band.

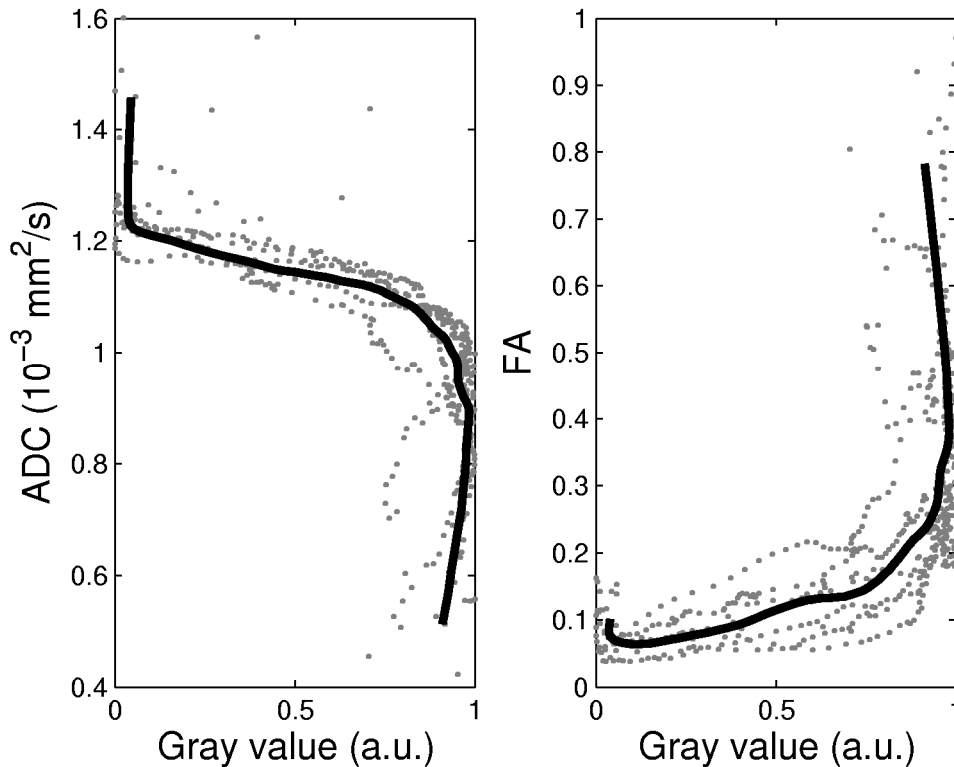


Figure 6.9: Grey values represented against the ADC and FA values for all samples, from which histology was present. Note the two well-differentiated diffusion regimens. The FA diagrams showed a low correlation between grey values and FA.

## 6.4 Discussion and conclusions

The following relationship of ADC, FA and the first eigenvector to structural and compositional properties of human articular cartilage could be derived.

### 6.4.1 Comparison with previous DTI in articular cartilage

The ADC and FA values measured in this study are in good agreement with previously reported data (Filidoro 2005; Deng 2007; Meder 2006; Raya 2008; Raya 2011; de Visser 2008). The somewhat lower ADC values in our study are probably due to the

---

lower temperature at which the MRI was performed (between 17°C and 19°C). The projections of the first eigenvector for 9.4 T (Figure 4.7) and for 17.6 T (Figure 6.4) are in good agreement as well.

It is interesting to compare the SNR level for 9.4 T and 17.6 T. SNR was calculated from the images without diffusion for all samples and then averaged. Figure 6.10 shows the SNR versus the distance from the cartilage surface. SNR profiles were similar and SNR values for 17.6 T were higher, which is well explicable through the higher field strength and the greater number of repetitions.

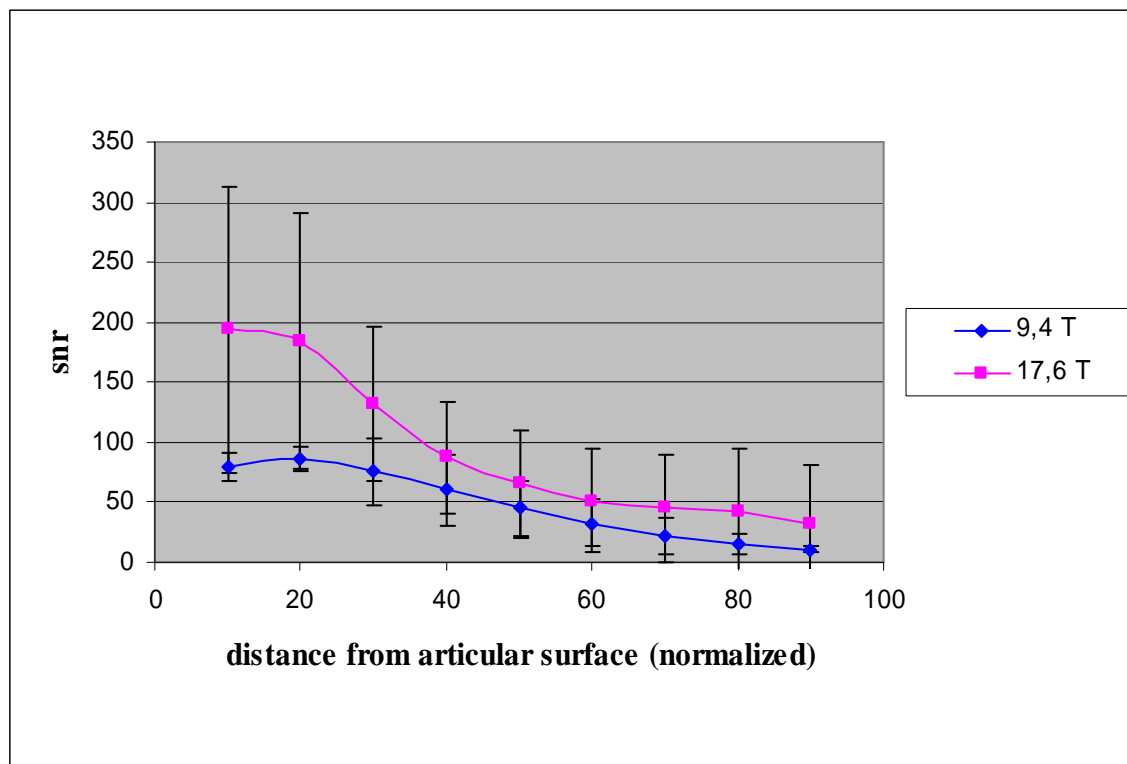


Figure 6.10: SNR of the cartilage versus the distance from the cartilage surface. The SNR is calculated for the diffusion-weighted image with b-value 0.5 s/mm<sup>2</sup> and averaged on all measurements. 9 sub-ROI were considered.

---

## 6.4.2 DTI under mechanical loading

In accordance with the results in bovine articular cartilage (de Visser 2008b) and in human patellar cartilage (Filidoro 2004; Raya 2008; Raya 2011), indentation of the samples produced changes in ADC, FA and the first eigenvector. A significant reduction of the ADC was found in the upper 30% of the cartilage. The significantly increased FA directly underneath and in the immediate vicinity of the indenter together with the higher share of the first eigenvectors oriented parallel to the surface of the indenter, are compatible with local compressive stress acting on the collagenous fiber network. Under loading, the orientation of the first eigenvector follows the expected changes in fiber orientation as demonstrated by SEM (Glaser 2002). Additionally to the increased FA, a significant decrease in FA was observed between 40% and 20% of the distance from the superficial cartilage (Figure 6.4-6.5). This reduction might be a sign of the ‘crimp’ presented by the collagen fibers in the area underneath the indentation (Glaser 2002). For the strain used in this work (20% of the cartilage height), this crimp is only expected in the transitional zone (Glaser 2002).

The increased FA observed in the tangential zone far away from the indenter is consistent with a higher degree of tangentially oriented fibers. It thus supports the hypothesis that the tangential zone distributes locally applied (compressive) stress laterally over a larger cartilage volume (Broom 1985; Glaser 2002).

Between the ADC and FA as well as the gray values measured from the digitalized Safranin-O stained cuts and the Young’s modulus, no significant dependence could be established. Here, future work can be done, which appears to require a much higher number of samples of healthy patellar cartilage than those included herein.

## 6.4.3 DTI versus SEM

The good correlation derived within this study between the height of the different cartilage zones as measured by the first eigenvector and SEM now gives direct evidence

---

for a close relationship between the average orientation of the collagenous fibers and the first eigenvector. The slight underestimation of the superficial zone (Figure 6.6) presumably is due the shrinking of the sample during preparation for SEM.

The relationship of the first eigenvector was first suggested by Filidoro et al. (Filidoro 2005), and more recently investigated using the polarized light microscopy (deVisser 2008b). De Visser et al. (deVisser 2008b) found a good statistical agreement between the angle of the projection of the first eigenvector in the imaging plane and the collagen fibril orientations as measured with polarized light microscopy.

#### **6.4.4 DTI versus Histology**

Histology with Safranin-O stain allows semiquantitatively analyzing the proteoglycan content in the cartilage. Safranin-O is a cationic dye of low molecular weight which selectively bounds to the glycosaminoglycans in cartilage. In sectional cuts the concentration of Safranin-O was found to be proportional to the negative fixed charge in cartilage, which is uniquely due to glycosaminoglycans (Kiviranta 1984). Since it was not possible to determine the exact concentration of Safranin-O, only the relative proteoglycan content could be established. The increased concentration of glycosaminoglycans towards the bone-cartilage interface measured in this work is in good agreement with the distribution found with biochemical analysis by other authors (Bayliss 1983; Kiviranta 1984).

#### **6.4.5 Influence of cartilage components on the measured parameters**

For the short diffusion times used in this work (section 5.3), diffusivity is predominately determined by the volume fraction of free water (Knauss 1999), i.e., the volume of water divided by the cartilage volume. Therefore it is expected that the diffusivity decreases as the proteoglycan and collagen density increases. The correlation of the diffusion parameters with the histology seems to indicate that both collagen and

---

proteoglycan contribute to ADC and FA. ADC and FA plotted against the histology gray values are shown in Figure 6.9. ADC presented three well differentiated regions when correlated with the gray values. Low gray values at the articular surface correspond to high ADCs of around  $1.5 \times 10^{-3} \text{ mm}^2/\text{s}$ . These high ADCs may be a consequence of partial volume effects with the physiologic saline solution (remember the large slice thickness of 1.5 mm). In the second region, ADC decreases almost linearly as the proteoglycan content increases, thus indicating that the decrease of ADC in this region can be to some extent explained by the increase in proteoglycan content. However, for ADCs below approximately  $1.0 \times 10^{-3} \text{ mm}^2/\text{s}$ , the data present a sharp decay at almost constant gray values (see the bend in Figure 6.8), thus indicating that a different component of the extracellular matrix determining the diffusivity may predominate in this region.

There are two possible explanations for the decrease in ADC. The first is the increase of the collagen content from the transitional zone to the radial zone (see Table 2). Although the values in Table 2 are only semi-quantitative, several biochemical studies have analyzed the distribution of collagen in cartilage and found that collagen content decreases from the articular surface (21%) to the middle zone of the cartilage (15%) and then increases again towards the bone-cartilage interface (19%) (Muir 1970; Venn 1977; Maroudas 1980).

A second explanation is the presence of two T2 components close to the BCI, a fast T2 component,  $T_{2f}$ , of around 2-4 ms and a slow T2 component,  $T_{2s}$ , of 30 ms (Keinan-Adamsky 2006; Shinar 2006). From the BCI to the AS  $T_{2f}$  increases and its weight decreases (from  $T_{2f} = 4 \text{ ms}$  with a weight of 80% at the BCI to 15 ms and 40% weighting at 60% of the cartilage height (Shinar 2006)).  $T_{2s}$  and  $T_{2f}$  are sensitive to different dipolar interactions (Keinan-Adamsky 2006).  $T_{2s}$  is principally influenced by the dipolar interaction due to oriented collagen fibrils, whereas  $T_{2f}$  is influenced by the isotropic dipolar interactions either caused by isotropic reorientation of the water molecules or by proton exchange with chemically shifted protons of the NH and OH

---

groups (Keinan-Adamsky 2006). Therefore, it is likely that both components have different diffusion properties. Due to the diffusion gradients, the TE of the diffusion-weighted spin-echo sequence was 16 ms, which may be large enough to strongly reduce the contribution of the fast T2 component (for the pig model of (Keinan-Adamsky 2006) the TE is four times larger than T<sub>2f</sub>).

At last we would like to point out that the existence of the two diffusion regimens does not mean that the diffusion properties are only consequence of one of the components. With our data it is only possible to relate changes in DTI parameters with changes in proteoglycan content, and in a much minor extent with collagen. As Knauss et al. demonstrated (Knauss 1999), at low diffusion times (here 5.85 ms) the diffusivity is primarily determined by the water content so that it is expected that both proteoglycans and collagen contributes to diffusivity. This is corroborated by the fact that in trypsin (Knauss 1999; Meder 2006; Deng 2007) and collagenase (Knauss 1999; Deng 2006) degraded cartilage, a systematic increase of the ADC was found.

#### **6.4.6 Conclusions**

The results presented in this chapter demonstrate that ADC and FA depend both on proteoglycan and collagen content, although differently in the superficial and deep regions of the cartilage, and that the first eigenvector, indicating the main diffusion direction, is closely related to the collagen architecture.

---

## 7 Conclusions and summary

Articular cartilage is a highly structured tissue and plays an important role in the pathogenesis of osteoarthritis (OA), which is a global socioeconomic burden (Yelin 1995, MacLean 1998, Buckwalter 1997). The degradation of articular cartilage is considered to be an entry point in the process of irreversible joint degeneration. Loss of integrity within the collagenous fiber network is considered to be a hallmark of transition from potentially reversible to irreversible degeneration of articular cartilage long before macroscopically visible loss of cartilage substance occurs (Buckwalter 1997). Consequently, there is a strong need to diagnose cartilage damage early, and increasing efforts are made to develop and to validate effective disease-modifying therapies.

Magnetic resonance imaging (MRI) is a noninvasive imaging technique used primarily in medical settings to produce high quality images of the inside of the human body. MRI is based on the principles of nuclear magnetic resonance (NMR), i. e., the coherent resonant excitation of the atomic nuclei in a static magnetic field with electromagnetic radio frequency pulses. Diffusion tensor imaging (DTI) is an MRI technique based on the orientation-dependent measurement of the molecular diffusion properties of water, which can be employed to analyze the tissue ultrastructure by measuring the internal anisotropy and the main directions of local diffusion in a tissue. Thus, DTI may come very helpful for analyzing articular cartilage because it may be capable to reflect early changes in the alignment of the collagenous fibers.

The value of water diffusion as a marker for OA is largely known. First invasive measurements of the diffusion in cartilage were performed by Maroudas et al. (Maroudas 1968, Maroudas 1977), who obtained increased apparent diffusion coefficients (ADCs) in OA cartilage. Since MRI can measure diffusivity non-invasively

---

at scales of microns, diffusion can be an interesting biomarker for the early diagnosis of OA. Early works on spectroscopy and DWI of the cartilage demonstrated the increment of diffusion with enzymatic cartilage degradation (Burstein 1993).

This PhD thesis consists of two parts. Aims of the first part (cf. chapter 4) were to assess the feasibility of DTI at a magnetic field strength of 9.4 Tesla for analyzing human hyaline articular cartilage and to evaluate whether DTI can demonstrate zonal architectural properties of articular cartilage. In the second part (cf. chapters 5 and 6), the meaning of the DTI parameters determined at 17.6 Tesla are systematically examined with respect to the proteoglycan and collagen content and the relationship between the DTI parameters and the mechanical properties of cartilage are presented.

The presented results at 9.4 T confirm the feasibility and applicability of DTI experiments for structural analysis of hyaline articular cartilage in high-field-strength MRI. The mean diffusivity, the fractional anisotropy (FA), and the eigenvector projection map show characteristic variations throughout the depth of cartilage. Based on these maps, eigenvectors are confirmed to be the most promising parameters to characterize the zonal architecture of cartilage. These results are in good agreement with the current literature about hyaline articular cartilage architecture as defined by the collagenous fibers. Accordingly, the results confirm the suggestion in the literature that DTI eigenvector analysis is related to the alignment of the collagenous fibers in cartilage, this confirmation being relevant to the detection of early cartilage damage in OA.

For the second part of this work, a 17.6-Tesla scanner was employed and histology, SEM, and mechanical investigation of the cartilage sample were performed. The ADC and FA values measured in this study are in good agreement with previously reported data for high-field measurements.

The geometric profile of the measured ADCs finds an explanation through the effect of proteoglycan content, collagen content, and possibly through the presence of two T2 components close to the bone-cartilage interface. While ADC decreases from the cartilage surface to the bone-cartilage interface with the increase of proteoglycan

---

content, which is known from histology, the ADC shows a sharp decay at almost constant proteoglycan content for values below approximately  $1.0 \times 10^{-3} \text{ mm}^2/\text{s}$ . Therefore, the results indicate that both possible explanations for this higher decrease in ADC (the first being the increase of the collagen content from the transitional zone to the radial zone; and the second being the presence of two T2 components close to the bone-cartilage interface) maintain so far their validity also when high fields are applied.

FA has a general slightly increasing tendency from the cartilage surface to the bone-cartilage interface with the increase of the proteoglycan content. The strong increase of FA directly at the cartilage surface and in the radial zone, where the content of proteoglycan is approximately constant, confirms the relevance of the influence of the collagen structure.

The good correlation in this study between the height of the different cartilage zones as measured by the first eigenvector on the one hand and SEM images on the other hand gives direct evidence for a close relationship between the average orientation of the collagenous fibers and the orientation of the first eigenvector.

Finally in accordance with earlier results in bovine articular cartilage and in human patellar cartilage, indentation of the samples leads to changes in ADC, FA, and the first eigenvector. Under load, the orientation of the first eigenvector follows the expected changes in fiber orientation as demonstrated by SEM. The increased FA observed in the tangential zone far away from the indenter is consistent with a higher degree of tangentially oriented fibers. The results thus support the hypothesis that locally applied (compressive) stress is distributed laterally over a larger cartilage volume.

In conclusion, this work demonstrates the feasibility of DTI of articular cartilage with high spatial resolution at 9.4 and 17.6 Tesla and establishes relationships between DTI parameters on the one hand and the zonal cartilage architecture and the constituents of the extracellular matrix (proteoglycan and collagen) on the other hand.



---

## Zusammenfassung

Der Gelenkknorpel ist ein hochstrukturiertes Gewebe und spielt eine wichtige Rolle in der Pathogenese der Osteoarthritis (OA), die eine weltweite soziale und wirtschaftliche Belastung darstellt (Yelin 1995, MacLean 1998, Buckwalter 1997). Die Zerstörung des Gelenkknorpels wird als Startpunkt für den Prozess der irreversiblen Gelenkdegeneration betrachtet. Dabei wird ein Verlust der Integrität des Kollagenfasernetzes im Gewebe als Zeichen des Übergangs von potentiell reversibler zu irreversibler Degeneration angesehen, welches dem Entstehen eines makroskopisch erkennbaren Knorpelverlusts vorangeht (Buckwalter 1997). Infolgedessen besteht ein hoher Bedarf an Techniken zur Frühdiagnostik erster Knorpelschäden, und es wird zunehmend in die Entwicklung und Verifizierung von effektiven Therapien investiert.

Die Magnetresonanztomographie (MRT) ist eine nichtinvasive bildgebende Technik, die primär in medizinischen Anwendungen zur Aufnahme hochqualitativer Bilder aus dem Körperinneren dient. Die MRT basiert auf dem Prinzip der Kernspinresonanz (*nuclear magnetic resonance*, NMR), also der kohärenten resonanten Anregung von Atomkernen im statischen Magnetfeld mit elektromagnetischen Hochfrequenzpulsen. Die Diffusionstensor-Bildgebung (*diffusion tensor imaging*, DTI) ist eine MRT-Technik, die auf der richtungsabhängigen Messung von molekularen Diffusionseigenschaften beruht und zur Analyse der mikroskopischen Gewebe(ultra)struktur verwendet werden kann, indem die innere Anisotropie und die Hauptrichtungen der lokalen Diffusion im Gewebe gemessen werden. Insofern erscheint die DTI äußerst nützlich für die Untersuchung des Gelenkknorpels, da sie zur Darstellung erster Veränderungen in der Ausrichtung der Kollagenfasern geeignet ist.

Der Diffusionskoeffizient als Marker für Osteoarthritis ist allgemein bekannt. Erste invasive Messungen der Diffusion in Knorpel wurden von Maroudas et al. (Maroudas 1968, Maroudas 1977) durchgeführt, welche einen erhöhten Diffusionskoeffizienten im

---

osteoarthrotischen Knorpel ermittelten. Da mittels Kernspintomographie die molekulare Diffusionsbewegung nichtinvasiv auf einer Größenordnung von Mikrometern gemessen werden kann, dient die Diffusion als Biomarker für die Frühdiagnose der Osteoarthrose. Erste Arbeiten zur Spektroskopie und zur diffusionsgewichteten Bildgebung des Knorpels zeigten die Zunahme der Diffusion bei enzymatischer Knorpeldegradierung (Burstein 1993).

Die vorliegende Dissertation besteht aus zwei Teilen. Ziele des ersten Teils (Kapitel 4) dieser Arbeit waren, die Durchführbarkeit der Diffusionstensor-Bildgebung bei einer magnetischen Feldstärke von 9.4 Tesla in der Analyse des menschlichen hyalinen Gelenkknorpels zu untersuchen und zu evaluieren, ob die Diffusionstensor-Bildgebung zonale Eigenschaften der Architektur des Gelenkknorpels darstellen kann. Im zweiten Teil (Kapitel 5 und 6) wird die Bedeutung der bei 17.6 Tesla bestimmten DTI-Parameter systematisch bezüglich des Proteoglykan- und Kollagengehalts überprüft und eine Beziehung zwischen den DTI-Parametern und den mechanischen Eigenschaften des Knorpels hergestellt.

Die Ergebnisse bei 9.4 Tesla bestätigen die Durchführbarkeit und Anwendbarkeit von DTI-Experimenten zur Strukturanalyse des hyalinen Gelenkknorpels in der Hochfeld-MRT. Der Diffusionskoeffizient, die fraktionelle Anisotropie (FA) sowie die Darstellung der Eigenvektorprojektionen in Parameterkarten zeigen über die Knorpeltiefe hinweg charakteristische Änderungen. Basierend auf diesen Parameterkarten erweisen sich die Eigenvektoren als der vielversprechendste Parameter zur Charakterisierung der zonalen Architektur des Knorpels. Diese Ergebnisse sind in guter Übereinstimmung mit der aktuellen Literatur über die Architektur des durch Kollagenfasern definierten hyalinen Gelenkknorpels. Dementsprechend bestätigen die Ergebnisse den in der Literatur vertretenen Vorschlag, dass die Resultate der Eigenvektoranalyse mittels DTI im Zusammenhang mit der Ausrichtung der Kollagenfasern in Knorpel stehen, was wiederum für die Früherkennung von Knorpelschäden bei der Osteoarthrose relevant ist.

---

Für den zweiten Teil dieser Arbeit wurde ein 17.6 Tesla-Gerät verwendet sowie parallel eine Histologie, eine Rasterelektronenmikroskopie (REM) und eine mechanische Belastungsprüfung der Knorpelprobe durchgeführt. Die dabei gemessene Diffusionskoeffizienten (ADC) und die FA-Werte stimmen gut mit zuvor berichteten Daten für Hochfeldmessungen überein.

Das geometrische Profil der gemessenen ADCs kann durch die Wirkung des Proteoglykangehalts, des Kollagengehalts und möglicherweise durch das Vorhandensein von zwei T2-Komponenten nahe dem Knochen-Knorpel-Übergang erklärt werden. Während der ADC von der Knorpeloberfläche hin zum Knochen-Knorpel-Übergang mit (aus der Histologie bekanntem) ansteigendem Proteoglykangehalt abnimmt, zeigt der ADC einen scharfen Abfall bei beinahe konstantem Proteoglykangehalt für Werte unterhalb von etwa  $1.0 \times 10^{-3} \text{ mm}^2/\text{s}$ . Daher weisen die Ergebnisse darauf hin, dass beide möglichen Erklärungen für diese höhere Abnahme des ADCs (sowohl das Ansteigen des Kollagengehalts von der Übergangszone zur Radialzone als auch das Vorhandensein zweier T2-Komponenten nahe dem Knochen-Knorpel-Übergang) auch bei hohen Feldstärken weiter ihre Gültigkeit behalten.

Die FA weist bei steigendem Proteoglykangehalt von der Knorpeloberfläche hin zum Knochen-Knorpel-Übergang eine allgemein leicht ansteigende Tendenz auf. Das starke Ansteigen der FA direkt an der Knorpeloberfläche und in der Radialzone, in der der Proteoglykangehalt näherungsweise konstant ist, bestätigt die Relevanz des Einflusses der Kollagenstruktur.

Die in dieser vergleichenden Analyse erhaltene gute Übereinstimmung zwischen der Höhe der unterschiedlichen Knorpelzonen, einerseits durch Messung des ersten Eigenvektors und andererseits durch REM-Bilder, liefert einen direkten Nachweis für einen engen Zusammenhang zwischen der gemittelten Ausrichtung der Kollagenfasern und der Orientierung des ersten Eigenvektors.

Schließlich führt ein Eindringen (*indentation*) der Proben in Übereinstimmung mit früheren Ergebnissen zu Änderungen von ADC, FA und dem ersten Eigenvektor. Unter Last folgt die Orientierung des ersten Eigenvektors den erwarteten Änderungen

---

entsprechend der durch die REM demonstrierten Faserausrichtung. Die in der Tangentialzone weit von dem Stempel entfernt beobachtete höhere FA passt zu einem höheren Maß an tangential ausgerichteten Fasern. Die Ergebnisse stützen somit die Vermutung, dass eine lokal aufgebrachte kompressive Spannung lateral über ein größeres Knorpelvolumen verteilt wird.

Zusammenfassend zeigt die vorliegende Arbeit, dass DTI-Messungen am Gelenkknorpel mit hoher räumlicher Auflösung bei 9.4 und 17.6 Tesla durchführbar sind, und etabliert Zusammenhänge zwischen DTI-Parametern einerseits und der zonalen Knorpelarchitektur und den Bestandteilen der extrazellulären Matrix (Proteoglykan und Kollagen) andererseits.

---

# Bibliography

- Alberts 1994            Alberts B, Bray D, Lewis J, Raff M, Roberts K, Watson JD. Molecular Biology of the Cell (3<sup>rd</sup> Edition). New York, USA, Garland Publishing, 1994.
- Basser 1994            Basser PJ, Mattiello J, LeBihan D. MR diffusion tensor spectroscopy and imaging. *Biophys J.* 1994;66(1):259-267.
- Basser 1994-b         Basser PJ, Mattiello J, Le Bihan D. Estimation of the effective self-diffusion tensor from the NMR spin echo. *J Magn Reson B* 1994;103:247-254.
- Basser 1992            Basser PJ, Le Bihan D. Fiber orientation mapping in an anisotropic medium with NMR diffusion spectroscopy. *Proceedings 11<sup>th</sup> Scientific Meeting ISMRM, Berlin, Germany, 11:1221, 1992.*
- Basser 1998            Basser PJ, Pierpaoli CA. A simplified method to measure the diffusion tensor from seven MR images. *Magn Reson Med* 1998; 39:928-934.
- Basser 2002            Basser PJ, Jones DK. Diffusion-tensor MRI: theory, experimental design and data analysis - a technical review. *NMR Biomed* 2002;15:456-467.

- 
- Bastin 1998 Bastin ME, Armitage PA, Marshall I. J Magn Reson Imaging 1998;16:773-785.
- Bauer 1998 Bauer A, Stabler A, Bruning R, Bartl R, Krodel A, Reiser M, and Deinling M. Diffusion-weighted MR imaging of bone marrow: Differentiation of benign versus pathologic compression fracture. Radiology 1998;207:349-356.
- Bayliss 1983 Bayliss MT, Venn M, Maroudas A, Ali SY. Structure of proteoglycans from different layers of human articular cartilage. Biochem J 1983;209:387-400.
- Behr 2004 Behr VC, Weber T, Neuberger T, Vroemen M, Weidner N, Bogdahn U, Haase A, Jakob PM, Faber C. High-resolution MR imaging of the rat spinal cord in vivo in a wide-bore magnet at 17.6 Tesla. MAGMA 2004;17:353-358.
- Bernstein 2004 Bernstein MA, King KF, Zhou XJ. MRI Pulse Sequence. Elsevier Academic Presse, 2004
- Bloch 1946 Bloch F. Nuclear induction. Phys Rev 1946;70: 460-474.
- Bodammer 2004 Bodammer N, Kaufmann J, Kanowski M, Tempelmann, C. Eddy current correction in diffusion-weighted imaging using pairs of images acquired with opposite diffusion gradient polarity. Magn Reson Med 2004;51:188-193.
- Brandt 2009 Brandt KD, Dieppe P, Radin E. Etiopathogenesis of osteoarthritis. Med Clin North Am 2009;93:1-24.

- 
- Brooks 2002 Brooks SA, Dwek MV, Schumacher U. Functional and Molecular Glycobiology. Oxford, England, Bios Scientific Publishers, 2002
- Broom 1985 Broom ND, Marra DL. New structural concepts of articular cartilage demonstrated with a physical model. Connect Tissue Res. 1985;14:1-8.
- Broom 1986 Broom ND. The collagenous architecture of articular cartilage-a synthesis of ultrastructure and mechanical function. J Rheumatol 1986;13:142-152.
- Buckwalter 1997 Buckwalter JA, Mankin HJ. Articular cartilage: part I - II. J Bone Joint Surg 1997;79-A(4):600-632.
- Burstein 1993 Burstein D, Gray ML, Hartman AL, Gipe R, Foy BD. Diffusion of small solutes in cartilage as measured by nuclear magnetic resonance (NMR) spectroscopy and imaging. J Orthop Res 1993;11: 465-478.
- Carr and Purcell 1954 Carr HY, Purcell EM. Effects of diffusion on free precession in nuclear magnetic resonance experiments. Phys Rev 1954;3:630-638.
- Clark 1997 Clark JM, Norman A, Nötzli H. Postnatal development of the collagen matrix in rabbit tibial plateau articular cartilage. J Anat 1997;191:215-227.
- Clarke 1971 Clarke IC. Articular cartilage: a review and scanning electron microscope study. J Bone Joint Surg 1971;53-B:732-750.

- 
- Cleveland 1976      Cleveland GG, Chang DC, Hazlewood CF, Rrschach HE. Nuclear magnetic resonance measurement of skeletal muscle: anisotropy of the diffusion coefficient of the intracellular water. *Biophys J* 1976;16:1043-1053.
- Deng 2007            Deng X, Farley M, Nieminen MT, Gray M, Burstein D. Diffusion tensor imaging of native and degenerated human articular cartilage. *J Magn Reson Imaging* 2007;25:168-171.
- de Visser 2008      de Visser SK, Crawford RW, Pope JM. Structural adaptations in compressed articular cartilage measured by diffusion tensor imaging. *Osteoarthritis Cartilage* 2008;16:83-89.
- de Visser 2008b     de Visser SK, Bowden JC, Wentrup-Byrne E, Rintoul L, Bostrom T, Pope JM, Momot KI. Anisotropy of collagen fibre alignment in bovine cartilage: comparison of polarised light microscopy and spatially resolved diffusion-tensor measurements. *Osteoarthritis Cartilage* 2008;16:689-697.
- Di Lullo 2002      Di Lullo GA, Sweeney SM, Körkkö J, Ala-Kokko L, San Antonio JD. Mapping the ligand-binding sites and disease-associated mutations on the most abundant protein in the human, type I collagen. *J Biol Chem* 2002;277:4223-4231.
- Edelstein 1984      Edelstein WA, Bottomley PA, Pfeifer LM. A signal-to-noise calibration procedure for NMR imaging systems. *Med Phys* 1984;11:180-185.
- Egglı 1988            Egglı PS, Hunziker EB, Schenk RK. Quantitation of structural features characterizing weight- and less-weight-bearing regions in

- 
- articular cartilage: a stereological analysis of medial femoral condyles in young adult rabbit. *Anat Rec* 1988;222:217-227.
- Eisenberg 1985 Eisenberg SR, Grodzinsky AJ. Swelling of articular cartilage and other connective tissues: Electromechanochemical forces. *J Orthop Res* 1985;3:148-159.
- Filidoro 2004 Filidoro L, Glaser C, Dietrich O, Weber J, Oerther T, Wick M, Reiser MF, Raya J. Diffusion tensor analysis of anisotropy in human articular cartilage. *MAGMA 21<sup>st</sup> ESMRMB Copenhagen, Denmark*, 17:114, 2004.
- Filidoro 2005 Filidoro L, Dietrich O, Weber J, Rauch E, Oerther T, Wick M, Reiser MF, Glaser C. High-resolution diffusion tensor imaging of human patellar cartilage: feasibility and preliminary findings. *Magn Reson Med* 2005;53:993-998.
- Filidoro 2008 Filidoro L, Weber DL, Arnoldi AP, Weber J, Raya JG, Jakob PM, Reiser MF, Putz R, Mützel E, Glaser C. Collagenous Fibre architecture of articular cartilage: comparison between high field DTI and scanning electron microscopy. *ECR, Wien, Austria*, B-578, 2008.
- Firbank 1999 Firbank MJ, Coulthard A, Harrison RM, Williams ED. *Phys Med Biol* 1999;44:261-264.
- Frank 1999 Frank LR, Wong EC, Luh WM, Ahn JM, Resnick D. Articular cartilage in the knee: mapping of the physiologic parameters at MR imaging with a local gradient coil-preliminary results. *Radiology* 1999;210:241-246.

- 
- Garrido 1994            Garrido L, Wedeen VJ, Kwong KK, Spencer UM, Kantor HL. Anisotropy of water diffusion in the myocardium of the rat. *Circul Res* 1994;74:789-793.
- Geneser 1990            Geneser F. *Histologie*. pp 211-216. Deutscher Ärzteverlag. 1990.
- Gerlach and Stern 1924      Gerlach W and Stern O. Über die Richtungsquantelung im Magnetfeld. *Ann Phys*1924;74:673.
- Glaser 1998            Glaser C. Kollagenfaserarchitektur des Gelenkknorpels unter verschiedenen mechanischen Belastungssituationen. München, Germany, Dissertation LMU, 1998.
- Glaser 2002            Glaser C, Putz R. Functional anatomy of articular cartilage under compressive loading. Quantitative aspects of global, local and zonal reactions of the collagenous network with respect to the surface integrity. *Osteoarthritis cartilage* 2002;10:83-99.
- Glaser 2005            Glaser C. New techniques for cartilage imaging: T2 relaxation time and diffusion-weighted MR imaging. *Radiol Clin North Am* 2005;43:641-53.
- Glaser 2006            Glaser C. Imaging of cartilage. *Radiologe* 2006;46:16-25.
- Güllmar 2008            Güllmar D. Anisotropic EEG/MEG volume conductor modeling based on diffusion tensor imaging. Dissertation Fakultät für Informatik und Automatisierung der Technischen Universität Ilmenau 2008.

- 
- Gulani 1997 Gulani V, Iwamoto GA, Jiang H, Shimony JS, Webb AG, Lauterbur PC. A multiple echo pulse sequence for diffusion tensor imaging and its application in excised rat spinal cords. *Magn Reson Med* 1997;38:868-873.
- Haacke 1999 Haacke EM, Brown RW, Thompson MR, Venkatesan R. *Magnetic resonance imaging: Physical principles and sequence design*. New York, USA. John Wiley & Sons, 1999.
- Hayes 1972 Hayes WC, Keer LM, Herrmann G, Mockros LF. A mathematical analysis for indentation tests of articular cartilage. *Journal of Biomechanics* 1972;5:541-551.
- Henkelman 1994 Henkelman RM, Stanisz GJ, Kim JK, Bronskill MJ. Anisotropy of NMR properties of tissues. *Magn. Reson Med* 1994;32:592-601.
- Holmes 1998 Holmes MW, Bayliss MT, Muir H. Hyaluronic acid in human articular cartilage. Age-related changes in content and size. *Biochem J* 1998;250:435-441.
- Hornak 2010 Hornak JP. *The basic of MRI*. 2010.  
<http://www.cis.rit.edu/htbooks/mri/>
- Hsu 1998 Hsu EW, Muzikant AL, Matulevicius SA, Penland RC, Henriquez CS. Magnetic resonance myocardial fiber orientation mapping with direct histological correlation. *Am J Physiol* 1998;274:1627-1634.

- 
- Hsu 1999 Hsu EW, Setton LA. Diffusion tensor microscopy of intervertebral disc annulus fibrosus. *Magn Reson Med* 1999;41:992-999.
- Hulmes 2002 Hulmes DJ. Building collagen molecules, fibrils, and suprafibrillar structures. *J Struct Biol* 2002;137:2-10.
- Jones 1999 Jones DK, Horsfield MA, Simmons A. Optimal strategies for measuring diffusion in anisotropic systems by magnetic resonance imaging. *J Magn Reson Imaging* 1999;42:515-525.
- Kärger 1988 Kärger J, Pfeifer H, Heink W. Principles and applications of self-diffusion measurements by nuclear magnetic resonance. *Advances in Magnetic Resonance* 1988;12:1-89.
- Keinan-Adamsky 2006 Keinan-Adamsky K, Shinar H, Navon G. Multinuclear NMR and MRI studies of the maturation of pig articular cartilage. *Magn Reson Med* 2006;55:532-40.
- Kellman 2005 Kellman P, McVeigh ER. Image reconstruction in SNR units: a general method for SNR measurements. *Magn Reson Med*. 2005;54:1439-1447. Erratum in: *Magn Reson Med*. 2007;58:211-212.
- Kiviranta 1984 Kiviranta I, Tammi M, Jurvelin J, Säämänen AM, Helminen HJ. Fixation, decalcification, and tissue processing effects on articular cartilage proteoglycans. *Histochemistry* 1984;80:569-573.
- Knauss 1999 Knauss R, Schiller J, Fleischer G, Kärger J, Arnold K. Self-diffusion of water in cartilage and cartilage components as studied

- 
- by pulsed field gradient NMR. *Magn Reson Med* 1999;41:285-292.
- Korhonen 2002 Korhonen RK, Laasanen MS, Töyräs J, Rieppo J, Hirvonen J, Helminen HJ, Jurvelin JS. Comparison of the equilibrium response of articular cartilage in unconfined compression, confined compression and indentation. *Journal of Biomechanics* 2002;35:903-909.
- Kummer 2005 Kummer B. *Biomechanik* pp 31-57. Köln, Germany, Deutscher Ärzte-Verlag, 2005
- Kurkijärvi 2004 Kurkijärvi JE, Nissi MJ, Kiviranta I, Jurvelin JS, Nieminen MT. Delayed gadolinium-enhanced MRI of cartilage (dGEMRIC) and T2 characteristics of human knee articular cartilage: topographical variation and relationships to mechanical properties. *Magn Reson Med* 2004;52:41-46.
- Lai 1991 Lai WM, Hou JS, Mow VC. A triphasic theory for the swelling and deformational behaviors of articular cartilage. *J Biomech Eng* 1991;113:245-258.
- Lammentausta 2006 Lammentausta E, Kiviranta P, Nissi MJ, Laasanen MS, Kiviranta I, Nieminen MT, Jurvelin JS. T2 relaxation time and delayed gadolinium-enhanced MRI of cartilage (dGEMRIC) of human patellar cartilage at 1.5 T and 9.4 T: Relationships with tissue mechanical properties. *J Orthop Res* 2006;24:366-74.
- Lauterbur 1973 Lauterbur PC. Image formation by induced local interactions: examples employing NMR. *Nature* 1973;242:190-191.

- 
- Le Bihan 1986      Le Bihan D, Breton E, Lallemand D, Grenier P, Cabanis EA, Laval-Jeantet M. MR imaging of intravoxel incoherent motions : application to diffusion and perfusion in neurologic disorders. *Radiology* 1986;161:401-407.
- Le Bihan 1995      Le Bihan D. *Magnetic Resonance Imaging of Diffusion and Perfusion: Applications to Functional Imaging*. New York, USA, Lippincott-Raven Press, 1995.
- Le Bihan 2001      Le Bihan D, Mangin JF, Poupon C, Clark CA, Pappata S, Molko N, Chabriat H. Diffusion tensor imaging: concepts and applications. *J Magn Reson Imaging* 2001;13:534-546.
- MacLean 1998      MacLean CH, Knight K, Paulus H, Brook RH, Shekelle PG. Costs attributable to osteoarthritis. *J Rheumatol* 1998;25:2213-2218.
- Mankin 1974      Mankin HJ. The reaction of articular cartilage to injury and osteoarthritis. *New England Journal Medicine* 1974;291:1285-1292 and 1335-1340.
- Mansfield 1973      Mansfield P, Grannell PK. NMR 'diffraction' in solids? *J Phys C: Solid State Phys* 1973;6:L422-426.
- Maroudas 1968      Maroudas A. Physicochemical properties of cartilage in the light of ion exchange theory. *Biophys J* 1968;8:575-595.

- 
- Maroudas 1976 Maroudas A. Balance between swelling pressure and collagen tension in normal and degenerate cartilage. *Nature* 1976;260:808-809.
- Maroudas 1977 Maroudas A, Venn M. Chemical composition and swelling of normal and osteoarthrotic femoral head cartilage. II. Swelling. *Ann Rheum Dis* 1977;36:399-406.
- Maroudas 1979 Maroudas A. Physicochemical properties of articular cartilage. *Adult Articular Cartilage*, M.A.R. Freeman ed., Pitman Medical Publishing, Kent, England, pp.215-290.
- Maroudas 1980 Maroudas A, Bayliss MT, Venn MF. Further studies on the composition of human femoral head cartilage. *Ann Rheum Dis* 1980;39:514-523.
- Maroudas 1991 Maroudas A, Wachtel E, Grushko G, Katz EP, Weinberg P. The effect of osmotic and mechanical pressures on water partitioning in articular cartilage. *Biochem Biophys Acta* 1991;1073:285-294.
- Meder 2006 Meder R, de Visser SK, Bowden JC, Bostrom T, Pope JM. Diffusion tensor imaging of articular cartilage as a measure of tissue microstructure. *Osteoarthritis Cartilage*. 2006;14:875-81.
- Melhem 2002 Melhem ER, Mori S, Mukundan G, Kraut MA, Pomper MG, van Zijl PCM. Diffusion tensor MR imaging of the brain and white matter tractography. *Am J Roentgenol* 2002;178:3-16.

- 
- Mlynarik 1999 Mlynarik V, Trattnig S, Huber M, Zernbasch A, Imhof H. The role of relaxation times in monitoring proteoglycan depletion in articular cartilage. *J Magn Reson Imaging* 1999;10:497-502.
- Mlynarik 2003 Mlynarik V, Sulzbacher I, Bittsanky M, Fuiko R, Trattnig S. Investigation of apparent diffusion constant as an indicator of early degenerative disease in articular cartilage. *J Magn Reson Imaging* 2003;17:440-444.
- Moseley 1990 Moseley ME, Cohen Y, Kucharczyk J, Mintorovitch J, Asgari HS, Wendland MF, Tsuruda J, Norman D. Diffusion-weighted MR imaging of anisotropic water diffusion in cat central nervous system. *Radiology* 1990;176:439-445.
- Moseley 1991 Moseley ME, Kucharczyk J, Asgari HS, Norman D. Anisotropy in diffusion-weighted MRI. *Magn Reson Med* 1991;19:321-326.
- Mosher 2000 Mosher TJ, Dardzinski BJ, Smith MB. Human articular cartilage: influence of aging and early symptomatic degeneration on the spatial variation of T2-preliminary findings at 3T. *Radiology* 2000;214:259-266.
- Mow 1997 Mow VC, Hayes WC. *Basic Orthopaedic Biomechanics*. Philadelphia, USA, Lippincott-Raven, 1997.
- Muir 1970 Muir H, Bullough P, Maroudas A. The distribution of collagen in human articular cartilage with some of its physiological implications. *J Bone Joint Surg Br* 1970;52:554-563.

- 
- Neeman 1991      Neeman M, Freyer JP, Sillerud LO. A simple method for obtaining cross-term-free images for diffusion anisotropy studies in NMR microimaging. *Magn Reson Med*. 1991;21:138–143.
- Nieminen 2001      Nieminen MT, Rieppo J, Töyräs J, Hakumaki JM, Silvennoinen J, Hyttinen MM, Helminen HJ, Jurvelin JS. T<sub>2</sub> relaxation reveals spatial collagen architecture in articular cartilage: a comparative quantitative MRI and polarized light microscopic study. *Magn Reson Med* 2001;46:487-493.
- Niethard 2005      Niethard FU, Pfeil J. *Orthopädie*. Stuttgart, Germany, Thieme, 2005
- Nissi 2003      Nissi MJ, Rieppo J, Töyräs J, Laasanen HJ, Jurvelin JS, Nieminen MT. T<sub>2</sub> relaxation reveals differences in spatial collagen network anisotropy in human, bovine and porcine articular cartilage. *Proceedings 11<sup>th</sup> Scientific Meeting ISMRM, Toronto, Canada*. 11:54, 2003.
- Nissi 2007      Nissi MJ, Rieppo J, Töyräs J, Laasanen MS, Kiviranta I, Nieminen MT, Jurvelin JS. Estimation of mechanical properties of articular cartilage with MRI - dGEMRIC, T<sub>2</sub> and T<sub>1</sub> imaging in different species with variable stages of maturation. *Osteoarthritis Cartilage*. 2007;15:1141-1148.
- O'Connor JJ 1993      O'Connor JJ, Johnston I. *Mechanics of Osteoarthritis of the knee*. 14<sup>th</sup> Congress on Biomechanics. *Book of Abstract* 1993: 968-969.
- O'Connor P 1988      O'Connor P, Orford CR, Gardner DL. Differential response to compressive loads of zones of canine hyaline articular cartilage:

- 
- micromechanical, light and electron microscopic studies. *Ann Rheum Dis* 1988;47:414-420.
- Pierpaoli 1996 Pierpaoli C, Jezzard P, Basser PJ, Barnett A, Di Chiro G. Diffusion tensor MR imaging of the human brain. *Radiology* 1996;201:637-648.
- Pierpaoli and Basser 1996 Pierpaoli C and Basser JP. Toward a quantitative assessment of diffusion anisotropy. *Magn Reson Med* 1996;36:893-906.
- Pauwels 1960 Pauwels F. A new theory on the influence of mechanical stimuli on the differentiation of connective tissue. *Z Anat Entwickl Gesch* 1960;121:478-515.
- Pullig 2001 Pullig O, Pfander D, Swoboda B. Molecular principles of induction and progression of arthrosis. *Orthopäde* 2001;30:825-833.
- Purcell 1946 Purcell EM, Torrey HC, Pound RV. Resonance absorption by nuclear magnetic moments in a solid. *Phys Rev* 1946;69:37.
- Putz 2003 Putz R, Fischer H. Altersunterschiede der Anordnung der kollagenen Fasern im Gelenkknorpel. *Osteologie Aktuell* 1993;VII:42-44.
- Rabi 1938 Rabi II, Zacharias JR, Millman S, Kusch P. A new method of measuring nuclear magnetic moments. *Phys Rev* 1938;53:318.
- Raya 2008 Raya JG, Melkus G, Dietrich O, Filidoro L, Weber D, Reiser MF, Jakob PM, Glaser C. Multiparametric characterization of healthy

- 
- and diseased cartilage at 17.6 T: Early results. Proceedings 16<sup>th</sup> Scientific Meeting ISMRM, Toronto, Canada, 16:330, 2008.
- Raya 2008b      Raya JG, Dietrich O, Birkenmaier C, Sommer J, Reiser MF, Baur-Melnyk A. Feasibility of a RARE-based sequence for quantitative diffusion-weighted MRI of the spine. *Eur Radiol*. 2007;17:2872-2879.
- Raya 2009      Raya JG, Melkus G, Dietrich O, Adam-Neumair S, Muetzel E, Reiser MF, Jakob PM, Glaser C. Multiparametric analysis of healthy and diseased articular cartilage at 17.6T and correlation with histology. Proceedings 17<sup>th</sup> Scientific Meeting ISMRM, Honolulu, Hawaii, USA, 17:4001, 2009.
- Raya 2011      Raya JG, Arnoldi AP, Weber DL, Filidoro L, Dietrich O, Adam-Neumayer S, Mützel E, Melkus G, Putz R, Reiser MF, Jakob PM, Glaser C. Ultra-high field diffusion tensor imaging of articular cartilage correlated with histology and scanning electron microscopy. Accepted by *MAGMA* May 2011.
- Reif 1987      Reif F. *Statistische Physik und Theorie der Wärme*. 3. Auflage. Berlin, Germany, Walter de Gruyter, 1987.
- Tunner 1975      Tanner JE. Transient diffusion in system partitioned by permeable barriers. Application to NMR measurements with a pulsed field gradient. *J Chem Phys* 1975;69:1748-1754.
- Shinar 2006      Shinar H, Navon G. Multinuclear NMR and microscopic MRI studies of the articular cartilage nanostructure. *NMR Biomed* 2006;19:877-893.

- 
- Stejskal and Tanner 1965 Stejskal OE, Tanner JE. Spin diffusion measurements: spin echoes in the presence of a time-dependent field gradient. *J Chem Phys* 1965;42:288-292.
- Tanner 1978 Tanner JE. Transient diffusion in a system partitioned by permeable barriers. Applications to NMR measurements with a pulsed field gradient. *J Chem Phys* 1978;69:1748-1754.
- Tanner 1979 Tanner JE. Self diffusion of water in frog muscle. *Biophys J* 1979;28:107-116.
- Ulug and van Zijl 1999 Ulug AM and van Zijl PC. Orientation-independent diffusion imaging without tensor diagonalization: Anisotropy definitions based on physical attributes of the diffusion ellipsoid. *J Magn Reson Imaging* 1999;9:804-813.
- Valdes 2008 Valdes AM, Spector TD. The contribution of genes to osteoarthritis. *Rheum Dis Clin North Am* 2008;34:581-603.
- Venn 1977 Venn M, Maroudas A. Chemical composition and swelling of normal and osteoarthrotic femoral head cartilage. I *Chemical Ann Rheum Dis* 1977;36:121-129.
- Wayne 2003 Wayne JS, Kraft KA, Shields KJ, Yin C, Owen JR, Disler DG. MR imaging of normal and matrix-depleted cartilage: correlation with biomechanical function and biochemical composition. *Radiology* 2003;228:493-499.

- 
- Weber DL 2007 Weber DL, Filidoro L, Dietrich O, Weber J, Reiser M, Jakob PM, Glaser C. Investigation of SNR for DTI with human articular cartilage at 17.6 Tesla. Proceedings Scientific Meeting ISMRM-ESMRMB, Berlin, Germany, 15: 2655, 2007.
- Wentorf 2003 Wentorf F, Chen W, Zhang X, Initial findings of diffusion anisotropy in articular cartilage. Proceedings 11<sup>th</sup> Scientific Meeting ISMRM, Toronto, Canada, 11:57, 2003.
- Witte 2009 Witte F. Schmerzende Gelenke. Süddeutsche Zeitung 28.10.2009;23.
- Xia 1995 Xia Y, Farquhar T, Burton-Wurster N, Vernier-Singer M, Lust G, Jelinski LW. Self-diffusion monitors degraded cartilage. Arch Biochem Biophys 1995;323-328.
- Yelin 1995 Yelin E, Callaghan LF. The economic cost and social and psychological impact of musculoskeletal conditions. Arthritis Rheum 1995;38:1351-1362.
- Zhou 2002 Zhou XJ, Leeds NE, McKinnon GC, Kumar AJ. Characterization of benign and metastatic vertebral compression fractures with quantitative diffusion MR imaging. Am J Neuroradiol 2002;23:165-170.



---

# Danksagung

Herrn Prof. Dr. Dr. h.c. Maximilian Reiser danke ich dafür, dass er mir die Gelegenheit gegeben hat, an der Forschungsarbeit in seinem Institut teilnehmen zu können, insbesondere weil er mir immer entgegengekommen ist, Familie und Beruf zu vereinbaren.

Herrn Prof. Dr. Peter Jakob der Universität Würzburg danke ich für die gute Kooperationsarbeit mit unserer Forschungsgruppe und dafür, dass er uns die Ausrüstung und Instrumente seiner Abteilung zur Verfügung gestellt hat.

Mein besonderer Danke gilt Herrn PD Dr. Christian Glaser, der die Forschungsgruppe Muskuloskelettale Bildgebung ins Leben gerufen und deren Fortkommen mit seinen bereichernden Ideen und Beiträgen begleitet hat. Ich bedanke mich für das interessante Forschungsthema und neben den zahlreichen anregenden Diskussionen bei den medizinischen Aspekten insbesondere für seine freundliche Unterstützung in allen Phasen dieser Arbeit.

Herrn PD Dr. Olaf Dietrich und Herrn Dr. José Raya danke ich für die Unterstützung bei physikalischen Fragestellungen und ihre Verbesserungsvorschläge.

Herrn Jürgen Weber danke ich für die Unterstützung bei der Programmierung der Auswerteroutine.

Herrn Wammetsberger danke ich für die technische Hilfe bei der Probenhalterungsarchitektur.

---

Auch will ich mich bei allen Kollegen bedanken, die ich in diesen Jahren kennengelernt habe, für ihre Hilfsbereitschaft und das freundschaftliche Klima in der Arbeitsgruppe: Andreas, Christoph, Daniel aus Würzburg, Herbert, Michael I., Michael P., Manuela, Steven, Sylvia, Thomas, Ulrike.

Ein ganz besonders herzliches Dankeschön gilt meinen Eltern, die mir mein Studium ermöglicht und mich immer unterstützt haben, sowie meinem Ehemann für die unendliche Geduld und meinen Kindern für die verbreitete gute Laune.